Coupling protonation states of acid-sensing ion channels to dynamics and function

Megan Miaro

A thesis submitted to the University of Ottawa in partial fulfillment of the requirements for the Master of Science degree in Chemistry

Department of Chemistry and Biomolecular Sciences

Faculty of Science

University of Ottawa

Abstract

Acid-sensing ion channels (ASICs) are trimeric, sodium-selective proton-gated ion channels. Having ligands as small as protons presents a challenge when studying the structure-function relationships of pH-dependent gating. Knowing where protons must bind to evoke a pH-dependent conformational change related to gating would provide one with insights into the molecular mechanisms underlying pH-dependent function in ASICs. We use molecular dynamics (MD) simulations that allow us to model explicit protons and directly examine the effects of changing protonation states on ASIC1 dynamics. We first combine the use of unbiased MD simulations with pK_a prediction on the three functional states of cASIC1 to identify the effects of protonation state changes on interactions between ionizable residues in the acidic pocket (ACP), a region rich in acidic residues in the protein that plays a role in pH-sensing. We interpret the importance of E98, a buried residue in the ACP with a highly shifted pK_a value, as well as the positively charged R191, also in the ACP, which has a flexible side chain and can interact with multiple negatively charged side chains, and the role of these residues in the pH-dependent collapse of the ACP. Additionally, we identify a hydrogen-bond network in the palm domain that consists of the Q277 side chain that interacts with the E80 side chain and L414 backbone carbonyl. This network contributes to a stable desensitized state and is stabilized by an E80-/E412H/E417H protonation configuration. Next, targeted MD was combined with pK_a prediction to simulate the full transition pathways and to link protonation states with the molecular mechanisms involved in conformational changes. Our results suggest four residues, E98, E314, H328, and E374, that may be important in pH-sensing and gating, and that require further functional investigation in the context of activation and desensitization. This research exemplifies how MD is a useful tool in studying how protonation directly affects the structural

dynamics of a protein and how it can complement existing functional studies and be used to suggest future experimental investigations.

Acknowledgements

I want to express my gratitude to the following:
First my supervisor, Dr. Maria Musgaard, her expertise, and guidance were invaluable throughout this research and in writing this thesis. I have benefited greatly from her mentorship, enthusiasm, and encouragement. I am grateful to have worked with her over the past three years.

My co-supervisor Dr. Natalie Goto, for providing guidance, and input in the writing of my thesis.

The members of my thesis advisory committee, Drs Corrie DaCosta and Jyh-Yeuan (Eric) Lee for providing guidance and thoughtful feedback, especially in encouraging me to see the big picture in my work.

My colleagues, Anna Ananchenko, Mariam Taktek and Rebecca Dean, for their insights and fruitful discussions at group meetings from which I have learned much.

Lastly, I want to express my deepest gratitude to my family for their unconditional support and encouragement throughout my studies.

Table of Contents

List of Abbreviations

ASIC	Acid-sensing Ion Channel
ACP	Acidic Pocket
CNS	Central Nervous System
CpHMD	Constant pH Molecular Dynamics
CV	Collective Variable
DEG	Degenerin
DpHMD	Discrete pH Molecular Dynamics
ECD	Extracellular Domain
ENaC	Epithelial Sodium Channel
GB	Generalized Born
ICD	Intracellular Domain
LGIC	Ligand-gated Ion Channel
MD	Molecular Dynamics
PAC	Proton-activated chloride channel
PB	Poisson-Boltzmann
PNS	Peripheral Nervous System
RMSD	Root Mean Square Deviation
SASA	Solvent Accessible Surface Area
SSD	Steady-State Desensitization
TMD	Transmembrane Domain
VCF	Voltage Clamp Fluorometry
WT	Wild Type

List of Figures

Chapter 1

Chapter 2

Chapter 3

Chapter 4

Appendix A

Appendix B

List of Tables

Appendices

Chapter 1 : Introduction

Ion channels are transmembrane proteins ubiquitously expressed in all cell types and have the function of generating electrical signals important in intercellular signalling. Acid-sensing ion channels (ASICs) formulate a subfamily of ion channels that are primarily expressed in the central and peripheral nervous systems. We strive to understand how the ASIC protein structure relates to its function. The research presented in this thesis aims to characterize the ligand-binding sites of ASICs and link these to protein dynamics to better understand the gating mechanisms of ASICs. In this introductory chapter, the background and context will first be discussed, followed by the research question, objectives, significance, and the limitations of the study.

1.1. Ligand-gated ion channels

Ion channels, a class of membrane-spanning proteins, have evolved to mediate the transport of specific ions across a cellular membrane bilayer. Ion channels play an important role in signal transduction across biological membranes. They are ubiquitously expressed in prokaryotic and eukaryotic cells and this class of proteins can be traced to before the development of multicellular organisms (Burkhardt et al., 2011, Liebeskindet 2011). Their function involves the conductance of specific ions across a membrane bilayer, usually in response to external stimuli. Typically, without a stimulus, ion channels exist in the resting state, a non-conducting functional state with a closed gate. Known stimuli include mechanical force, changes in membrane

potential, and ligand-binding (Barker et al., 2017). The channels responding to the latter are named ligand-gated ion channels (LGICs). Although not solely expressed in the nervous system, LGICs mediate fast synaptic transmission on the millisecond time scale. Ligand-binding induces conformational changes in the protein, driving it between the conducting, open state, or non-conducting states, the resting and desensitized states. LGICs represent a diverse group of proteins with their function evolved to be specific to certain ions and ligands. As such, these proteins have different properties and expression levels in different cell types and make for potential drug targets (Alexander et al., 2017).

1.2. Acid-sensing ion channels

Acid-sensing ion channels (ASICs) are trimeric, proton-gated ion channels expressed in the central and peripheral nervous systems (CNS and PNS, respectively). They are members of the family of degenerin/epithelial (DEG/ENaC) superfamily of Na^+ channels, a group of ion channels that typically feature two transmembrane helices (TMD) and a large extracellular domain (ECD) (Waldmann et al., 1997). These sodium-selective ion channels are involved in physiological processes such as nociception (Rang et al., 1991), synaptic plasticity, learning, memory in the brain, and the sensation of fear (Coryell et al., 2007; Wemmie et al., 2002). In addition, they are implicated in several pathophysiologies, namely, pain-associated tissue acidosis from injury, inflammation, and ischemia (Issberner et al., 1996; Pan et al., 1999). Six subtypes are known to exist in mammals, these include ASIC1a, ASIC1b, ASIC2a, ASIC2b, ASIC3, and ASIC4. Of these subtypes, ASIC1a, ASIC1b, ASIC2a and ASIC3 subtypes are

responsive to extracellular acidification. The channels can function as homotrimers or as heterotrimers with a combination of the existing subtypes (Wemmie et al., 2013). ASIC1a is the main pH-sensor of the brain and is implicated in the detection of tissue ischemia, neural inflammation, synaptic cleft acidification, and metabolic stress (Du et al., 2014; Wemmie et al., 2013), making these channels potential drug targets.

Understanding the structure-function relationship of ASICs is important for the development of targeted therapeutics. Extensive functional studies have been performed on ASICs to better describe their function. ASIC1 was the first ASIC clone to be described as proton-sensitive (Waldmann et al., 1997), and ASIC1a is the most extensively studied ASIC subtype. Upon extracellular acidification, protons bind to regions in the ECD of the ion channel, promoting activation that is characterized by transient currents. The specific, proton-binding residues are, however, still unknown. ASIC1a activation is rapid with a time constant of ~ 6 to 13 milliseconds (ms) at pH 6.5 (Babini et al., 2002; X. Chen et al., 2005; Sherwood et al., 2011; Sutherland et al., 2001). Following activation, the ion channels rapidly undergo desensitization, with a time constant of ~1.2 to 3.5 s (Bässler et al., 2001; Hesselager et al., 2004; Sherwood et al., 2011; Sutherland et al., 2001), while under stimulating conditions. The desensitized state is an activated, non-conducting state. After the removal of the stimulus, the channels can return to the resting state (Figure 1.1). This transition is named recovery and has a time constant of ~5 to 13 s at pH 7.4 (Babini et al., 2002; Benson et al., 2002; Sutherland et al., 2001).

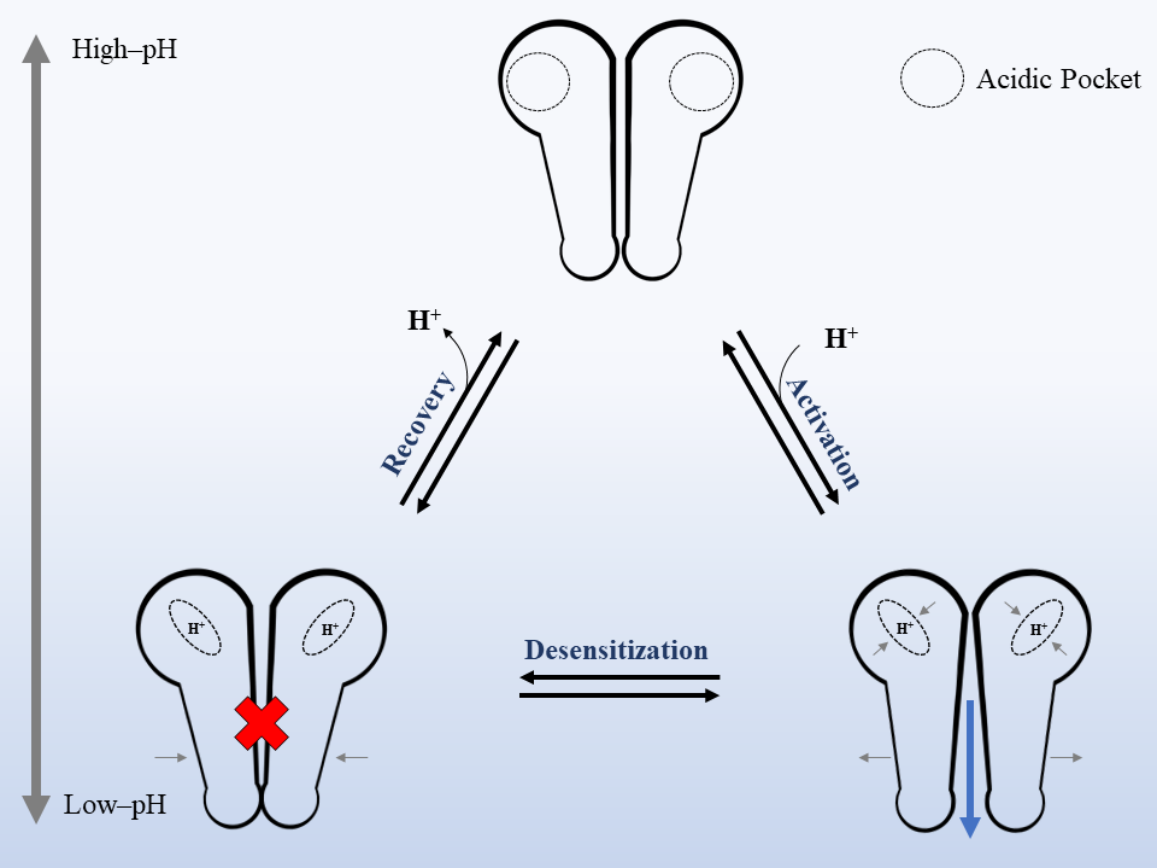

Figure 1.1 The gating cycle of ASIC1.
The high pH resting state has a closed gate, an expanded acidic pocket and central vestibule. During extracellular acidification, protons bind to regions in the extracellular domain. The open state has a collapsed acidic pocket, central vestibule, and an open gate. Desensitization leads to a ligand-bound state with a closed gate. The desensitized extracellular domain architecture is highly similar to the open state with further collapse of the central vestibule. With extracellular alkalinization, the protons unbind, and the acidic pocket and central vestibule expand once again. This process is termed recovery.

1.3. ASIC1 Architecture

X-ray crystal structures for all three major functional states, the open, desensitized, and resting states, exist only for the chicken (*Gallus gallus*) ASIC1 (cASIC1) clone. Descriptions of other cASIC1 and hASIC1a structures follow later in this section. Overall, ASICs consist of a large ECD (residues 72 to 425, cASIC1 numbering) that house the putative proton-sensors, with two transmembrane helices (residues 42 to 71 and 426 to 455), similar to the global architecture of P2X receptors (Baconguis et al., 2013). P2X receptors are also trimeric, cation-selective LGICs (Khakh & North, 2012). However, ASICs have a domain swap in the second transmembrane helix (TM2), contributed by a conserved glycine-alanine-serine (GAS) belt that forms a constriction in the pore (Baconguis et al., 2014). The domain swap was not observed in the first cASIC1 crystal structure elucidated in 2007 (Jasti et al., 2007) (Figure 1.2A, Figure 1.3A). The architecture of the ECD can be further divided into subdomains that are likened to the parts of a hand. The palm domain consists of seven β-strands, above it is the knuckle domain composed of two helical segments. The β-ball domain is made of five short β-strands at the core of the ECD. The thumb consists of two long helices and non-structured segments and the finger domain is formed by short helical segments and unstructured elements. The β-ball, thumb and finger domains form the ACP, a region that houses an abundance of acidic residues (Figure 1.2C). The palm domains of each subunit form a cavity internal to the protein referred to as the central vestibule. This vestibule also houses four acidic residues, E80, E374, E412, and E417 (Figure 1.2D).

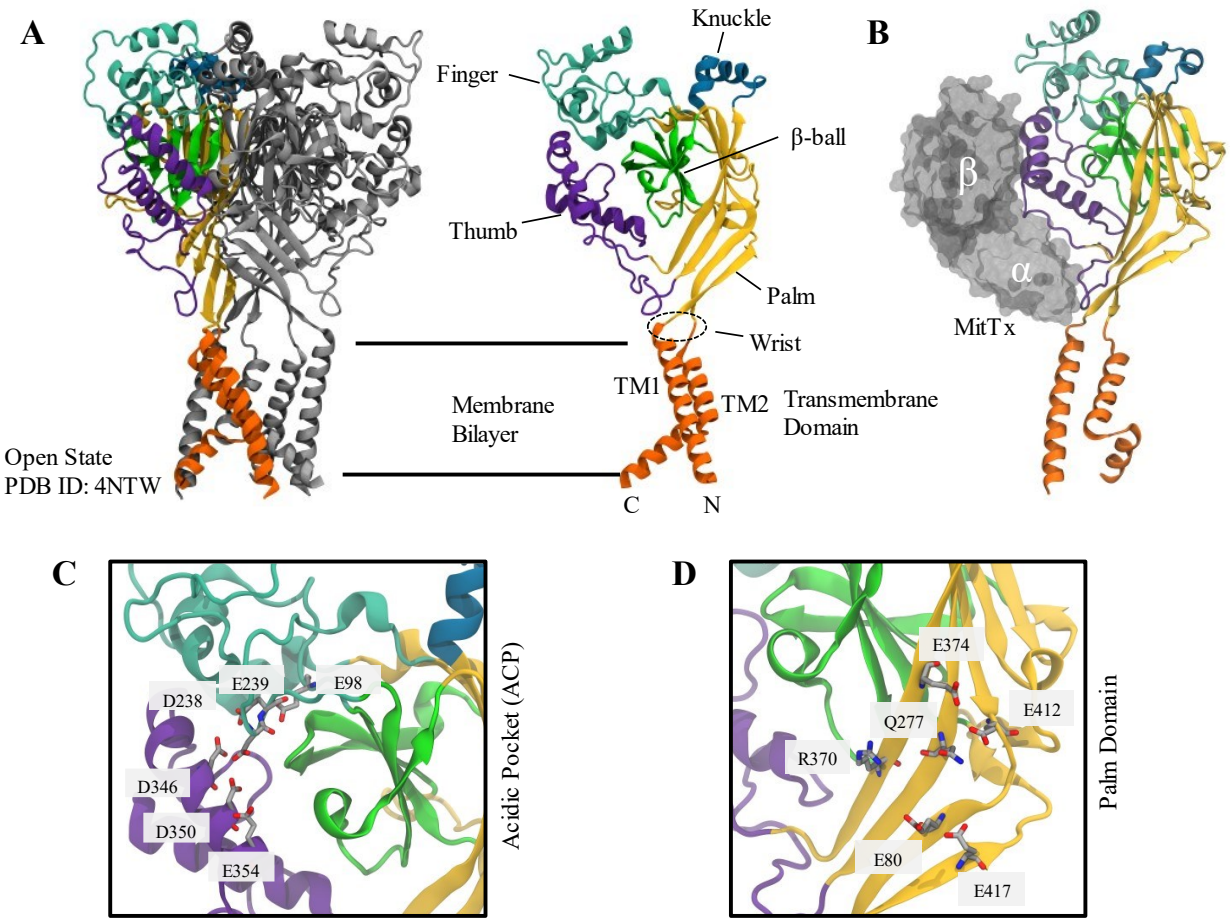

Figure 1.2 ASIC1 architecture.
A) A trimer of the open state (PDB: 4NTW) (Baconguis et al., 2014) with a single subunit coloured and a subunit annotated by subdomain. N and C represent the N- and C- termini. TM1 and TM2 are transmembrane helix 1 and transmembrane helix 2, respectively. B) A single subunit of the open state with the MitTx toxin heterodimer bound to the thumb domain. C) A close-up of the acidic pocket and D) the palm domain with charged residues shown.

The desensitized state structure was resolved at 3 Å, pH 6.5 using X-ray crystallography (PDB: 4NYK). The construct used to determine this crystal structure was called ASIC1mfc, which consisted of all amino acid residues up to 466, ending after the TM2 helix. Residues 46 to 451 were resolved in the crystal structure and it features a closed gate, contributed by D433 and G436 from the TM2 helix (Figure 1.3B), (Gonzales et al., 2009).

The physiologically relevant open state structure (PDB: 4NTW) was elucidated in complex with the Texas Coral Snake toxin (MitTx) at pH 5.5 (Baconguis et al., 2014). MitTx is a heterodimer composed of two non-covalently linked α and β subunits. The toxin was found to activate ASIC1 and maintain it in an open conformation (Figure 1.2A, B), independent of pH, at nanomolar concentrations (Bohlen et al., 2011). The cASIC1 Δ13 construct was used, where the first 13 residues on the N-terminus and the last 63 residues from the C-terminus, were removed to improve structure resolution (Baconguis & Gouaux, 2012). The construct was crystallized in the presence of Na^+ and had a resolution of 2.1 Å. The structures exhibit 3-fold symmetry. The toxin makes contacts with the ECD, specifically at the wrist, knuckle and thumb domains (Baconguis et al., 2014).

The cASIC1 resting state structure (PDB: 5WKU) was resolved at pH 8.0 in the presence of Ca^{2+} at a resolution of 2.95 Å. A pH-dependent Δ25 construct including residues 25 to 463 was used for crystallization. The resting state adopts an expanded ACP and a closed gate (Yoder et al., 2018), similar to the pore architecture of the gate in the desensitized state (Baconguis et al., 2014). This indicates a conserved conformation of the gate between the non-conducting functional states that may be independent of pH (Yoder et al., 2018) (Figure 1.3C). The three structures described are used in this work.

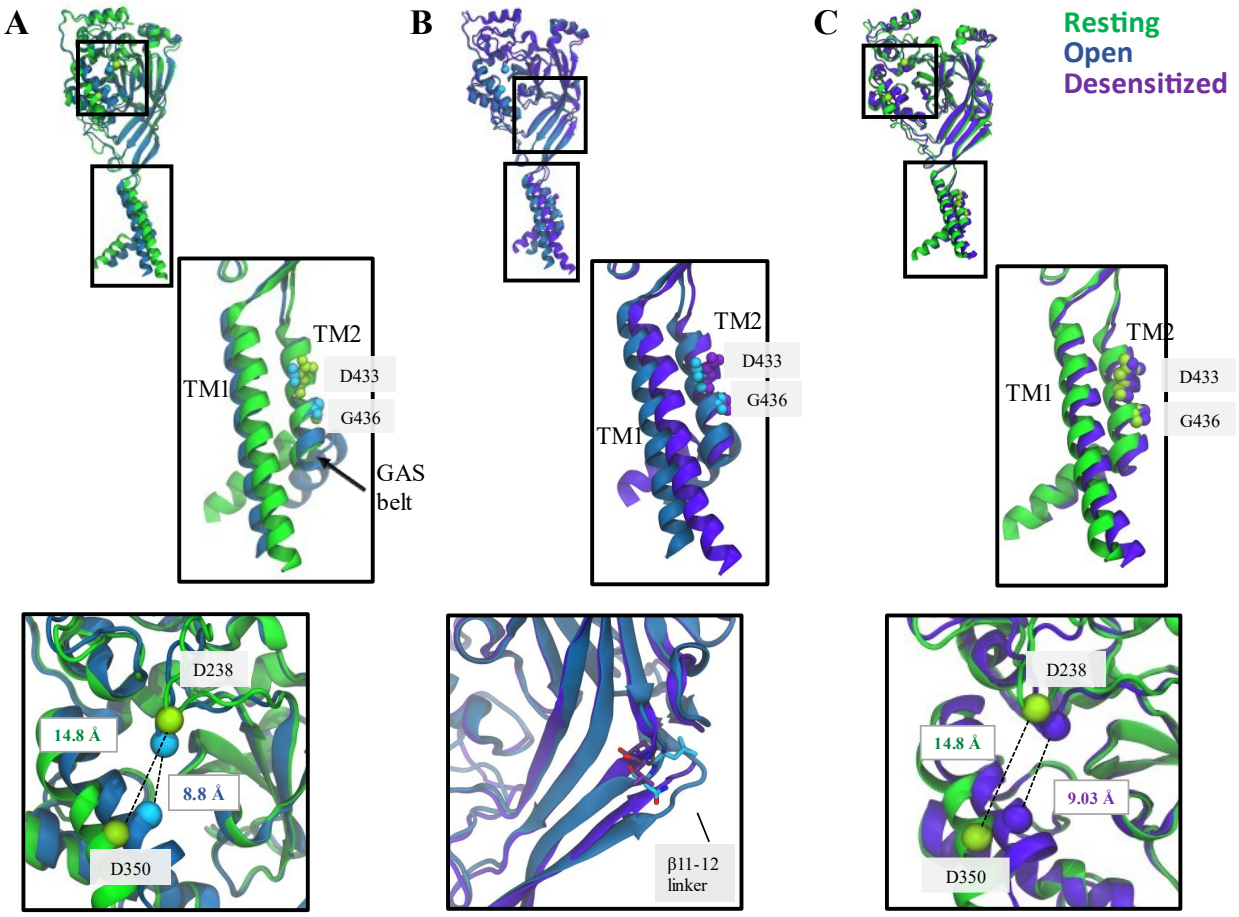

Figure 1.3 Superimposition of the ASIC1 functional states.
A) Superimposition of a resting state (green; PDB ID 5WKU) and open state (blue; PDB ID 4NTW) subunit. The transmembrane helices and acidic pocket are blown up below, top and bottom, respectively. Top: the TM1 and TM2 helices are shown with the pore-lining residues D433 and G436 in Van der Waals (VDW) representation. The GAS belt breaking TM2 into two helical segments is indicated. Bottom: Average D238-D350 Cα distances of the crystal structures are drawn as representative distances between the thumb and finger domains for the resting (14.8 Å) and open (8.8 Å) states. B) Superimposition of an open (blue) and desensitized (purple) state subunit. Close-ups of the palm domain and the transmembrane helices are shown on the below, top and bottom, respectively. Top: Superimposition of the TM helices with D433 and G436 shown in VDW representation. Bottom: the β11-12 linker (L414 and N415) takes on a different conformation between the open and desensitized states. C) Superimposition of a desensitized state and resting state subunit. The transmembrane helices and ACP are blown up below, top and bottom, respectively, as in panel A. Average D238-D350 Cα distances of the crystal structures are drawn for the desensitized (9.03 Å) and resting (14.8 Å) states. Superimposition was performed by aligning the Cα atoms of residues 72 to 425 for the ECD (ACP and palm domain panels), and residues 45 to 455 for the full subunits and TMD panels.

The cASIC1 constructs used for each structure differs in sequence coverage, and they all lack an intracellular domain (ICD) at the C-terminus, which was truncated to resolve these structures at higher resolutions (Figure 1.4). A gating cycle using these three structures is shown in Figure 1.5. In previous research, the pore domain and TM helices are generally stable in our simulations that lack the ICD. It is possible that the ICD may play a role in ASIC1 dynamics during pH-sensing although its role is not well known. We assume that the lack of the ICD will not greatly affect our interpretations.

Other existing structures include cASIC1 in an inactive state at a resolution of 1.9 Å (Jasti et al., 2007), a psalmotoxin-bound cASIC1 displaying ion-selective and non-selective functions (Baconguis & Gouaux, 2012), and in inactive states (Dawson et al., 2012). More recently, structures of the desensitized and resting states were elucidated with regions of the intracellular domain resolved, using cryo-electron microscopy (Yoder & Gouaux, 2020).

The first human acid-sensing ion channel 1a (hASIC1a) structure, inhibited by snake toxin mambalgin1, was resolved at pH 8.0 with cryo-electron microscopy. The structure is presumably trapped in a closed state. The structural similarity with the cASIC1 resting state is high with an overall Cα RMSD of 0.88 Å (Sun et al., 2020).

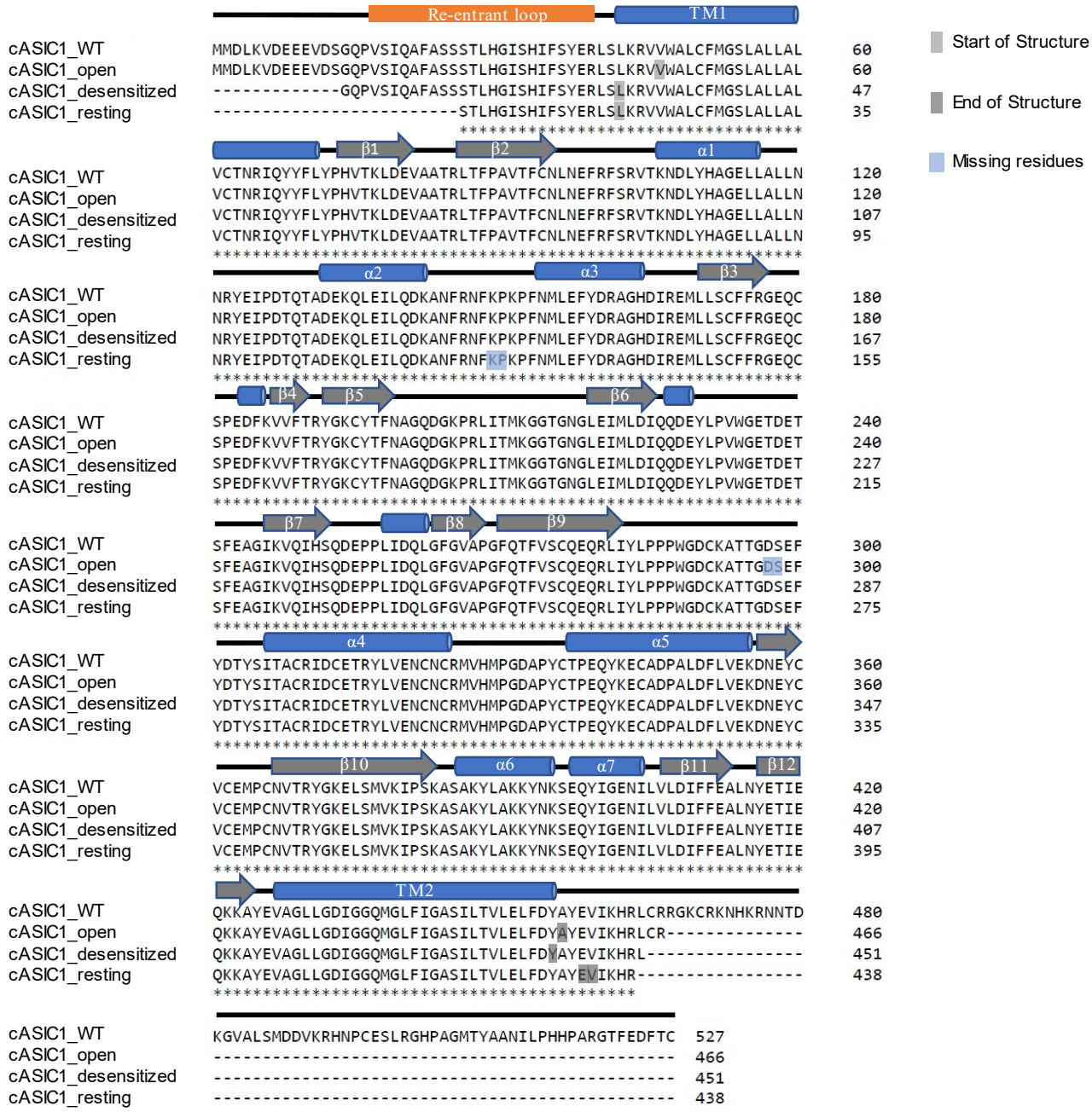

Figure 1.4 Multiple sequence alignment of the cASIC1 crystal structure constructs. Sequences of the constructs used are compared to the wild-type cASIC1 (*gallus gallus)* sequence. cASIC1_WT; wild-type sequence (FASTA Accession code: Q1XA76), cASIC1_open; open state (PDB: 4NTW), cASIC1_desensitized (PDB: 4NYK) and cASIC1_resting (PDB: 5WKU). The first and last residues of each structure, as well as any missing residues is highlighted as indicated above.

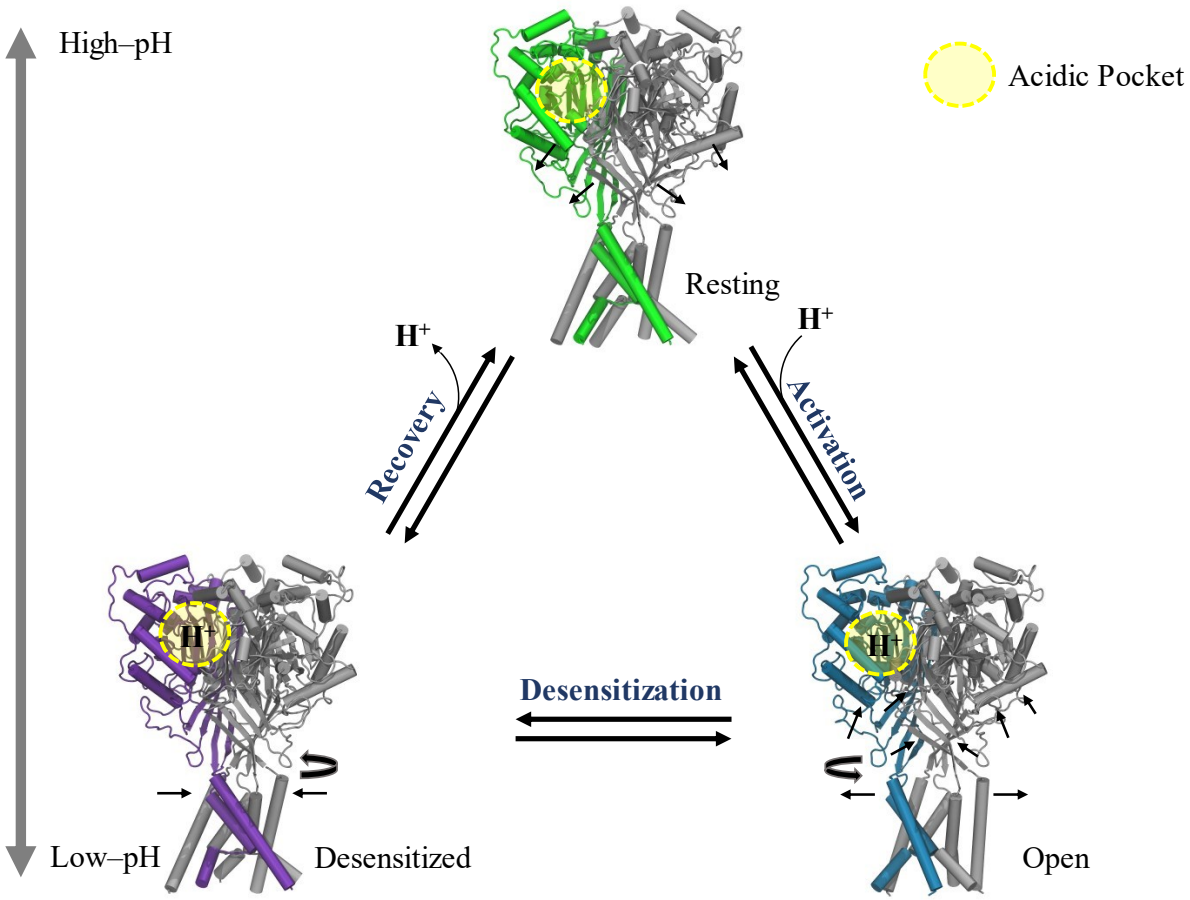

Figure 1.5 The functional cycle of cASIC1. The three crystal structures described in section 1.3 are shown in the functional cycle of ASICs. Arrows indicate general motions involved in the conformational changes between structures. H^+ represents protons.

1.4. Ligand-binding sites

It was hypothesized that the ligand-binding (proton-binding) site is in the acidic pocket (ACP). Again, the ACP is a cavity in the ECD formed by the thumb, finger and β-ball domains (Figure 1.2C). This pocket is abundant in polar and charged residues. It was thought that proton-binding to the ACP would lead to the formation of carboxyl-carboxylate interactions between interfacing acidic residues (D238-D350, E239-D346 and E220-D408) that results in ACP collapse. This conformational change would transduce to the TMD and promote the opening of the gate (Jasti et al., 2007). Other low pH structures also have a collapsed ACP (Baconguis et al., 2014; Baconguis & Gouaux, 2012; Dawson et al., 2012; Gonzales et al., 2009; Yoder et al., 2018; Yoder & Gouaux, 2020). Additionally, voltage clamp fluorometry (VCF) and luminescence resonance energy transfer have captured the motions of collapse between the thumb and finger domains in response to extracellular acidification (Ramaswamy et al., 2013; Vullo et al., 2017). Mutations of the residues hypothesized to form carboxyl-carboxylate interactions, specifically D346N and D350N, exhibited a decrease in proton sensitivity (Jasti et al., 2007), underlining their importance in proton-sensing. D238N also displayed a decrease in proton-sensitivity (Paukert et al., 2008). Many mutagenesis studies have targeted acidic residues in the ACP, yet even with extensively mutated constructs of six residues (E219Q/D237N/E238Q/D345N/D407N in mouse ASIC1a (mASIC1a) numbering) (Krauson et al., 2013) and even up to 16 acidic residues (E79Q/E177Q/D183N/D237N/E238Q/D303N/E315Q/E321Q/E344Q/D347N/D351N/E355Q in human ASIC1a (hASIC1a) numbering), ASIC1 still retained pH-dependent function (Vullo et al., 2017) providing evidence that the ACP is not the only proton-binding site crucial to pH-dependent activation.

ASIC1a function can also be modulated by amiloride (Alvarez de la Rosa et al., 2000; Kellenberger & Schild, 2002), extracellular Ca^{2+} (Babini et al., 2002), and toxins (Bohlen et al., 2011; X. Chen et al., 2005; Diochot et al., 2012; Escoubas et al., 2000). Structural studies have shown that these modulators tend to commonly bind to the thumb, finger, and wrist domains (Dawson et al., 2012; Sun et al., 2020). For example, MitTx1 is a selective agonist of hASIC1a (Bohlen et al., 2011) that binds to the thumb domain of ASICs. A nanobody (Nb.C1) has been shown to bind to the same site as the toxin in hASIC1a and as a result, it reduced channel activation by MitTx1 (Wu et al., 2021). A recent study using voltage-clamp fluorometry (VCF) also points to these three sites (finger, thumb and wrist) as the likely proton-sensing domains of ASIC1 (Vullo et al., 2021). Mutations to the thumb, wrist, and palm subdomains display less pH-sensitive phenotypes in activation and in desensitization (Krauson et al., 2013; Liechti et al., 2010; Lynagh et al., 2018; Paukert et al., 2008; Tianbo et al., 2009; Vullo et al., 2017). Interestingly, neutralization mutations in the palm domain, such as D78N (rat ASIC1a (rASIC1a) numbering; D79 in cASIC1), E79Q (rASIC1a numbering; E80Q in cASIC1), E413Q (hASIC1a numbering; E412 in cASIC1) and E416Q (rASIC1a numbering; E417 in cASIC1) had stronger effects on the pH-dependence for activation of the ion channel in comparison to ACP mutants, rendering the constructs less sensitive to pH. H73N and deletion of H73 in rASIC1a and mASIC1a (H74 in cASIC1) resulted in mutants displaying low and no response to a drop in pH, respectively (Lynagh et al., 2018). For the last-mentioned mutant, the authors did not comment on the effect the mutant had on the surface expression of the ion channel, so failure in membrane insertion could also be a cause of the lack of response.

Most functional studies have been carried out on the human, mouse, and rat ASIC1a. The sequence identity between these ASICs and cASIC1 are ~89% providing a basis for making

connections to the pH-dependent gating mechanisms in human systems when using the cASIC1 models (Figure 1.6).

Computational and experimental studies have correlated the structural dynamics of cASIC1 to its gating mechanism. One study suggests based on mutagenesis, electrophysiological measurements, and free energy calculations that the protonation of acidic residues in the finger and thumb domains of the ACP increases the binding affinity between these two subdomains by the potential hydrogen bonds that can be formed upon protonation (H. Yang et al., 2009). This stabilization of interactions between these two subdomains induces conformational changes in the TMD, influencing it to twist, leading to an open gate (Figure 1.3A). An early computational study on the first ASIC1 structure showed that the ACP would expand (Figure 1.3A) when deprotonated and the authors suggested carboxyl-carboxylate pairs as potential proton-sensors: E299-D332, E339-E343 and D290-E363 (Shaikh & Tajkhorshid, 2008). Despite many efforts directed at identifying the proton-sensors, there is still no clear link to how proton-binding in regions of the ECD induces the opening or closure of the distal pore. Knowing precisely where protons bind, the identity of the proton-sensors and their local dynamics upon protonation would better our understanding of the gating mechanisms of ASIC1. Molecular dynamics (MD) simulations allow us to study the direct effects of protonation on potential proton-sensors and overall ASIC1 dynamics.

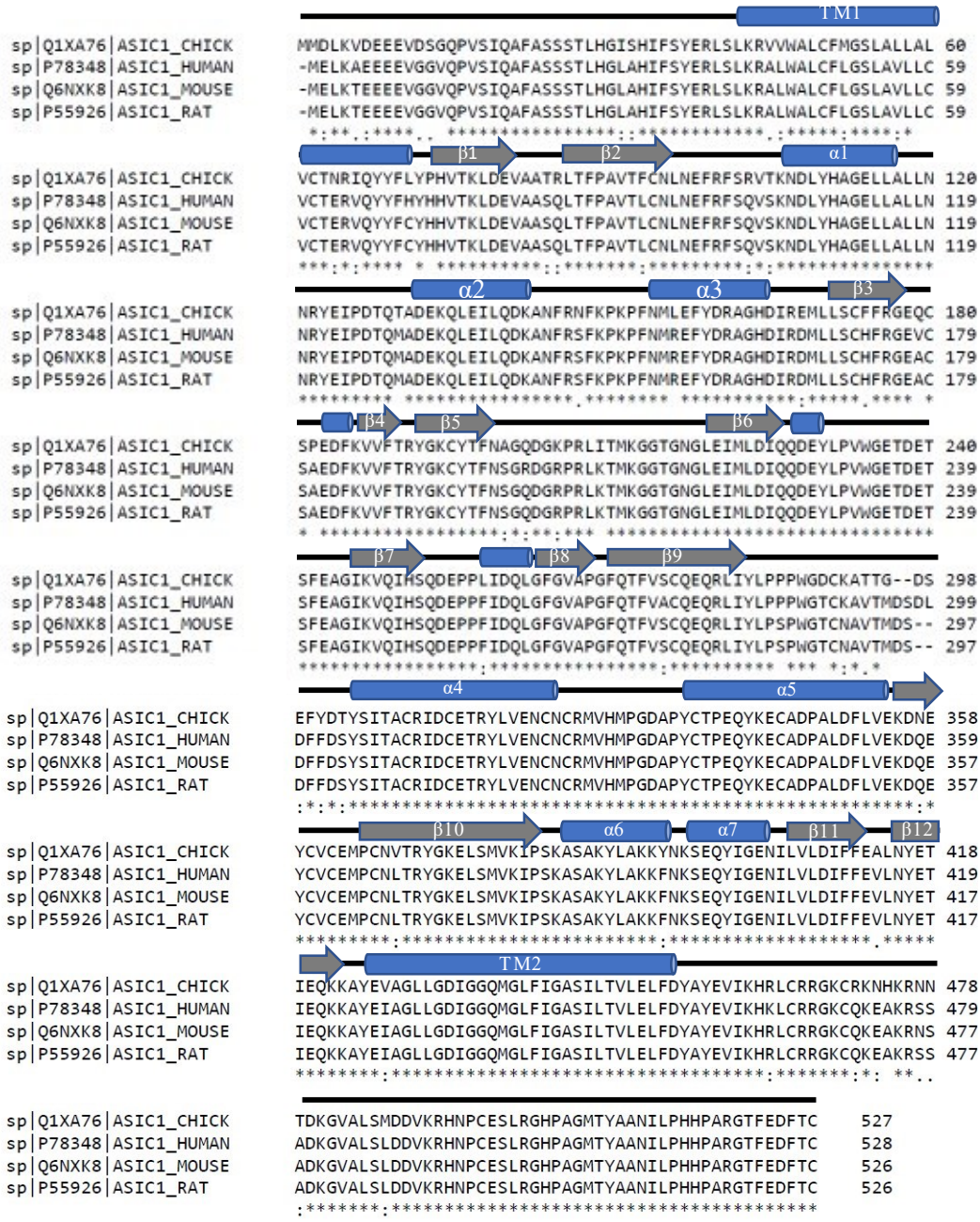

Figure 1.6 Multiple sequence alignment of ASIC1 across species.
Multiple sequence alignment of cASIC1 (Accession Code: Q1XA76), hASIC1a (AC: P78348), mASIC1a (AC: Q6NXK8) and rASIC1a (AC: P55926). The major secondary elements are illustrated.

1.5. Molecular Dynamics Simulations

Atomistic molecular dynamics (MD) simulations describe molecules at the atomic scale, providing a powerful tool for the study of molecular interactions, the validation of experimental work, and the conception of physiologically relevant predictions. This method utilises the force exerted on each atom by all other atoms in a system. From the calculated forces, Newton's second law is used to predict the displacement of each atom in the system as a function of time. MD simulations generate a trajectory, a sequence of atom coordinates of the entire system for each time step calculation (Hollingsworth & Dror, 2018). MD simulations have been implemented to study the dynamics of water and ions involved in protein function (Bernèche & Roux, 2001), ligand binding (Clark et al., 2016), in the refinement of X-ray crystal resolved structures (Afonine et al., 2012; Brunger & Adams, 2002) and to sample responses to perturbations involving a ligand (Dror et al., 2013; Wacker et al., 2017), mutations to the structure (Cordero-Morales et al., 2007), changes in protonation states (Liu et al., 2015; Rook, Miaro, et al., 2021) and the application of external forces (Delemotte et al., 2011; Y. Wang et al., 2021). It should be noted that in classical MD, covalent bonds cannot be formed nor broken, which is a challenge when studying a protein whose function is dependent on proton binding.

The forces are calculated in each step using a molecular mechanics force field. This force field includes functions and parameters that describe bonded (spring-like terms for covalent bond length and angles, and torsion angles) and non-bonded (Van der Waals and electrostatic) potential energies of a system (Figure 1.7**)**. Force fields are continuously being improved and have seen great improvements in agreement with experimental data in the last two decades (Lindorff-Larsen et al., 2012).

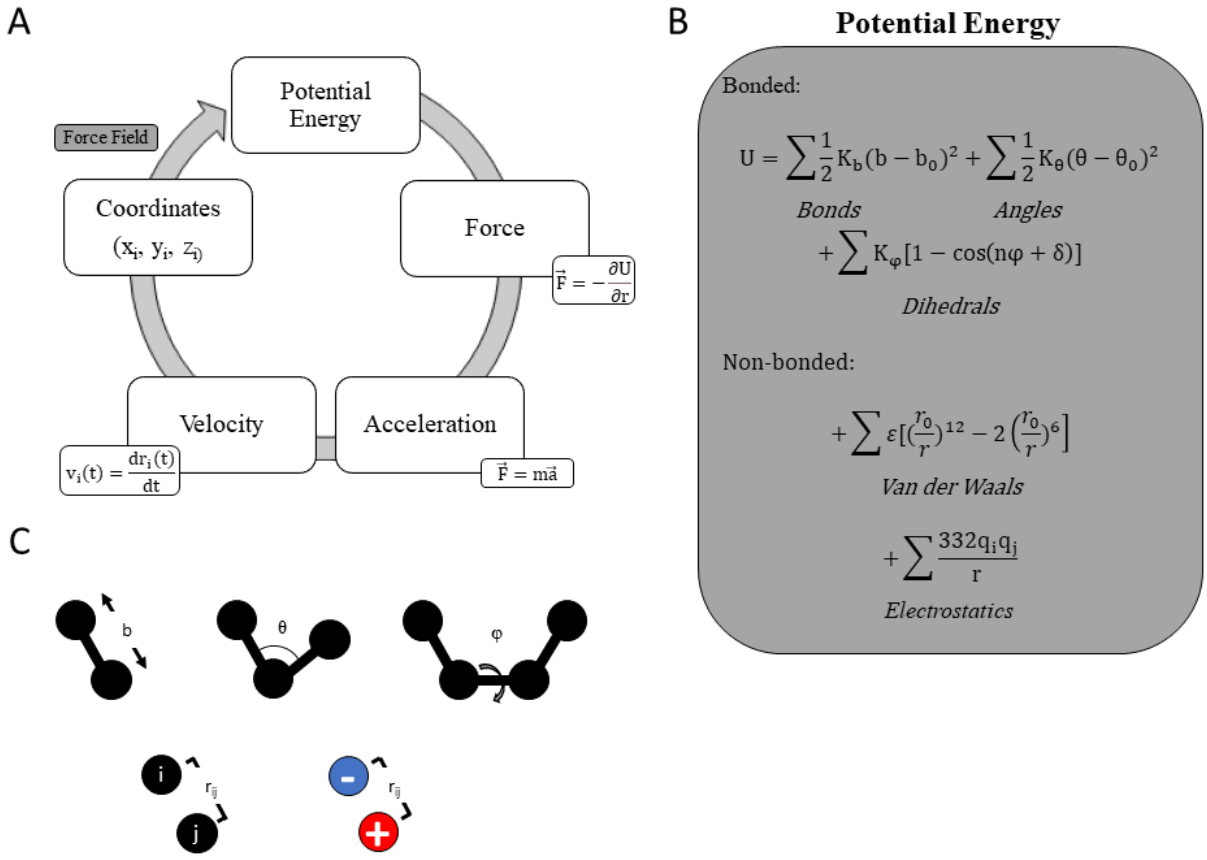

Figure 1.7 The molecular dynamics simulation cycle and molecular mechanics field energy terms.

A) The general MD cycle. An initial set of atom coordinates (r_i) is used to calculate the potential energy, force, acceleration, velocity, and the new set of coordinates through each iteration. B) The force field terms are used to calculate the potential energy at each timestep. It consists of bonded energy functions to describe bond stretching, angle bending and dihedrals between a set of atoms. It also consists of non-bonded energy functions, Van der Waals and electrostatic interactions. K_b is the spring constant describing the strength of a covalent bond, b_0 is the equilibrium bond length, K_θ is the angle force constant, K_θ is the equilibrium bond angle, K_φ is the dihedral amplitude, n is the dihedral multiplicity, δ is the dihedral phase, q_iq_j represent partial charges, r_0 is the Lennard-Jones radius and ε_{ij} is the Lennard-Jones well depth. C) Schematic of the bonded and non-bonded energy terms. i and j represent the atom of interest and all other atoms in the system, respectively.

However, these are still models and so there will always be uncertainty with the interpretation of MD results. The most popular force fields include AMBER (Robustelli et al., 2018), CHARMM (Huang et al., 2016) and OPLS (Harder et al., 2016). CHARMM36m has been specifically optimized for proteins, lipids and drug-like ligands and it is commonly used for membrane protein systems (Huang et al., 2016; Klauda et al., 2010; Vanommeslaeghe & MacKerell, 2012). The various force fields differ in the exact energy equation used, as well as in the set of parameters used to describe the equilibrium bond and angle distances (b_0, θ_0), the bond and angle strengths (K_b, K_θ), the dihedral amplitude (K_φ), the dihedral multiplicity (n), the partial charges (q_iq_j), the Lennard-Jones radius (r_0) and the Lennard-Jones well depth (ε_{ij}).

Another limitation of current atomistic MD simulations is the discrepancy between simulation timescales and the timescales of the biological events in question (Hollingsworth & Dror, 2018). With the rapid advancements in hardware (GPUs) and software for MD that can speed up simulation calculations, the simulation of biological timescales is becoming more attainable (Hollingsworth & Dror, 2018) but remains a challenge for large biomolecular systems. Short time scales also limit the ability of a system to sample conformational space effectively, as such, proteins can easily be trapped in a local minimum. Enhanced sampling methods have been developed to lower the energy barriers of systems to escape from their local minima and to speed up the process of rare biological events such as conformational changes. These methods include, e.g., umbrella sampling (Torrie & Valleau, 1977), steered MD (Grubmüller et al., 1996) and metadynamics (Laio & Parrinello, 2002). These three methods all use collective variables (CVs), a metric that describes a defined progression along a reaction coordinate (e.g. the C_α distance between D238 on the finger domain and D350 on the thumb domain is shorter in the open state (8.8 Å) than in the resting state (14.8 Å) in cASIC1), to bias the system towards a desired target.

Replica exchange MD (Sugita & Okamoto, 1999) and accelerated MD (Hamelberg et al., 2004) have also been useful in the sampling of transition pathways and intermediate states (Schlick & Portillo-Ledesma, 2021). In this research, we use a type of steered MD (targeted MD) in Chapter 3 to bias our system towards a pre-defined endpoint conformation. This bias is implemented with the use of an external biasing potential with a dependence on the RMSD between a starting and a target structure (Grubmüller et al., 1996). The theory behind targeted MD is explored in-depth in Chapter 3.

1.6. Protein Function and pH

Proteins are composed of a sequence of amino acids that encode their functions. Each amino acid residue can be characterized by its polarity and charge. Charged amino acids have ionizable side chains where the protonation states depend on pH and their local environment. These residues include aspartate, glutamate, histidine, lysine, arginine, tyrosine, and cysteine. The protonation or deprotonation events of ionizable side chains can have profound effects on the structure and the function of a protein. These effects can include changes in salt bridge and hydrogen bond interactions that can affect protein folding. Several proteins exist with a function that is dependent on the external pH due to changes in protonation states of their ionizable amino acid residues such as nitrophorins (nitric oxide carrier heme proteins) that can release nitric oxide (NO) by transitioning from a closed to an open conformation going from pH 5 to pH 7.5 (Andersen et al., 2000; Weichsel et al., 2000). The so-called Tanford transition in β-lactoglobulin A and B is characterized by a reversible conformational change that is pH-dependent, induced by

a change in the protonation state of E89, a residue buried in the hydrophobic core of the protein, that becomes exposed at pH 7.5 (Qin et al., 1998; Tanford & Taggart, 1961). More closely related are *G. violaceus* ligand-gated ion channels (GLICs), another proton-gated ion channel belonging to the family of pentameric ligand-gated ion channels (pLGICs).These cationic-selective ion channels undergo slow activation upon extracellular acidification (pH 7.4 to pH 5.0) and have been suggested to play a role in photosynthesis by taking part in the adaptation to changes in the pH of cyanobacterium (Bocquet et al., 2006).

Even more comparable to ASICs are proton-activated chloride channels (PAC), a new protein family (Ullrich et al., 2019; J. Yang et al., 2019) that are expressed in mammalian cells and they have roles in acid-induced cell death as well as tissue injury (Capurro et al., 2015; Sato-Numata et al., 2014; H. Y. Wang et al., 2007). These ion channels are also trimeric, and they share structural similarities with ASICs and ENaCs, having two transmembrane helices and a large ECD (Noreng et al., 2018; Ruan et al., 2020; Yoder et al., 2018). The ECD from a structural standpoint is similar to that of ASICs albeit PACs have smaller and more compact equivalents to the thumb and finger domains of ASICs. PACs activate upon extracellular acidification going from high pH (pH 8) to low pH (pH 4), leading to the conductance of chloride ions (Ruan et al., 2020).

K_a is the acid dissociation constant and describes the equilibrium constant between an acid (HA) and its conjugate base (A^-)

$$HA \rightleftharpoons H^+ + A^-$$

$$K_a = \frac{[H^+][A^-]}{[HA]}$$

$$pK_a = -\log K_a.$$

where H^+ represents a proton, HA is the acid and A^- is the conjugate base. The pK_a is the negative logarithm of the K_a and is used as a measurement of the strength of an acid. The pK_a is equivalent to the pH of a solution when the concentration of the acid and its respective conjugate base are equal. The pH of a solution of a weak acid can be related to its concentration and its conjugate base with the Henderson-Hasselbach equation:

$$pH = pK_a + \log_{10}(\frac{[A^-]}{[HA]}).$$

When the pH of a solution of a weak acid is equal to the pK_a of the weak acid, the concentration of the weak acid and its conjugate base are also equal. The proportion of both the weak acid and conjugate base populations in a solution can be calculated at a given pH. Each ionizable side chain (aspartate, glutamate, histidine, lysine, arginine, tyrosine, serine, threonine, and cysteine) has a 'table pK_a value' determined experimentally in water. In a protein, the pK_a of an ionizable amino acid side chain can be affected by its local environment and it will differ from the 'table pK_a value'. For example, a hydrogen-bond interaction between an acidic side chain and a histidine residue can result in a higher pK_a than what is predicted for a lone histidine amino acid in water and lower for the acid. This is due to the interaction stabilizing the proton on the histidine side chain. The pK_a value can act as an indicator of whether a titratable residue is to be protonated or not and this can be used to predict relevant interactions in the local environments of a protein.

Several methods exist to predict the pK_a of ionizable groups in biomolecules such as proteins and nucleic acids. One class of methods describes the environment of the system with an electrostatic continuum model, meaning that the solvent and ions are treated with a dielectric constant, instead of being explicitly modeled as in MD. This class of methods includes the use of

the Poisson-Boltzmann (PB) equation to account for the effects of solvent accessibility and of nearby ionizable residues on the titratable residues of interest (Jo, Vargyas, et al., 2008; C. Li et al., 2019; Lu et al., 2009; Rocchia et al., 2001). Another method of this class implements the generalized Born (GB) approach that uses approximations of electrostatic energies (Feig et al., 2004; Feig & Brooks, 2004). Often these calculations do not consider the flexibility and dynamic environments of titratable sites. The Multi-Conformation Continuum Electrostatic (MCCE) method predicts pK_a values accurately using different force fields (Georgescu et al., 2002; Rocchia et al., 2001; L. Wang et al., 2015). The other class of methods suitable for proteins are empirical-based methods. This class uses the three-dimensional structure of proteins to predict the pK_a using statistical fitting of parameters and terms describing the environment of a given titratable residue. Typically, empirical methods are the most cost-effective methods for large proteins (Bas et al., 2008; Cvitkovic et al., 2019; Milletti et al., 2009; Tan et al., 2013). These methods are less computationally intensive relative to the force field-based methods, as highly specialized calculations that take into account the solvent are not required. Calculations made by empirical approaches have become comparable to calculations generated by the more rigorous methods that require modeling (PBE and GB) (Davies et al., 2006; Stanton & Houk, 2008). PROPKA is a commonly used empirical pK_a prediction tool that functions with a three-dimensional structure input file. PROPKA was developed to be a computationally fast approximation for the prediction of pK_a values. PROPKA predicts the pK_a of ionizable amino acid residues by considering the perturbation to the model pK_a value influenced by the protein environment (Bas et al., 2008; Olsson et al., 2011). This is calculated for each ionizable amino acid residue by

$$\Delta pK_a^{w \to p} = \Delta pK_a^{desolv} + \Delta pK_a^{HB} + \Delta pK_a^{RE} + \Delta pK_a^{QQ}.$$

ΔpK_a^{desolv} accounts for the desolvation penalty described as a "loss of solvation energy" from the protein when protein atoms replace the solvent water around neighbouring residues. The next two perturbations account for intrinsic electrostatic contributions. ΔpK_a^{HB} describes the perturbation from favourable hydrogen-bond interactions between the ionizable residue, *i*, with the rest of the protein, that influences the deprotonation energy of a residue of interest. These contributions are partitioned into short-distance and long-distance contributions using a pre-defined cut-off distance, making this term an approximation (H. Li et al., 2005). Groups greater than the cut-off would not contribute to the hydrogen-bonding perturbation. ΔpK_a^{RE} is another intrinsic electrostatic contributor and it accounts for unfavourable electrostatic interactions (e.g. COO- - OC interactions would result in an increased pK_a). The parameters used for this calculation are similar to the ones used when calculating hydrogen bonding interactions since these interactions lack a proper data set to define well grounded parameters. This may lead to inaccuracies with pK_a calculations, however, this term is small relative to the other contributors. Finally, ΔpK_a^{QQ} describes contributions of a Coulombic nature that considers the electrostatic effect of a charge *j* on residue *i* that determines whether the pK_a would increase or decrease.

$$pK_{a,i}^{protein} = pK_{a,i}^{water} + \Delta pK_{a,i}^{water \rightarrow protein}.$$

The cumulative predicted pKa shift ($pK_{a,i}^{water \rightarrow protein}$) is added to the model value resulting in a final pK_a prediction ($pK_{a,i}^{protein}$) with terms that make the pK_a dependent on the exact conformations of the neighbouring side chains (Olsson et al., 2011).

We use PROPKA as the tool is generally fast and reported to be fairly accurate (Davies et al., 2006; Stanton & Houk, 2008); making it an efficient choice for making pK_a predictions along

the trajectory of simulations. Despite a reduced accuracy in comparison to the methods that require solvent modelling, the trade-off is worthwhile as PROPKA can predict the pK_a values of all residues in a three-dimensional protein structure in mere seconds. Additionally, we use it to calculate the pK_a as a function of time in our simulations allowing for pK_a measurements that take into account the dynamic nature of proteins. We are most interested in observing changes in pK_a as a response to changes in ASIC1 dynamics resulting from changes in protonation states. As such, PROPKA is effective for the purposes of this research.

1.7. Thesis Objectives

ASICs are proton-gated ion channels, however, it is unclear where protons must bind to induce the pH-dependent gating mechanisms involved in ASIC activity and how proton-binding leads to channel-opening. The goal of this study is to characterize the proton ligand-binding sites of ASICs to better describe the gating mechanisms of ASIC1. To do this, MD simulations and pK_a prediction tools are used to predict the important proton sensors of ASICs. We then link protonation states to channel dynamics to better understand the gating mechanism with targeted MD where the full transition pathways between the relevant conformational states of ASIC1s are simulated. Additionally, we combine the use of targeted MD with the prediction of the pK_a values of ionizable residues and monitor their change over time. Instances where pK_a values for a residue crosses the threshold of pK_a 5 at low pH and pK_a 8 at high pH can be thought to be protonation or deprotonation events. We hope to gain useful insights on proton ligand-binding and unbinding events and relate this to the pH-dependent channel gating mechanisms to describe

the full ASIC1 pathway. From our approach, we generate a list of the most-probable proton-sensors essential for channel function and describe their dynamics and their possible function in the context of existing functional data. This approach of studying pH-dependent protein dynamics could potentially be applied to other proteins with a pH-dependent function.

Chapter 2 : Protonation States Controlling Dynamics - Unbiased Molecular Dynamics Simulations of cASIC1

Section 2.3 of this chapter is published as:

Matthew L. Rook, Megan Miaro, Tyler Couch, Dana L. Kneisley, Maria Musgaard, David M. MacLean; Mutation of a conserved glutamine residue does not abolish desensitization of acid-sensing ion channel 1. *J Gen Physiol* 2 August 2021; 153 (8): e202012855. doi: https://doi.org/10.1085/jgp.202012855.

Author contributions:

M.L. Rook, D.L. Kneisley, T. Couch and D.M. MacLean conducted the electrophysiology experiments and analyzed the data. M. Miaro conducted the computational experiments and analyzed data. M.L. Rook, M. Miaro, M. Musgaard and D.M. MacLean interpreted the results and edited the manuscript.

Dr. Matthieu Chavent discussed the initial development of the hydrogen bond analysis used in this work.

2.1. Introductory Context

As discussed in Chapter 1, ASICs are trimeric, sodium-selective ion channels with a pH-dependent function (Waldmann et al., 1997). Despite the extensive studies that have been performed to improve our understanding of the structure and function relation of ASICs, it is not well understood how proton-binding induces conformational changes relevant to channel activity.

The ligand-binding mechanism involved in protein function is an important component in understanding the structure-function relationships. In most ligand-gated ion channels, the ligand-binding sites can be identified from structural studies with the visualization of an associated ligand in a structure. However, an agonist such as a proton, although possible, is very difficult to resolve using X-ray crystallography or cryo-EM, the techniques that were used to solve the current cASIC1 structures (Baconguis et al., 2014; Bohlen et al., 2011; Yoder et al., 2018). As such, MD simulations are used here to study potential proton binding sites as protons are explicitly accounted for in the model.

Previously, we combined MD simulations and pK_a predictions to narrow down a list of potential proton-sensors in ASIC1 by simulating the ion channel at "low-pH" and "high-pH", defined as a pH ~5 and ~8, respectively. As explained in the first chapter, these pH values are generally used in electrophysiological studies of ASICs to drive the channels to the open (pH 5-5.5) or the resting states (pH 8). This was done by either fully protonating every ASP, GLU and HIS residue ("low-pH"; neutralizing ASP and GLU and treating HIS as positively charged) or leaving them unprotonated ("high-pH"), with histidine singly protonated (i.e. neutral) and ASP and GLU negatively charged. These amino acid residues are chosen as they are more likely to

undergo changes in protonation upon extracellular acidification. The simulations were performed for the open, desensitized, and resting states. This was followed by pK_a prediction of all ASP, GLU and HIS residues in each simulation as a function of time, using snapshots every 0.5 ns. From this analysis, a list of the average pK_a values for each residue in each system was compiled and used as a predictor for the pK_a of these residues in the functional states induced by the activating and inactivating pH conditions. From this list, we narrowed down potential proton-sensors by including residues that showed pK_a predictions dependent on the imposed "pH" in the form of the applied protonation states.

Actual constant pH values are difficult to simulate as it implies the modelling of explicit, positively charged protons in free solution. If protonation events were possible with conventional MD alone, given the small size of our simulation box, even a pH of 5 would only equate to less than one hydronium ion in the system. Using these same conditions, if there were to be a protonation event, introducing more hydronium ions during a simulation would change the net charge of the system (Rook, Musgaard, et al., 2021). However, MD simulations must always have a neutral charge. This is because the particle mesh Ewald (PME) method that calculates long-range electrostatic interactions for the entire system requires the system to be neutral (Darden et al., 1993). Charges are usually balanced by the addition of counterions during the setup of a simulation system.

We could also predict the protonation states of each residue by comparing the pK_a to pH 5 or 8, values we refer to as "low-pH" and "high-pH" (Table 2.1). Applying the predicted protonation states in simulations were observed to have stabilizing effects on their respective protein structures during MD simulations, in comparison to simulating under the two pH conditions.

Table 2.1 Predicted protonation states of each functional state of cASIC1.
The following protonation state configurations were applied to the subsequent functional states in the gating cycle from activation to desensitization to recovery in section 2.1. In sections 2.2 and 2.3, the protonation states are applied to their respective structures (resting protonation state on the resting state, open protonation on the open state, and desensitized protonation state on the desensitized state) unless otherwise specified. H denotes a protonated residue (neutralizing Asp/Glu; making His positive). Highlighted are residues thought to be potential proton-sensors from previous research (Miaro, 2020).

Ionizable Residue	*Resting State*	*Open State*	*Desensitized State*
H74	-	H	-
E80	-	H	-
E98	-	H	H
H111	-	H	H
E220	-	-	-
E239	-	-	H
H328	-	H	H
D346	-	H	-
E354	-	H	H
E374	-	H	H
D408	H	H	H
E412	-	H	H
E417	-	-	H
D433	-	-	H

As such, these protonation schemes (Table 2.1) are used as the default for all following simulations unless otherwise specified.

This chapter aims to characterize the likely proton-binding sites to better understand the structure-function relationship of the pH-dependent gating mechanism of cASIC1 function. This consists of simulating different agonist-bound forms of the protein. The effect of varying protonation states on the dynamics of cASIC1 is explored in the following.

2.2. Experimental Procedures

Preparation of the cASIC1 models

All systems were set up using existing cASIC1 models (*Gallus gallus*) for the open (PDB ID 4NTW) (Baconguis et al., 2014), the resting (PDB ID 5WKU) (Yoder et al., 2018) and the desensitized states (PDB ID 4NYK) (Gonzales et al., 2009). The three crystal structures were chosen based on their respective resolutions and structure completeness, relative to other existing structures. Missing residues and atoms were filled using Modeller v9.21 (Webb & Sali, 2016). Spatial restraints from the template sequence (original structure) were applied to the full sequence to create comparative models with "filled in" residues. Only residues with missing atoms were selected to be refined. Non-missing residues were left as is. The open state structure spans residues 42 to 455, 42 to 458 (459 in chain B) for the resting state, and 45 to 456 for the desensitized state. The full cASIC1 sequence would span from residue 1 at the N-terminal to 527 at the end of the C-terminal in the cytoplasmic domain (Jasti et al., 2007), however, we did not attempt to model the N- and C-terminal sections. Each model was oriented for proper placement in a membrane bilayer by aligning the atom coordinates with the corresponding structures in the Orientation of Protein Membranes (OPM) database (Lomize et al., 2012).

All co-crystallized chloride ions from the PDB structures, if existing, were kept in the systems (only in the open and desensitized states). Chloride has been reported to affect desensitization in cASIC1 but this is not explored in the thesis (Kusama et al., 2010). Water molecules were removed only from the desensitized state structure as they caused issues for the simulation setup. There have not been any reports of water molecules being essential for pH-dependent ASIC activity. The resting state structure does not contain crystal water molecules.

Simulation System Setup and Production Run

The protein membrane systems were set up in GROMACS 2019.4 (Abraham et al., 2015), with a background protonation setup as in Table 2.1 (unless otherwise specified). Protonation states were set interactively using the *pdb2gmx -asp, -glu, -his* command. The protein models were inserted into a palmitoyl-oleoyl-phosphatidylcholine (POPC) bilayer generated by the CHARMM-GUI membrane builder (Jo, Kim, et al., 2008) using InflateGRO (Kandt et al., 2007). Each system was built in a 120 Å X 120 Å X 161 Å triclinic box. The Charmm36m force field was utilized (Huang et al., 2016). The system temperature was set to 310.15 K. The TIP3P water model (Mark & Nilsson, 2001) was used to fill the box with solvent. Sodium ions and chloride ions were generated to neutralize the system for a final concentration of 0.15 M NaCl.

Equilibration and Production Runs

All systems were minimized for a maximum of 5000 steps or until convergence, then equilibrated in six steps for a total of 375 ps. The first three equilibration steps in the NVT ensemble use a 1-fs time step and each is 25 ps long. The last three equilibration steps in the NPT ensemble use a 2-fs time step and each is 100 ps long. Position restraints were progressively removed during equilibration as suggested in the default CHARMM-GUI protocol. Periodic boundary conditions were applied. The Verlet cutoff scheme was applied with a force-switch modifier from 10 Å with a cutoff of 12 Å. The cutoff used for short-range electrostatics was 12 Å and the particle mesh Ewald (PME) method was used for long-range electrostatics (Darden et al., 1993; Essmann et al., 1995). A Berendsen thermostat and a Nose-Hoover thermostat (Hoover, 1985; Nosé, 1984) were used for all equilibration steps and production run steps, respectively, to maintain the temperature at 310.15 K for all steps. The pressure was

maintained at 1 bar using semi-isotropic pressure coupling in the final four steps of equilibration and for the production run using the Berendsen barostat (Berendsen et al., 1984) and the Parrinello-Rahman barostat (Parrinello & Rahman, 1981), respectively. The LINCS algorithm was applied to constrain covalent bonds involving hydrogen to their default length (Hess et al., 1997). The production runs in section 2.1 were run from a range of 100 ns to 600 ns long with at least three repeats of 100 ns for each system, in the NPT ensemble. Furthermore, the protonation state of a target state (Table 2.1) was applied to the native functional state to simulate transition pathways. The production runs in section 2.2 consist of systems with extensive protonation state sampling of residues in the acidic pocket (ACP) and the palm domain. 35 unique simulations were prepared for all three functional states: 14, 13 and eight simulations for the open, desensitized, and resting states, respectively. Each simulation was run for 25-ns in duplicates. Residues in the ACP and palm domains were sampled: E98, D238, E239, D346, D350, E354 in the ACP and E80, E412, E417 and E374 in the palm domain.

SASA Calculation of the Central Vestibule

The overall solvent accessible surface area (SASA) is represented as the average SASAs in the following group of residues: 78, 80, 275, 277, 279, 281, 368, 370, 372, 374, 410, 412, 417 and 419, for all subunits. The selection is inclusive of all residues with a side chain within the central vestibule. A radius of 1.4 Å is used on the selection to find points exposed to solvent that are within this range. This calculation was performed for each chain individually, and each frame. The calculations were performed with VMD (Humphrey et al., 1996). Plots were generated in Gnuplot Version 2.5.

Measurement of Minimal Distances

Distances between hydrogen bonding donor and acceptor atoms (OD1, OD2, OE1, OE2, NH1 and NH2) between a set of ionizable residues within the acidic pocket were measured for each frame. If multiple interactions were possible between two residues, the shortest possible distance was recorded. The measured interactions include residues E98, R191, D238, E239, D346, D350, and E354. Interactions measured are as in Figures 2.5, 2.6 and Appendix A Figure 4.8. Calculations were made every 0.01 ns for eight simulations of the resting state, 14 simulations of the open state, and 13 simulations of the desensitized state, each with a unique protonation configuration. Each system was run for 25 ns in duplicate. The calculations were performed with VMD (Humphrey et al., 1996). The histograms (Figure 2.5, 2.6 and Appendix A Figure 4.8) were made with pyplot.hist from Matplotlib 3.2.2 using the density parameter to generate a normalized probability density function that includes data from each simulation of the resting, open or desensitized states. Plots were generated in Matplotlib 3.2.2.

Hydrogen-bond Analysis

Hydrogen bonds were calculated as described in (Rook, Miaro, et al., 2021). The protonation configuration for the desensitized state (Table 2.1) was used on the desensitized state (PDB 4NYK (Gonzales et al., 2009)) for the "wild-type" simulations. The protonation states of E80, E412 and E417 were sampled thoroughly for eight unique simulations (Figure 2.7). Each simulation was run for 100 ns in triplicate. The Q277N was made by manually mutating Q277 to an ASN. The same base protonation configuration for a desensitized state was used. The Q277N system was also run for 100 ns in triplicate. To calculate hydrogen bonds, every 10 ps, potential hydrogen bonds between the donor or acceptor atoms of E80, Q277, E412, L414, and E417 in

the palm domains, were measured for all three subunits. The donor atoms consist of E80HE2 (if protonated), Q277NH1, Q277NH2, E412HE2 (if protonated), and E417HE2 (if protonated). The acceptor atoms consist of E80E1, E80E2, Q277OE1, E412OE1, E412OE2, L414O, E417OE1 and E417OE2. Hydrogen bonds were calculated with the 4.3.1 Hydrogen Bond Analysis module (Smith et al., 2019) of MD Analysis (Gowers et al., 2016; Michaud-Agrawal et al., 2011). The analysis implements an adapted version of M. Chavent's Jupyter Notebook accessible on GitHub (https://github.com/MChavent/Hbond-analysis) (del Toro et al., 2020). A default cutoff of 3.0 Å was used for the donor-acceptor distance and a cut-off of 150° was used for the donor-hydrogen-acceptor angle. Residues that could participate in equivalent hydrogen bonds (i.e. E80OE1 and E80OE2) were summed for a single percentage representing the interaction (Figure 2.8).

2.3. Unbiased Simulations of Protonation Swaps

As discussed in the introductory section above, in prior work, we have used pK_a prediction in conjunction with unbiased MD simulations to predict the protonation states of ionizable residues for each functional state (resting, open and desensitized). These predicted protonation schemes were then imposed onto their respective structure to observe the effects on dynamics with the expectation that the structures would be stabilized with our predictions. We identified protonation schemes that appear to stabilize each of the three functional states. These protonation states, although not experimentally validated, are used throughout the thesis as they do not

perturb the structures to a great extent in comparison to our previous “low-pH” and “high-pH” simulations that emulated activating and deactivating conditions, respectively (Miaro, 2020).

First, we sought to test the above-mentioned protonation states and observe if they would perturb the structure of the ion channel in a simulation, indicative of the beginnings of a conformational change. To do this, the pre-determined predicted protonation states (Table 2.1) were imposed on the pre-functional state, meaning that we used the protonation state of our target functional state on the structure we want to undergo a conformational change (e.g., for activation, the protonation states predicted to stabilize the open state are applied to the resting state. For desensitization, the protonation states predicted to stabilize the desensitized state are applied to the open state, and the protonation states predicted to stabilize the resting state are applied to the desensitized structure for recovery from desensitization). By imposing the predicted protonation states of a target state onto the pre-state (i.e. open state protonation is imposed onto the resting state structure to simulate the activation pathway), the systems are then analyzed to detect changes to the starting structures related to a relevant conformational change. Four systems were simulated, two resting state structures with either an open-state stabilizing configuration or simply E98 and D408 protonated (E98H/D408H). The latter was simulated as D408 has a high a pK_a even in the resting state, suggesting that it would be protonated, while E98 has the highest average pK_a (~8-10) in comparison to all other acidic residues in the open state and we hypothesized it to be a proton-sensing residue important in the driving steps of activation (Miaro, 2020). The other two systems were of the open state with a desensitized state-stabilizing protonation, and a desensitized state with a resting state-stabilizing protonation configuration, to emulate desensitization and recovery from desensitization, respectively (Table 2.1). The simulation times of systems emulating activation and desensitization were extended

beyond the initial 100-ns of the production run as these are the quickest events and would be the most likely to show indications of a transition. Even so, the simulation times used are likely insufficient as activation and desensitization take place on the ms to s time-scales (Gründer & Pusch, 2015; Hesselager et al., 2004).

The first step in the analysis is to verify the stability of our systems. This was done by measuring the C_α root mean square deviation (RMSD) over time, using the starting structure as a reference. The start of a conformational change is expected to have higher RMSDs relative to simulations where we use a "standard" protonation scheme (e.g. simulations of the open state with an open-state stabilizing protonation state should have little changes in RMSD over time) (Figure 2.1). The RMSDs were measured for the full constructs, the TMD (residues 47 to 70 and 427 to 453) and the ECD (residues 71 to 426). By imposing the protonation state of our target structure onto our starting structure, in both the second resting state system (E98H/D408H) and in the desensitization systems (Figure 2.1B, C), the overall RMSDs of the proteins exhibit clear increases as a function of time, relative to the resting state with open protonation and desensitized state with the resting state protonation. Strangely, the systems of activation (resting with open protonation) and recovery (desensitized to resting) exhibit RMSD values that do not appear to increase to the same extent from the beginning to end of the simulations, relative to the previous two systems (Figure 2.1A, D). These simulations have an $RMSD_{ECD}$ that displays a moderate increase in the first 100 ns, and they tend to remain in a similar conformation for the remainder of the simulation time.

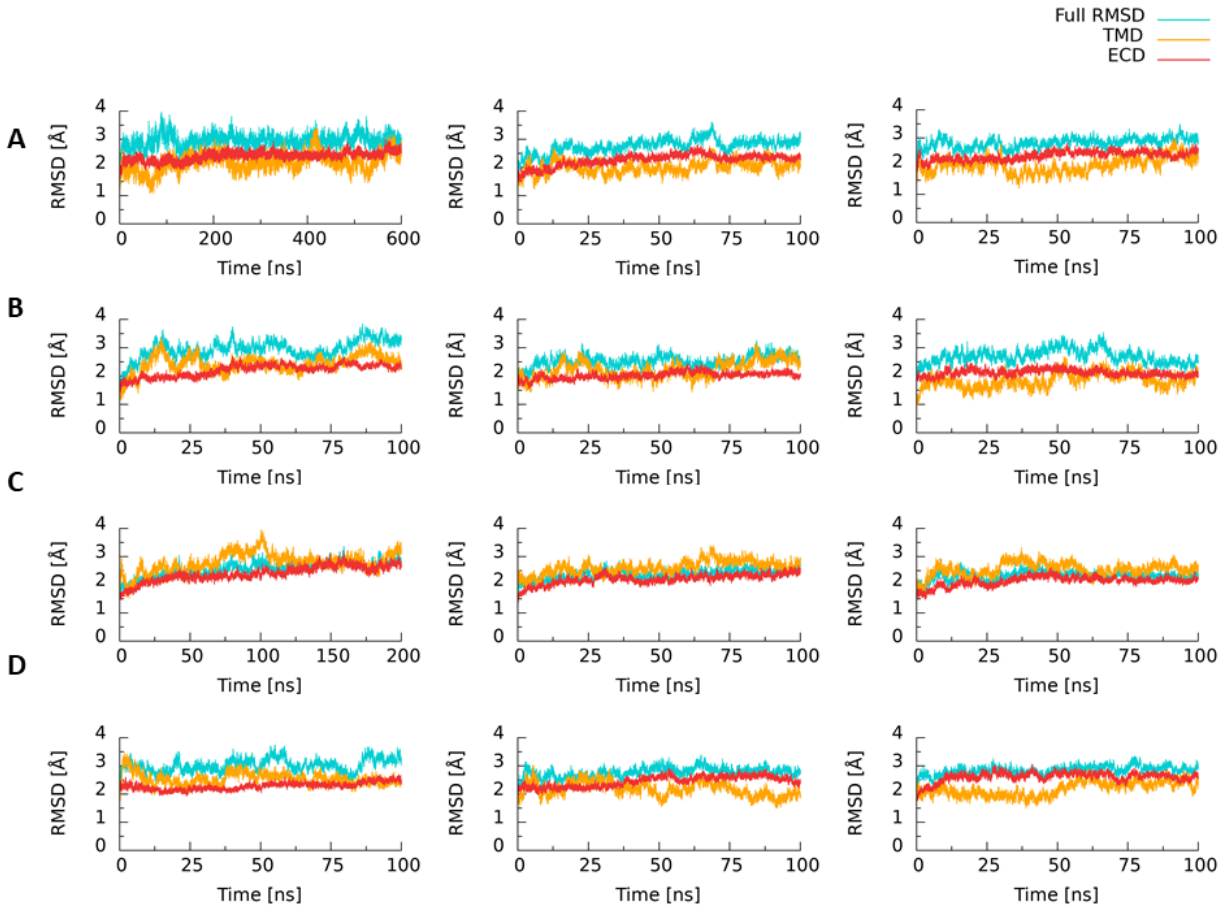

Figure 2.1 RMSD measurements of each protonation-swap system.
The C_α RMSD between the starting structure and each frame is measured for the A) open protonation state configuration on the resting state, B) E98 protonated resting state structure, C) desensitized protonation state configuration on the open state and D), resting state protonation configuration on the desensitized state. The RMSDs of the entire channel, the TMD (residues 42 to 72 and 426 to 459 for the resting state; 45 to 72 and 426 to 456 for the open state; 45 to 72 and 426 to 455 for the desensitized state) and the ECD (residues 73 to 426) are shown. On average, the full RMSDs (turquoise in the plots above) for our previous simulations with protonation states matching the structure (e.g. open protonation state on the open state) were ranged from ~2 – 2.8 Å for the resting, open and desensitized states (~2.5 Å, ~2 Å and ~2-2.5 Å, resting, open and desensitized, respectively). Each of these simulations was 25 ns in length but the systems converge within this time due to the stabilizing effects of the chosen protonation states.

Overall, the simulations emulating activation with the resting state E98H/D408H (Figure 2.1B) and desensitization with the open state imposed with a desensitized protonation state (Figure 2.1C) display clear perturbations to their equilibrium. Unexpectedly, even after simulating for 600 ns (Figure 2.1A), the resting state with the open protonation state imposed, the average RMSD barely reaches 4 Å.

This indicates that the protonation states used are not sufficient to drive conformational changes. This could be because the timescales we use are insufficient to sample the beginnings of a conformational change or the protonation states that we use are incorrect.

Other factors than the protonation state configuration, such as random fluctuations, may also affect the RMSD. To observe changes indicating the start of relevant conformational changes, state-specific measurements such as water hydration in the pore (Figure 2.2, Appendix A Figure 4.2, Controls: Appendix A Figure 4.3), contraction or expansion of the acidic pocket (ACP) (Figure 2.3, Appendix A Figure 4.4, Controls: Appendix A Figure 4.5) and the solvent-accessible surface area (SASA) of the central vestibule (Appendix A Figure 4.6, Controls: Appendix A Figure 4.7) are also considered. As discussed in the Introduction chapter, these collective variables can be distinguished from the crystal structures (Baconguis et al., 2014; Gonzales et al., 2009; Jasti et al., 2007; Yoder et al., 2018).

The water counts in the pore permeation pathway along the transmembrane domain (TMD) were measured to observe changes in the hydration of the pore, indicating opening or closure, consistent with activation and desensitization, respectively. Each system is either dehydrated (resting and desensitized state structures) or hydrated (open state structure) as expected for each respective starting functional state.

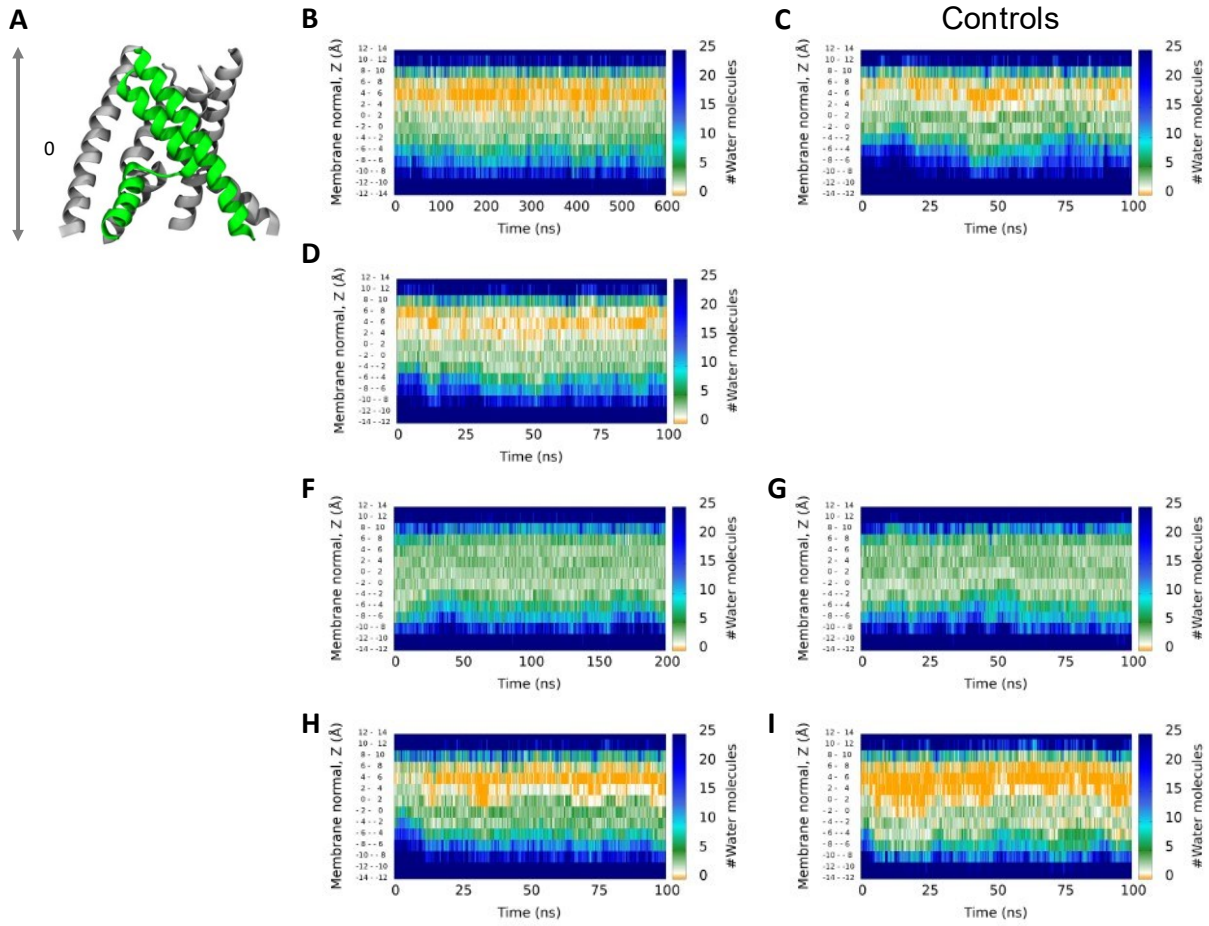

Figure 2.2 Pore hydration.
Representative plots of the number of water molecules along subsections of the membrane normal along the pore permeation pathway. A) TMD of cASIC1 scaled to the z-axis of the pore hydration plots. B) Resting state with open protonation, D) resting state with E98 protonated, F) open state with desensitized protonation and H) desensitized state with resting protonation, respectively. To the right are controls: C) resting with resting protonation, G) open with open protonation and I) desensitized with desensitized protonation. Note the different time scales of the x-axis. All repeats are shown in Figure Appendix A2.1.

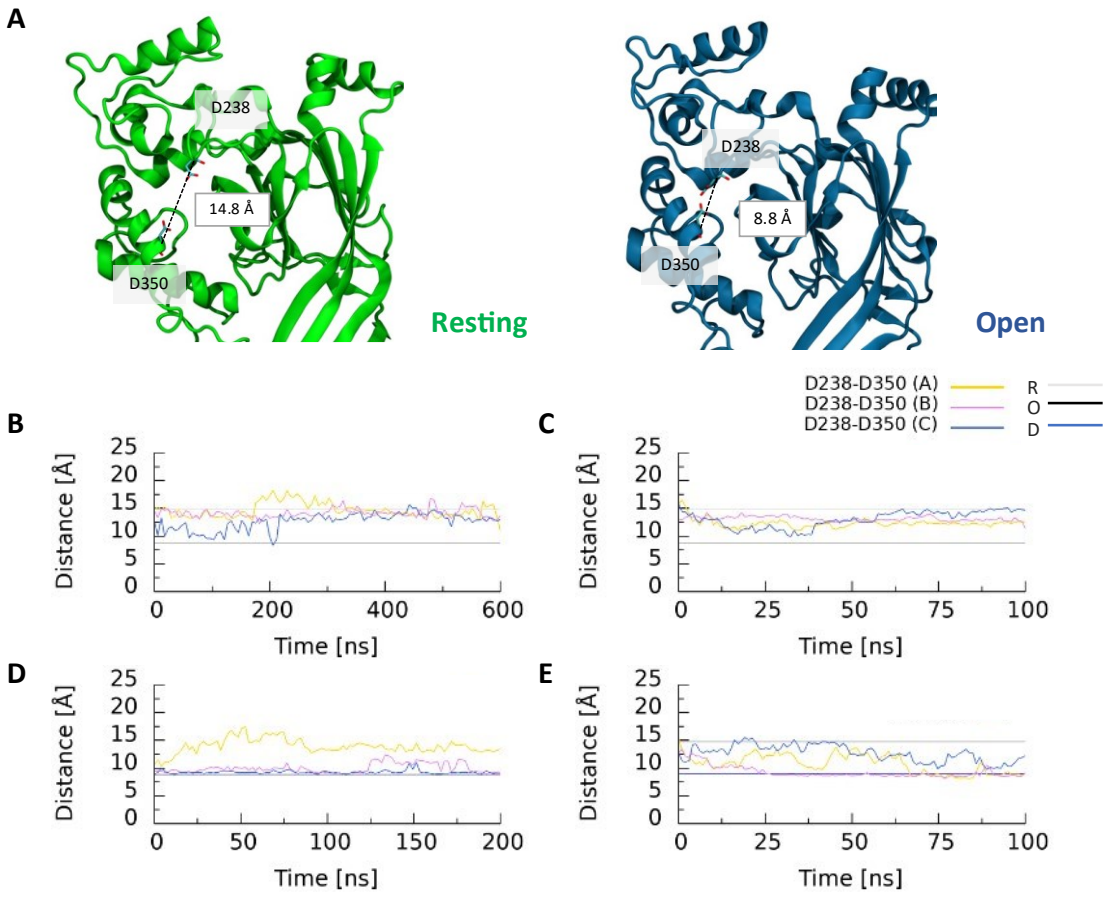

Figure 2.3 Representative Cα distances in the acidic pocket between D238 and D350. (A) Close-up of the acidic pocket of the resting state (left, green) and open state (right, blue) crystal structures. Depicted are the average Cα distances between D238-D350 for the resting state (PDB 5WKU) and open state (4NTW), respectively. (B) D238-D350 distances measured from the resting state with open protonation, (C) resting state with E98 protonated (final structure), (D) open state with desensitized protonation, and (E) desensitized state with resting protonation for each chain (A, yellow; B, violet and C, blue, respectively). R (gray), O (black) and D (blue) represent the average distance between the Cα atoms of D238 and D350 for all three chains in the resting state (14.78 Å), open state (8.81 Å), and desensitized state (9.02 Å) crystal structures. R, O, D standards are drawn twice on each plot to represent the start and end of a conformational transition (i.e., the plots for "activation" (B) have the average distances for the resting and open state crystal structures only).

Additionally, each system displayed no obvious changes in water counts throughout the simulations (Figure 2.2, Appendix A Figure 4.2). Thus, no channel openings or closures are observed in response to the protonation swaps.

Another indicator of activation and recovery from desensitization is marked by the collapse or expansion of the ACP, respectively. To monitor this, representative distances between the C_α atoms of D238 and D350, two acidic residues in the ACP that were hypothesized to hydrogen-bond in the low-pH open state (Jasti et al., 2007), were measured throughout our simulations to capture this motion (Figure 2.3 and Appendix A 4.4). First, in the two resting state systems, the distances begin at the native crystal structure distances (14.4 Å) and end by converging to similar distances (~ 12-15 Å) (Figure 2.2, B and C).

Interestingly, the distances occupy a lower range than the crystal structure for around 25 ns during the simulation of the resting state with the E98H system (Figure 2.3C). In the "desensitization" system, the distances remain within the range of the open/desensitized states crystal structure distances (8.8 Å) apart from chain A (Figure 2.3D). Finally, in the "recovery" system, the distances at the start of the simulation are higher than the average distances taken from crystal structure of the desensitized state. The distances gradually decrease during the simulation to occupy distances resembling the desensitized state (Figure 2.3E). Overall, no changes were observed that would indicate a commitment to one of the three major conformational changes in the ASIC1 transition pathways, despite the brief occupancy of target-like distances in the "recovery" systems.

The final metric was the SASA of the atoms of residues lining the central vestibule with side chains facing the inner vestibule, as this region is expected to expand in recovery from

desensitization, and to contract in activation, and even further in desensitization from a comparison of the crystal structures used (Baconguis et al., 2014; Gonzales et al., 2009; Yoder et al., 2018). Volumetric measurements of the central vestibule with CASTp have also predicted similar trends (Bargeton et al., 2019). In our simulations, only the recovery system displayed an expansion of the central vestibule, with the SASA of all three chains converging at the average SASA of the resting state crystal structure (Appendix A Figure 4.3D). The first system emulating "activation" (resting state structure with an open protonation state) displayed a final SASA that was lower than that of the resting state structure but, not low enough to reach the SASA of the open state crystal structure. The simulations emulating "desensitization" (the open state with desensitized protonation) displayed expansion of the central vestibule, a behaviour contrary to our expectations. Again, a comparison of the open and desensitized crystal structures would suggest that desensitization leads to an even more contracted central vestibule (Bargeton et al., 2019; Gonzales et al., 2009; Jasti et al., 2007). The SASAs in our simulations of desensitization were instead, on average, more akin to that of the resting state crystal structure.

We do not know at what rate a particular domain would transition relative to another domain and whether one local conformational change is dependent on another distal one. Overall, while increased RMSD values were observed for the simulations targeting activation and desensitization, there were no indications of a conformational change in any system. Potential reasons for the lack of conformational changes are covered in the discussion. From looking at global conformational changes that were unattainable with the methods used, we take a more detailed focus on the ACP and palm domains of ASIC1, regions attributed to pH-sensing.

2.4. Effects of the sampling of protonation states on ionizable residues in the ECD

The ACP was originally thought to house the proton-sensors that are the driving force for pH-sensitive ASICs activation, inferred from the visualization of carboxyl-carboxylate interactions in this region at low-pH and with mutagenesis studies of D346 and D350 in the ACP that resulted in a reduced pH-sensitivity in ASIC1 (Jasti et al., 2007). However, there has been increasing evidence these acidic pairs in the ACP are not crucial for pH-dependent channel function. Nonetheless, the ACP may still appear to play an important allosteric role in proton-dependent gating mechanisms of ASIC1 (Paukert et al., 2008; Rook, Musgaard, et al., 2021; Vullo et al., 2017). However, other than the D238-D350 and E239-D346 hydrogen-bonding pairs identified in the first cASIC1 crystal structure (Jasti et al., 2007), it is unclear what other interactions may form in the ACP which could contribute to the stabilization of the low-pH states (open and desensitized). Protonation events upon extracellular acidification can change electrostatic interactions contributing to the stabilization of a given conformation and this could potentially play a role in the transition from one state to another as well.

Here, the distances between the side chains of neighbouring residues in the ACP are measured to approximate the frequency of two residues being within hydrogen-bonding or coulombic interaction distance. Interaction distances with high occupancy would thus indicate stable interactions that potentially are pH-dependent and could be related to channel function. The distances were measured with varying configurations of protonation states as well, to see the effect on protonation and the stability of the observed interactions. Differences in interactions between a low-pH and high-pH state may point toward the formation of pH-dependent interactions. Furthermore, ligand-binding is directly related to the formation of specific interactions, thus protonation of the susceptible proton-sensors may also be similar to ligand-

binding in a receptor as protonation events would provide these ionizable residues (such as ASP, GLU and HIS) the ability to form electrostatic interactions such as hydrogen bonds, as well as to lose interactions. The formation and loss of these pH-dependent interactions can be crucial for pH-dependent ASIC1 function.

To characterize these interactions per functional state, the minimum distances between the acceptor and donor atoms of seven titratable residues in the ACP were measured. These residues include E98, R191, D238, E239, D346, D350 and E354. These residues were chosen since they are in proximity to each other and past simulations have shown that interactions may exist between their side chains in the open and desensitized states (Miaro, 2020). A total of 11 interactions consisting of 1:1 pairs of the above residues were measured throughout the simulations. The potential interactions to be measured were based on the analysis of previous simulations and the proximity of residues in relation to each other. Interactions that are structurally unlikely to occur were not considered. In this analysis, we use the definition that a hydrogen bond has a donor and acceptor atom distance of 3.5 Å or less to observe the potential of an existing interaction. Ideal hydrogen bond donor-acceptor-hydrogen angles were not considered in this analysis however, we can still describe the approximate positions of these residues relative to each other. The frequency of distances for each potential interaction in each simulation system is shown below (Figures 2.5 and 2.6) as an approximation of a probability distribution function. We make the assumption that a change in the protonation states of neighbouring residues surrounding the interaction does not affect the strength of the observed interaction of interest. This assumption is not completely true since the pK_a is directly affected by solute, ions, and the side chains of other nearby residues as was discussed in the Introduction Chapter. To make the data manageable, we analyze our data with this assumption.

First, protonation states are shown to affect the stability of interactions of interest. Between two interacting acidic residues with carboxylic groups (ASP, GLU), three possible protonation configurations can exist. Either both groups have no protons (0 H), one residue is singly protonated (1 H), and both residues are singly protonated (2 H) (Figure 2.4). Often, having a proton on a single residue in a pair (1 H) favours the frequency of an interaction between the two. From our results, having both residues either protonated or unprotonated greatly reduces the frequency of distances that fall into the range that can be considered as a hydrogen-bond interaction (Figures 2.5, 2.6). It is the interacting partner with the highest average pK_a that has a stronger hold on the proton and thus the highest frequency of distances within a hydrogen-bond interaction range.

For example, on average in the open, desensitized, and resting states, E98, a buried residue in the acidic pocket, has a pK_a of ~8-9, ~9-10, and ~6**,** respectively, while its interacting partner, E239, has an average pK_a of ~7-8, ~7-9, and ~5 (Miaro, 2020), respectively. Hydrogen-bond interactions are highly favoured when only E98 is protonated in an E98-E239 pair in the low-pH (open and desensitized) states (Figure 2.5A).

In the simulations of the open state, the interaction with the highest frequency exists between a protonated E98 and an unprotonated E239. In the simulations of the desensitized state, the same protonation state is favoured but at a lower frequency. These simulations of the desensitized state also have an increase in hydrogen bond like distances in the E98-/E239H protonated configuration (E239 is protonated instead of E98). Finally, E98-E239 interactions are not favoured in the resting state as expected since the crystal structure would suggest that the two side chains are too distanced to interact (Yoder et al., 2018).

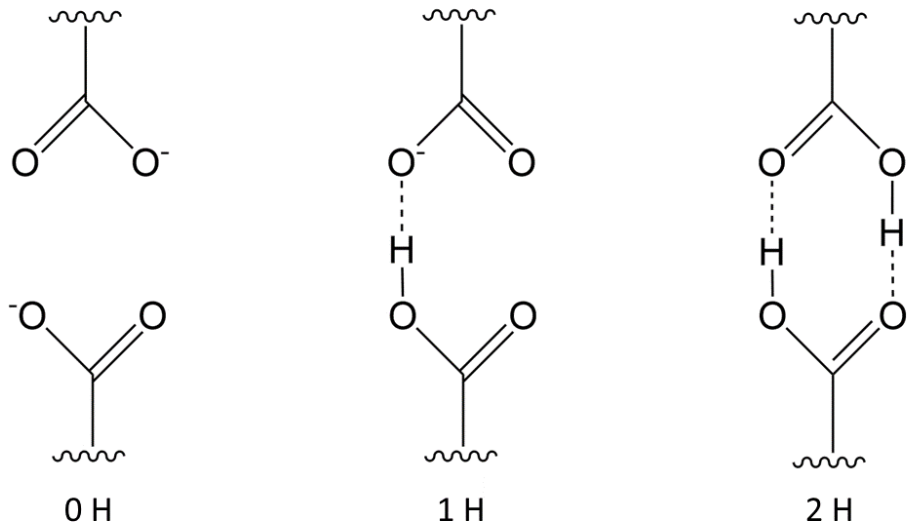

Figure 2.4 Acidic carboxyl-carboxylate pairings.
Interactions between two carboxyl side chains with zero (0 H), one (1 H) or two (2 H) protons. Our simulations depict that a singly protonated carboxyl group is favoured in carboxyl-carboxylate interactions.

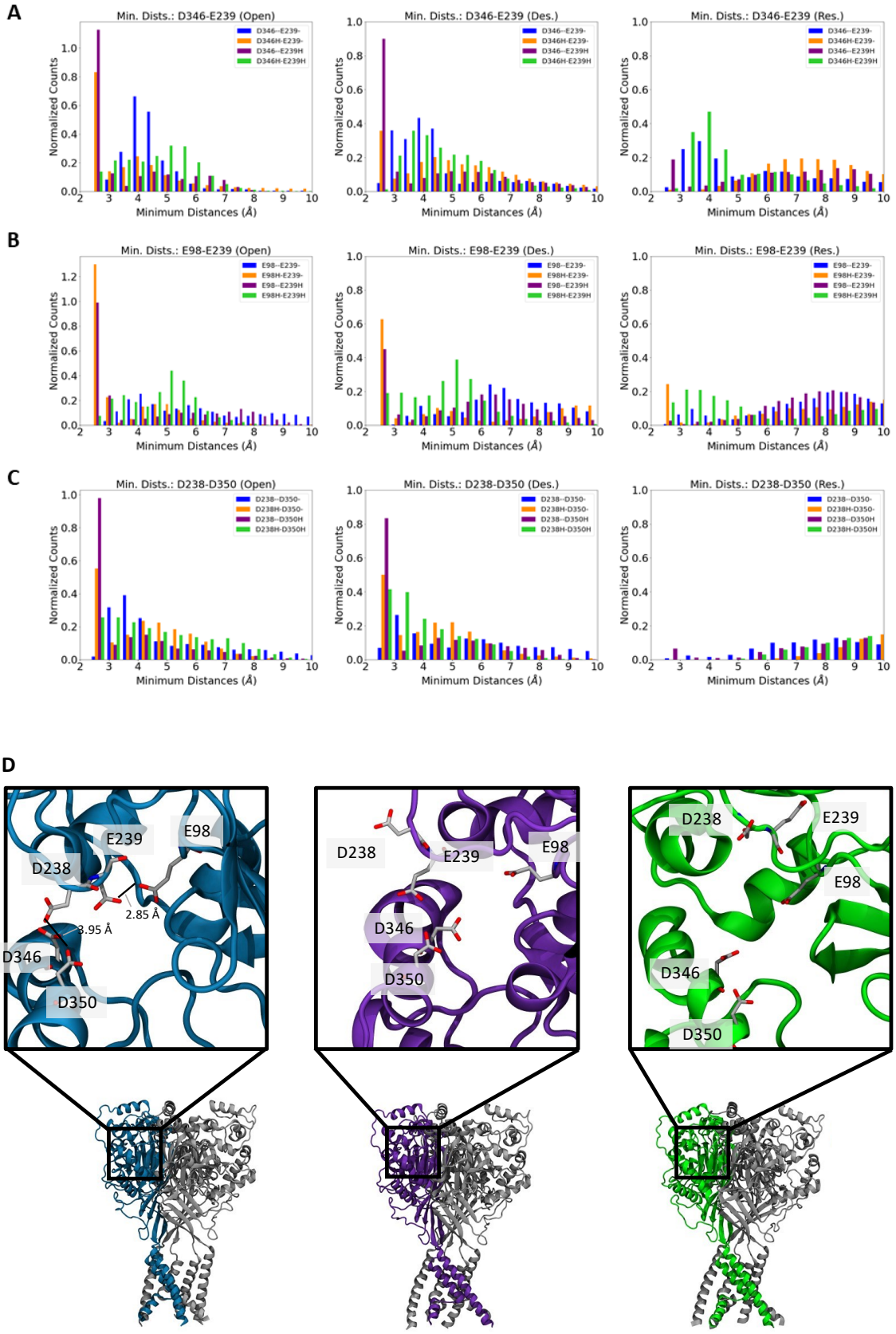
A
Min. Dists.: D346-E239 (Open)
Min. Dists.: D346-E239 (Des.)
Min. Dists.: D346-E239 (Res.)
D346--E239-
D346H-E239-
D346--E239H
D346H-E239H
Normalized Counts
Minimum Distances (Å)
B
Min. Dists.: E98-E239 (Open)
Min. Dists.: E98-E239 (Des.)
Min. Dists.: E98-E239 (Res.)
E98--E239-
E98H-E239-
E98--E239H
E98H-E239H
C
Min. Dists.: D238-D350 (Open)
Min. Dists.: D238-D350 (Des.)
Min. Dists.: D238-D350 (Res.)
D238--D350-
D238H-D350-
D238--D350H
D238H-D350H
D
E239
E98
D238
2.85 Å
3.95 Å
D346
D350

Figure 2.5 Approximation of the probability density functions of distances between acidic pocket interactions.
A) D346-E239, B) E98-E239 and C) D238-D350 for the open, desensitized, and resting states, from left to right. Legends indicate the changes in protonation states relative to the background protonation states from Table 2.1. Note that panel A and B, the leftmost plots, have a different y-axis. Interactions summarizing these trends are depicted in Figure 2.6. Counts over 10 Å exist but were not included in these plots. Note that probability densities can be greater than one as they are not probabilities. This is seen in the plots shown since the bin size used is small. It is the sum of the area under the curve that must equal to one as this is what represents the probability. D) Summary of interactions in the acidic pocket. Snapshots were taken from representative simulations of the open (left), desensitized (middle), and resting (right) state simulations. The top row represents snapshots of the ACP representing the interactions between the acidic residues E98, D238, E239, D346, and D350. The snapshots were taken at 18 ns, 12 ns and 18 ns, respectively, from left to right. Below are the full ASIC1 structures. The protonation states of each snapshot are specified in Appendix A Table 4.1. Donor-acceptor distances are drawn for residues with a distance of 4 Å or less. The systems depicted in panel D do not reflect the protonation states favouring all interactions suggested in this figure.

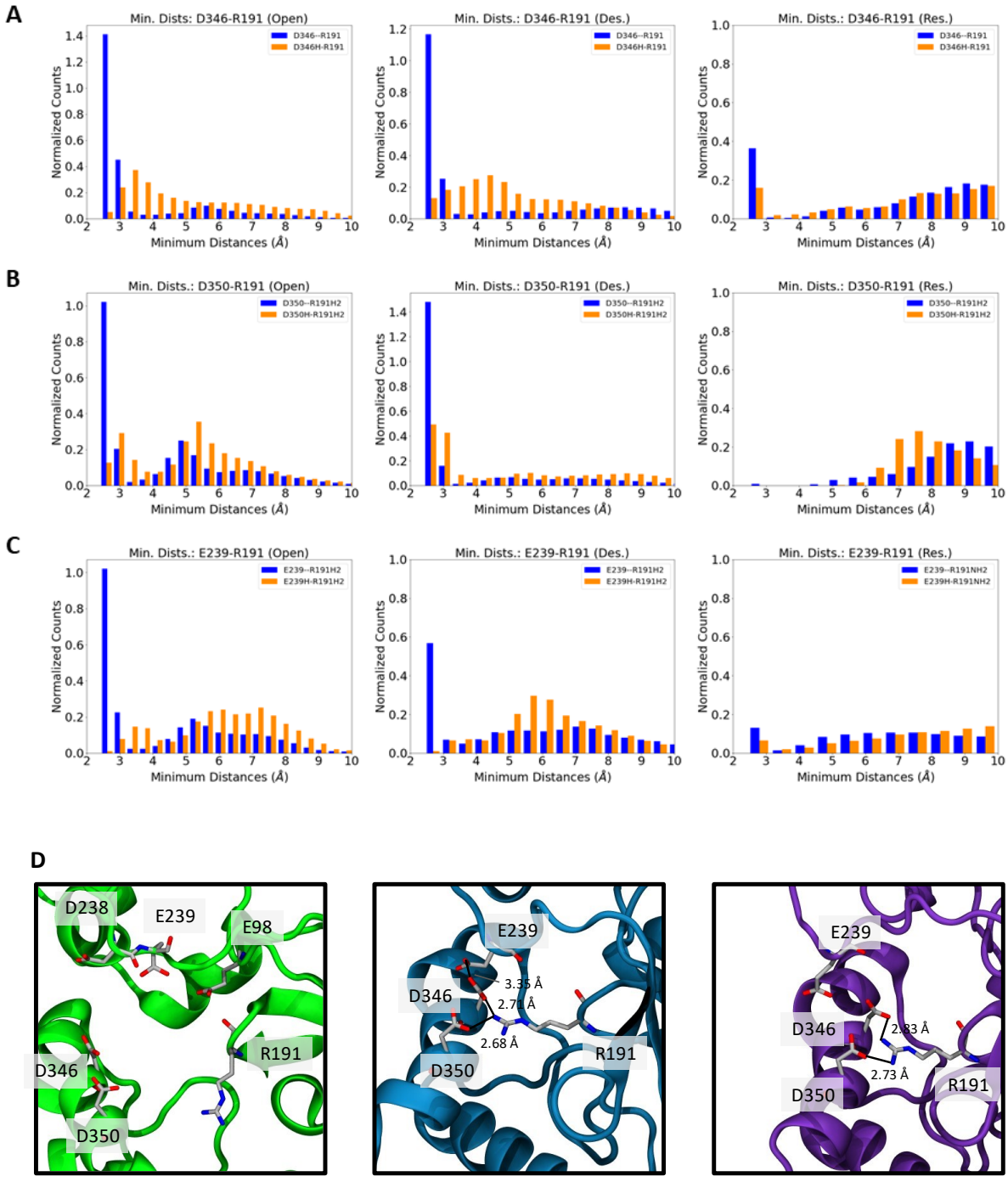

Figure 2.6 Approximation of the probability density function of distances between cationic and acidic residues.
A) D346-R191, B) D350-R191 and C) E239-R191 for the open, desensitized, and resting states, from left to right. Legends indicate the changes in protonation states relative to the background protonation states from Table 2.1. Counts over 10 Å exist but were not included in the plots. Note the different y-axis ranges. D) Snapshots were taken from representative simulations of the

open (left), desensitized (middle), and resting (right) state simulations. The enlarged snapshots of the ACP illustrates the interactions between the acidic residues R191, D238, E239, D346, and D350 as in Figure 2.5. The snapshots were taken at 18 ns, 10 ns and 18 ns, from left to right, respectively. The protonation states of each snapshot are specified in Appendix A Table 4.1. Donor-acceptor distances are drawn for residues with a distance of 4 Å or less. The systems depicted in panel D do not reflect the protonation states favouring all interactions suggested in this figure.

However, there is a low occupancy of E98/E239 donor-acceptor atom distances of less than 3.5 Å in the resting state with the E98H/E239- configuration. This may be interpreted as an initial approach of E239 to E98 in the resting state, a motion potentially required for activation of ASIC1. This interaction was also observed to form in one of the systems from section 2.1 above (the resting state with E98 and D408 protonated). In the case of the previous system, E98 was selected for protonation as it was thought to be a major proton-sensing residue due to its high, average pK_a values (~9-10 and ~8-9) in the low-pH states (open and desensitized) (Miaro, 2020). Thus, this observation supports that the protonation of E98 appears to be important for proton-sensing, perhaps being inclusive of the pinching motions observed in the ACP and proton-sensing in activation.

D238-D350 is another of the originally hypothesized carboxyl-carboxylate interactions (Jasti et al., 2007). When D238 is unprotonated and D350 is protonated (D238-/D350H), it yields the highest frequency of interactions in comparison to the three other possible protonation configurations (D238-/D350-, D238H/D350- and D238H/D350H). This is maintained in the desensitized state. However, no interactions exist between D238 and D350 in the resting state. The interaction most likely comes into place following local motions of the "crucial proton-sensors" and instead plays a role in stabilizing a "low-pH" structure, rather than being a driving force in the conformational changes involved in activation. It was reported in past studies of ASIC1a (mouse, rat and human constructs) that the mutation of these residues (D238, E239, D346 and D350) still yields pH-sensitive channels albeit with a reduction in their pH-sensitivity (Jasti et al., 2007; Krauson et al., 2013; MacLean & Jayaraman, 2017). Even with the mutation of 16 ionizable amino acid residues in the ACP, ASIC1 channels still retained function albeit the proton-sensitivity of these mutants was greatly reduced (Vullo et al., 2017).

In the ACP, there is also a positively charged arginine residue that appears to be flexible in our simulations. An interaction between D350 and R191 has been discussed in some detail in the literature where mutagenesis studies suggest that a disruption of this interaction using an R191A mutant shifts the pH_{50} of activation to lower values (H. Yang et al., 2009). This means that R191 appears to play a role in proton-sensing. In our open state simulations, D350 does participate in interactions with R191 in the first low-pH crystal structure and it was described to be a potential proton sensor site by Jasti et al. (Jasti et al., 2007). However, there are no indications in the resting state simulations that interactions between the R191-D350 pair appear at all (Figure 2.6 B).

As such, the R191-D350 interaction may not be important for immediate proton-sensing in activation, but instead in being an interaction that contributes to the stabilization of a low-pH state. In the open state, E239 and R191 form a salt bridge at a high frequency when E239 is unprotonated (Figure 2.6C). To note, these residues are relatively distanced from each other in the low-pH (open and desensitized) crystal structures. However, in simulations of especially the open state, the two residues approach each other.

There is a reduction of this hydrogen-bond distance occupancy in the desensitized state. Lastly, there is a small distribution of these interactions in the resting state which could indicate the start of the formation of the R191-E239 interaction in relation to an activation mechanism, as this interaction has a high occurrence in the open state simulations (Figure 2.6C).

Finally, D346 unprotonated interacts frequently with R191 (D346-/R191) in both the open and the desensitized states at a high frequency. This interaction also has a population of interactions existing in the resting states (Figure 2.6A), occurring at a higher frequency than any other hydrogen bond-like distance that we have measured with this analysis in the high-pH

(resting) state. The formation of this interaction in a resting conformation could potentially be important in transitions to the open state, where the interaction is even more favoured. To be clear, this interaction is not apparent in the crystal structure of the resting state (Yoder et al., 2018).

These results suggest that R191 is coordinating the charges of more than one acidic residue through salt-bridge interactions that can contribute interaction energies in stabilizing the open state. In the crystal structure of the resting state, R191 is adjacent to the loop with E98. The arginine side chain is positioned to interact with D260, E314, and H328 (Yoder et al., 2018), away from the acidic residues discussed above, in the lower end of the ACP (the other acidic residues occupy the upper end of the ACP that is also more exposed to solvent) (Figure 2.6D).

Through some mechanism, upon extracellular acidification, R191 no longer interacts with these three residues low in the ACP. The flexible side chain of R191 changes its orientation, making itself well-positioned to interact with E239, D346 and D350 in the open state (Figure 2.6D). Acidification of the ACP can potentially lead to the protonation of these charged residues (E314, D260, and H328 - becomes charged) which could make these interactions less favourable. Of these residues, E314 and H328 on average have pK_a values of or greater than ~5 calculated from unpublished results of open state simulations (Miaro, 2020).As such, the flexible side chain of R191 may be better able to dissociate from the lower end of the acidic pocket and explore conformational space in the upper ACP and form interactions with the previously described three acidic residues (D238, D346 and D350) on the thumb domain, opposite to R191 and the D238/E239 loop. This can possibly promote the collapse of the ACP.

Other interactions between D350-E354, R191-D238 and R191-E354 were also measured and overall, none of the interactions displayed any distances of high frequency within the accepted

range for hydrogen-bonding (< 3.5Å) defined above (Appendix A Figure 4.8). Thus, these interactions are not expected to form or to play any role in ACP collapse promoted-activation or proton-sensing in general. We have also used a similar approach to characterize the interactions and protonation states of three acidic residues in the palm domain of cASIC1 (Figure 2.7) (Rook, et al., 2021) covered in the following section.

2.5. A hydrogen-bond network in the palm domain retards recovery from desensitization

The final section of the Results highlights my contributions to the works described by Rook et al. (Rook, Miaro, et al., 2021). The mechanism of desensitization has supporting evidence that this transition can be characterized by a swap in the orientation of the side chains of L414 and N415 going from the open to the desensitized state. These two residues make up the β11-12 linker (Baconguis et al., 2014; Baconguis & Gouaux, 2012; Yoder et al., 2018). Previously, a study has reported a mechanism for the mediation of desensitization. It has been hypothesized that this distinct motion uncouples the ECD from the channel by acting as a molecular clutch (Yoder et al., 2018). Mutations and electrophysiological studies performed on this linker have also shown that this isomerization motion is required for desensitization where certain mutants that could lock the linker in the position of the resting state, were reported to prevent desensitization (Rook et al., 2020).

In a recent study, using electrophysiology, Wu et al. concluded that Q276 in human ASIC1a (Q277 in cASIC1 numbering) on the β9 strand acts as a valve regulating the isomerization of the

β11-12 linker. The idea is that Q276 with its side chain can sterically block the linker from flipping and they support this with a Q276G mutant that exhibits a sustained current following activation, in contrast to wild-type constructs that otherwise rapidly desensitize. The authors interpreted these results as an abolishment of desensitization, however, Q276W mutants from their studies with a larger and bulkier side chain than GLN displayed similar phenotypes to Q276G (Wu et al., 2019). This puts into question the validity of a steric mechanism as a Q276W should in theory lock the side chain in desensitization even more so than the wild-type. This is not the case. Additionally, a glycine (Q277G) mutant can also add more conformational flexibility to the β9 strand as it lacks a side chain. This may also affect the interpretation of their results.

We re-investigated these constructs with electrophysiology and instead showed that desensitization was not abolished in these constructs but instead, the channels desensitize rather quickly then activate again, resulting in what appeared to be a non-desensitizing current at low-pH. Ultimately, recovery from desensitization in the Q277G mutants was faster than wild type (Rook, Miaro, et al., 2021). To get a detailed understanding of the molecular mechanism behind these observations, we used MD simulations. First, in the crystal structure of the desensitized state (PDB ID 4NYK), the side chain of Q277 is positioned near the β11-12 linker and three acidic residues, E80, E412 and E417 (Figure 2.7A). Thus, there is the potential to form meaningful interactions in physiological conditions (in a membrane and solvated). To characterize potential interactions between these residues, hydrogen bond interactions were measured between the side chains of E80, Q277, E412, E417 and the backbone carbonyl of L414.

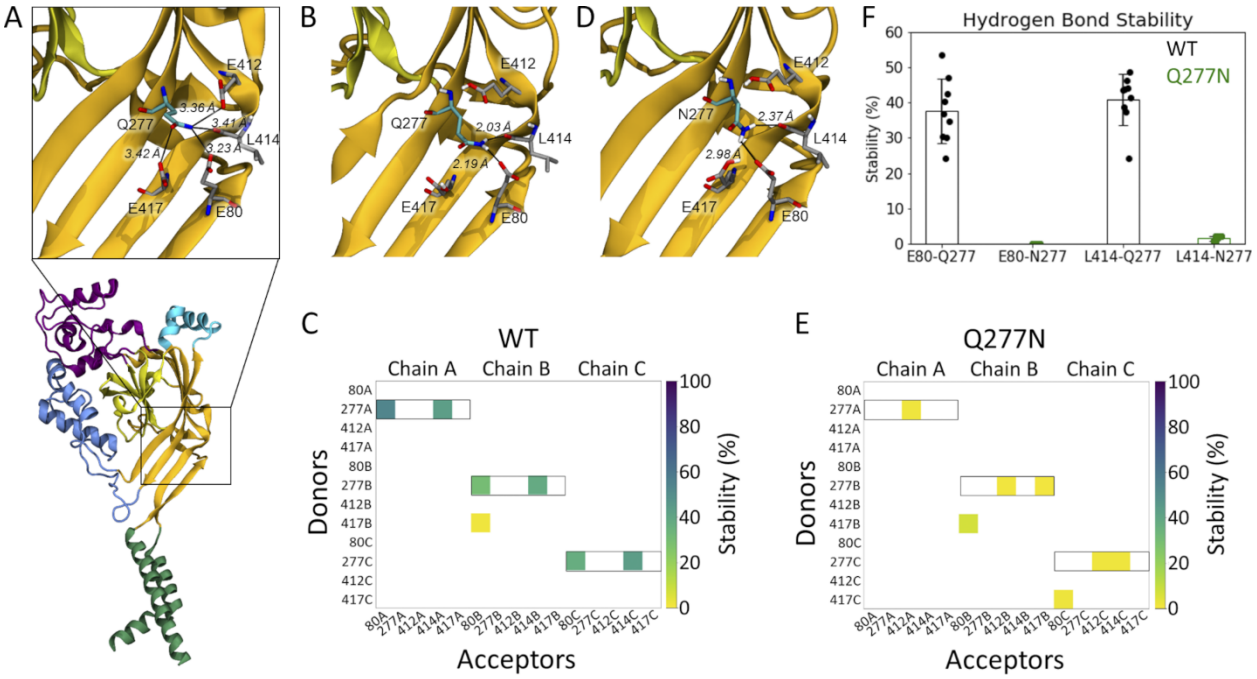

Figure 2.7 Q277 hydrogen bonds with E80 and L414 and a Q277N mutant weakens the hydrogen bond network. ©2021 ROOK et al. Originally published in JOURNAL OF GENERAL PHYSIOLOGY https://doi.org/10.1085/jgp.202012855.
A) Close-up of the palm domain in a single subunit of the desensitized state crystal structure (PDB 4NYK). Q277 is in proximity to E80, L414, E412 and E417. Distances between the acidic residues and Q277 are shown. B) Snapshot (taken at 8.6 ns) of a wild type simulation with interactions between Q277/E80- and Q277/L414O shown. C) Hydrogen bond analysis of a representative simulation of the wild type. Each square represents the frequency of an interaction as a whole of the simulation by colour according to the colour scale on the right-hand side of the plot. E80 is unprotonated and E412 and E417 are both protonated (E80-/E412H/E417H) in this simulation. All three chains are plotted individually. D) Snapshot (taken at 19.2 ns) of a Q277N mutant simulation with increased distances between Q277, E80 and L414 are drawn. E) Hydrogen bond analysis of a representative Q277N simulation. The plot is as described in C). The three acidic residues are protonated as in the wild type simulation. The hydrogen bond interaction seen in wild type is greatly weakened. F) Measure of the hydrogen bond stability as a percentage of the total simulation time for wild type versus Q277N. Q277N greatly reduces the frequency of the hydrogen bond network in the desensitized state.

These interactions were monitored for eight unique simulations where all possible combinations of protonation states of the three acidic residues (E80, E412 and E417) were sampled (Figure 2.8). We find that Q277 participates in the most stable interactions with E80 and the backbone carbonyl of L414 when E80 is unprotonated and E412 and E417 are both protonated.

We hypothesized that this hydrogen-bond network may be important in stabilizing the desensitized state and a disruption of these interactions would in turn de-stabilize this conformation and push the channel towards the resting state, hence the faster rates of recovery. As such, we suggested that a Q277N mutant would weaken the hydrogen-bond network due to its shorter side chain and thus should have faster rates of recovery from desensitization relative to the wild type. Simulations of Q277N displayed a reduction in interactions between 277N with E80, and L414O (Figure 2.7D, E, F) relative to wild type (Figure 2.7B, C, F).

N277 is a change by one -CH_2- group relative to the WT Q residue. We expect that the smaller size of this residue compared to its wild-type counterpart will negatively affect the observed hydrogen-bond network due to the distance between the donor and acceptor groups. We thus proposed that this residue (N277) would de-stabilize the desensitized state. Using electrophysiological recordings, we showed that Q277N recovers from desensitization at a rate 200-fold greater than wild type (it is 400-fold faster in Q277G) (Rook, Miaro, et al., 2021). Our hypothesis is thus supported experimentally and this refutes the idea that the stabilization and mediation of recovery from desensitization are mediated by Q277 acting as a steric block (Wu et al., 2019) but instead through electrostatic interactions contributed by Q277 (Rook, Miaro, et al., 2021).

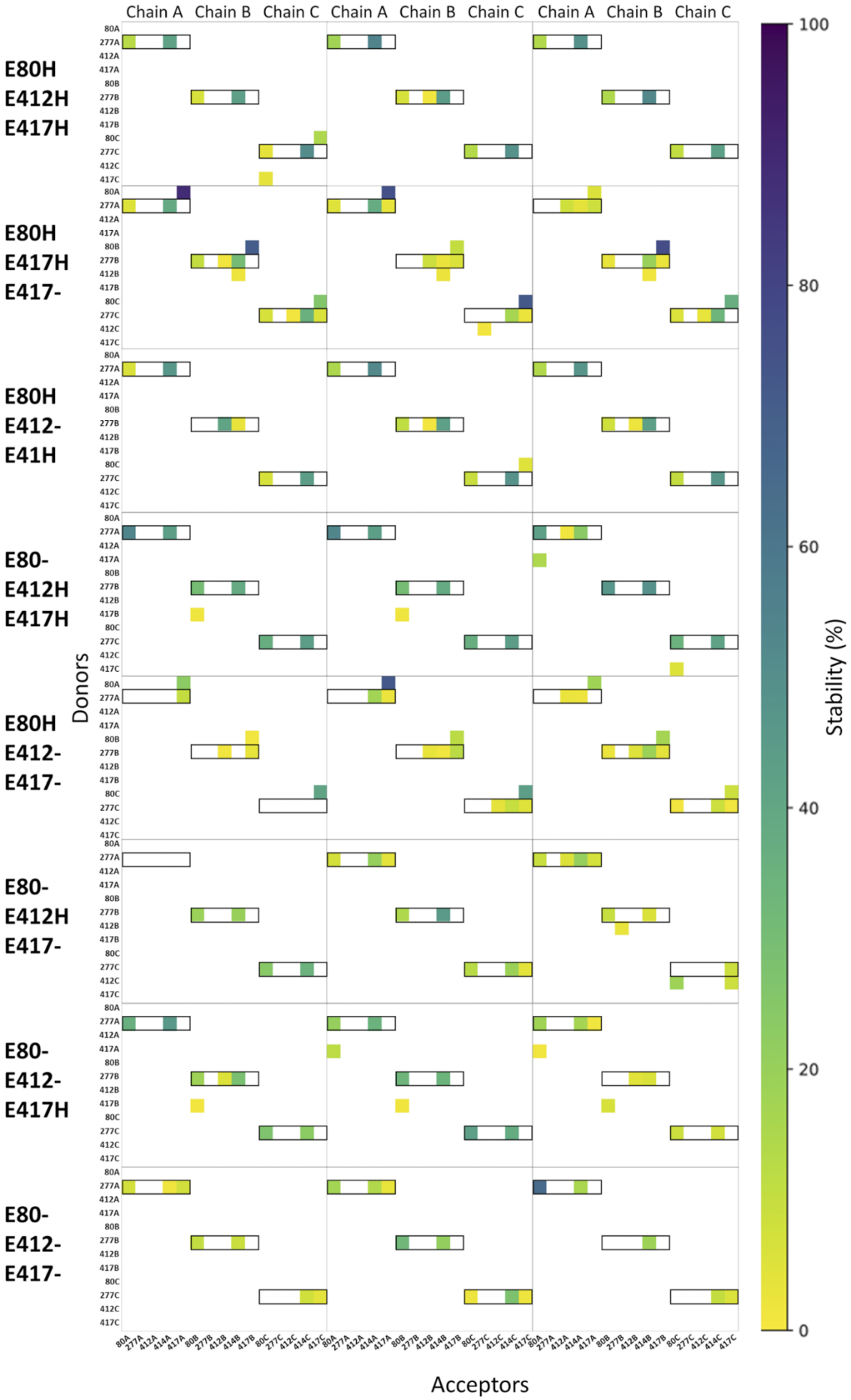
Chain A
Chain B
Chain C
E80H
E412H
E417H
E80H
E417H
E417-
E80H
E412-
E41H
E80-
E412H
E417H
E80H
E412-
E417-
E80-
E412H
E417-
E80-
E412-
E417H
E80-
E412-
E417-
Donors
Acceptors
Stability (%)
100
80
60
40
20
0

Figure 2.8 Hydrogen-bond network analysis of residues in the palm domain. ©2021 ROOK et al. Originally published in *JOURNAL OF GENERAL PHYSIOLOGY* https://doi.org/10.1085/jgp.202012855.
Hydrogen bond interactions were measured for each system in triplicate and each chain. Inter-chain interactions are also included. The frequency of hydrogen bond interactions over the length of a trajectory is plotted as a function of colour. All possible interactions between residues E80, Q277, E412 and E417 are calculated for every frame. The boxed results present the protonation scheme with the most stable interactions overall. Donors and acceptors represent the atoms from the specified residue that act as a donor or acceptor atoms to measure from. The percentage of hydrogen bond interactions is calculated individually and summed as shown on the plot.

Additionally, average pK_a calculations of E80 ($pK_a < 5$), E412 and E417 ($pK_a > 5$) from previous unpublished simulations (Miaro, 2020) would suggest the protonation scheme used for the wild type and mutant simulations in the desensitized state are appropriately assigned an, interestingly, this scheme contributes to the most stable hydrogen-bond network (Rook, Miaro, et al., 2021).

2.6. Discussion

The effects of protonation states on the dynamics of ASIC1 were examined to gain insights into the structure-function relationship with varying protonation states. Currently, it is not known specifically where protons must bind to induce conformational changes related to ion channel function. By testing various protonation states and monitoring the effects on the protein, we hoped to better understand and characterize potential proton-binding sites. It has been illustrated above that certain, presumably, "functional state-stabilizing" interactions exist in a single and specific protonation configuration. This is again with the assumption that changing the protonation states of ionizable residues near our interactions of interest will not affect the trends we observe. Of course, this is not true since by changing the protonation state of say an ASP by deprotonating it, this ASP residue becomes more electronegative. This can lead to a propensity of favourable interactions with neighbouring residues that are positively charged, or repulsive interactions with other nearby negatively charged residues. These effects can change the strength or disrupt nearby surrounding interactions. Nonetheless, our assumption was made as there are seven residues in the ACP that we look at. Taking into consideration each possible interaction, as

well as the proximity of other residues, in addition to considering the effects of changing the protonation states of nearby residues; the analysis becomes highly complex.

The favourable protonation state configurations shown to stabilize the resting, open and desensitized states seem to have direct implications to channel function as demonstrated with the hydrogen-bond network in the palm domain. There is an abundance of existing functional studies in the literature that aimed to characterize the function of ionizable residues throughout the ECD (ACP, palm, and wrist domains). These experiments consisted of a combination of mutagenesis and electrophysiological recordings, targeting mainly acidic and histidine residues in the ECD (Rook, Musgaard, et al., 2021), however, protonation states, or the molecular mechanisms by pH-dependent gating are not discussed as these methods lack information from a structural perspective. Here, we can directly observe the consequences of different proton-binding setups and relate them to the existing functional data to make inferences. The previously predicted protonation state configurations were not sufficient to sample the transition pathways for each functional state within the studied timeframe. Likewise, no indication of a full transition to the target states was observed for any system. This can be caused by at least two factors. First, the simulations in the range of nanoseconds are far from the relevant timescales of each transition pathway that are in the ms and s range (Gründer & Pusch, 2015; Hesselager et al., 2004). Nonetheless, there was an expectation to observe motions related to the beginning of a transition. Only in the recovery system was an expansion of the central vestibule like that of the target resting state observed. The second potential issue is that the protonation configuration predictions may be inaccurate, however, there is no way to verify this currently other than simulating for the relevant timescales which is a great computational cost for a protein of this size.

Constant-pH MD (CpHMD) simulations are a method that allows one to perform MD simulations at a constant pH. There are several approaches but essentially, unlike in classical MD, titratable residues can have their protonation states change during the simulation, dependent on a pH value of choice and the immediate surroundings of said residue (Aho et al., 2022; Baptista et al., 2002; Bürgi et al., 2002; J. Chen et al., 2008; W. Chen et al., 2014; Lee et al., 2004). This would be useful for seeing where protons tend to reside as a function of time at a physiologically relevant pH for any of the three functional states. Long time scale CpHMD experiments at target pH values can also allow for the sampling of physiologically relevant conformational changes. Current CpHMD methods, however, are more computationally intensive than classical MD as they tend to include extra steps to treat protonation or deprotonation events, often in different ways depending on the method used (Mongan & Case, 2005; Radak et al., 2017) and would of course require more computer time to run. Very recently, a CpHMD module has been released for GROMACS (Aho et al., 2022). The use of constant pH simulations in studying ASIC1 pH-dependent gating mechanisms is explored in-depth in the Discussion Chapter (Chapter 4). In the next chapter (Chapter 3), we use biased MD to overcome the sampling issue of classical MD and simulate the full transition pathways by applying an external force.

Despite the lack of transitions, we have been able to identify several interactions that are highly dependent on specific protonation states. Six major interactions in the ACP are characterized by having a high occupancy in some of the functional states. Clear differences exist between these interactions when comparing the resting, open and desensitized states (Figure 2.5, 2.6). These interactions are discussed here. First, the conformation of the two low-pH states (open and desensitized) have a highly similar ECD conformation (Figure 1.3), both

sharing a collapsed ACP. The decrease in interactions between E98-E239 and E239-R191 in the desensitized state, relative to the open state, was unexpected and may be relevant to desensitization. We speculate that a proton-transfer event is occurring between the interaction pairs – in our previous predictions, the difference in pK_a between E98 and E239 is less in the desensitized state compared to the open state (Miaro, 2020). This could mean at times, that E239 could potentially have an equal or even stronger hold on a proton shared with E98. It is unclear what is responsible for this difference between the open and desensitized states but considering our simulations, in the open state simulations E98 interacts consistently with E239 when E98 is protonated and E239 is unprotonated (E98H/E239-). A proton transfer from E98 to E239 would be consistent with E239 interacting with a deprotonated D346 at a high frequency in the open state (Figure 2.5). Contrarily, E239 still interacts with D346 at a high frequency when E239 is already protonated in the open state (D346/E239H). It is thus difficult to discern whether E239 is both protonated in the open and desensitized states, or if it may start off unprotonated then abstract a proton from E98 to strengthen its interactions with D346 on the thumb domain. These motions will be looked at in detail in the next chapter when the transition pathways are simulated.

Finally, the positively charged R191 has previously been described to participate in a D350-R191 interaction in the simulations of the open state in this chapter, as well as in the low-pH state crystal structures (Gonzales et al., 2009; Jasti et al., 2007). Here, R191 is shown to interact to nearly the same extent with D346 and E239 in both the open and desensitized states during MD simulations, and this underscores the importance of R191 in proton-sensing. R191A and R191E mutants were shown to decrease the binding affinity between the thumb and finger domains of ASIC1. The binding affinities were calculated using the molecular

mechanics/Poisson-Boltzmann surface area (MM-PBSA) method (H. Yang et al., 2009) on the low-pH cASIC1 structure (Jasti et al., 2007). In addition, the proton-sensitivity in electrophysiological experiments was reduced to a greater extent with the two arginine mutants (R191A, R191E) than with mutants of the other negatively charged residues in the ACP (D238A, D238K, D238N, D238S, E239Q, and D346N) (H. Yang et al., 2009) that are mainly thought of as potential proton-sensors. This is likely due to the positively charged guanidinium side chain of R191 coordinating simultaneous salt-bridge interactions with the three mentioned residues. The R191 side chain is typically positioned at the center of the ACP surrounded by negative charges in our simulations of the open and desensitized states (Figure 2.6D). Losing the positive charge would make the ACP even more electronegative and interfacing acidic residues on the thumb and finger domains would have a greater difficulty to approach each other in activation. However, the R191A and R191E channels retain their function, meaning that this proposed mechanism does not account for the entire pH-dependent activation mechanism. As discussed above and in the Introduction chapter, the ACP may not be the sole binding site behind the driving force for activation.

To speculate on the molecular mechanism for activation based on our observations, first in the crystal structure of the resting state, R191 starts with its side chain oriented downwards in the ACP (Figure 2.6D), away from the thumb and finger acidic residues (D238, E239, D346 and D350). Its guanidinium group is in contact with D260, E314 and H328. Upon extracellular acidification, for reasons not currently known, R191 dissociates from these interactions and can move along the ACP like a zipper (from the lower end to the top end, picking up electrostatic interactions with E350, D346 and E239 as it climbs along the thumb helix, knitting together the thumb and finger domains contributing to the “pinching” of the ACP into a collapsed

conformation. As R191 “slides” along, interfacing carboxyl-carboxylate (D346-D238, D350-E239) interactions are in more favourable positions to interact since they are brought closer together by the arginine. This may occur while a protonated E98 (adjacent to R191), interacting with E239, can lower the D238/E239 loop lower into the ACP to interact with D346 and D350 on the thumb domains. Of course, from looking only at simulations of a single conformation, we cannot see these mechanisms transpire. The relevance of this ACP mechanism, as in how these changes in motions are transmitted to the gate, will be further discussed in the following chapter (Chapter 3) and in the Discussion (Chapter 4) as we look to simulate the transition pathways of activation, desensitization and recovery which may, in turn, allow us to visualize a potentially relevant molecular mechanism. A cartoon representation of the potential mechanism for the pH-dependent gating is shown in the Discussion chapter taking into consideration the data discussed here as well as in Chapter 3.

The final experiment resulted in the characterization of a hydrogen-bond network in the palm domain of cASIC1 that appears to stabilize the desensitized state. This allowed us to associate the most stabilizing protonation states with E80 deprotonated and E412 and E417 both protonated. Despite this hydrogen bond being important in desensitization and recovery, the Q277N, and Q277G mutants still retain pH-dependence (Rook et al., 2021), thus, the described hydrogen-bond network does not appear to account solely for this pH-dependent mechanism. Other interactions in the wrist, palm or even the acidic pocket likely act in concert with the formation and breaking of the described network.

To conclude, the effect of protonation states on ASIC1 dynamics was explored in this chapter. We observed how by imposing previously predicted protonation states based on the pK_a predictions, simulation of a full transition pathway is not possible; likely due to time constraints

and uncertainty of having the correct protonation states. To further study the effect of protonation on channel dynamics in a more detailed manner, the protonation states of acidic residues were sampled in the ACP and in the palm domain to predict the most probable protonation states based on the most stable interactions that could form. We characterized E98 and D346 to have strong proton-sensor potential that can play a role in the early steps of activation, supported by existing functional studies. The importance of the basic R191 is also explored and suggested to play a more important role in acid-sensing in the ACP. In the next chapter, the full simulation pathways will be explored to better tie in protonation states to the gating mechanism of ASIC1s.

Chapter 3 : Simulation of Transition Pathways - Targeted Molecular Dynamics Simulations

3.1. Introductory Context

The recurring theme of this thesis involves the characterization of proton-sensors in ASICs and their implications for ion channel function. In Chapter 2, potential pH-dependent interactions presumed to play a role in the stabilization of each functional state were described. These descriptions come from the analysis of simulations of the individual functional states of ASIC1. However, we are interested in relating changes in protonation states with the ASIC1 gating mechanism. As such, analysis of the potential proton-sensors during the transition pathways of ASIC1 may provide a higher level of detail to this question.

For a pH-dependent protein, we assume that the protons also need to be placed on the correct ionizable residues for a conformational transition to occur. This protonation configuration is expected to change the energy landscape of a transition and make it more favourable to overcome the energetic barrier of a conformational change. Without understanding how the ion channel transitions from one state to another, triggered by a change in protonation states, it is difficult to identify what important residues are implicated in pH-dependent ASIC function.

Conventional MD, as used in Chapter 2, is practical for the sampling of the local conformational space of a starting structure. However, it is difficult to sample out-of-equilibrium states that could arise from rare events, such as conformational changes from a resting to an open state (Hollingsworth & Dror, 2018). This is due to current computational limits in terms of the ability to simulate on relevant timescales and insufficient conformational sampling. There exist methods to address the limited sampling of conventional MD as described in the Introduction. To this end, we use targeted MD, a non-equilibrium MD simulation method that will allow us to simulate potential transition pathways of activation, desensitization, and recovery in cASIC1. By

sampling the full transition pathways involved in ASIC1 function, we can also observe the effects of relevant conformational changes to the predicted pK_a values of ionizable amino acid residues of interest.

Targeted MD involves the introduction of a biasing force constraint to a system to speed up a process of interest, such as a conformational change. Targeted MD uses the RMSD between an input structure and a target structure as a reaction coordinate to pull the system towards the target with every time step (Grubmüller et al., 1996). This method implements a modified Hamiltonian, reminiscent of the "energy function" used in conventional MD, where H(X) represents the unmodified energy function (inclusive of the potential and kinetic energy) for all coordinates in a system (X).

$$H_\lambda(X,t) = H(X) + U_\lambda(X,t)$$

$$= H(X) + \frac{k(t)}{2}(s(X) - \lambda(t))^2$$

$$= H(X) + \frac{k(t)}{2}(s(X) - s_0 - vt)^2.$$

$U_\lambda(X,t)$ is the external modified potential energy function that is described as a harmonic potential spring with a dependence on time (t) and the collective variable (CV). In targeted MD, the CV is the RMSD (s(X)). The modified potential energy function includes a time-dependent biasing force constraint (k), and it is a function of the RMSD between the current and target atom coordinates. Here, k is the spring constant that defines how closely the center of the moving harmonic spring will be followed by the collective variable (CV) or RMSD. s(X) is the instantaneous measured RMSD. λ is the instantaneous target RMSD position at a given time point (t). s_0 is the user-defined target position of the CV, essentially the desired RMSD of the

targeted atoms relative to the target structure at the end of the simulation and v represents a constant pulling velocity (Bonomi et al., 2009; Grubmüller et al., 1996; Tribello et al., 2014). Although sampling of the full transition pathways is now possible, it should be noted that since we add restraints to the systems, we may lose information about potential intermediate structures that may exist in a complete, non-biased transition pathway.

Once more, the aim of this chapter is to characterize the likely proton-binding sites of cASIC1 as in Chapter 2, but instead by using targeted MD to simulate the transition pathways. Here the effects of targeted MD on global structural dynamics as well as on the pK_a of ionizable amino acid residues of interest are explored and related to their potential role in ASIC1 function.

3.2. Experimental Procedures

Simulation System Setup

All simulation systems were built and prepared as described in Chapter 2 (2.2 *Experimental Procedures – Preparation of the cASIC1 models p.26).* As outlined in Chapter 2, protonation states are fixed during MD simulations, wherefore each system was set up with two different protonation states, a "native" configuration, and a "target" configuration. For example, in the activation systems, we used a protonation configuration previously used to simulate a stable resting state as a "native" configuration. The "target" configuration was an open protonation state shown to stabilize the open state. This was imposed on the resting state structure when simulating activation. The protonation schemes are the same as used in the previous chapter (Table 2.1). For desensitization, two systems were prepared with either the open or desensitized stabilizing protonation states. Finally, for recovery, two systems were prepared with either the desensitized or resting state stabilizing protonation states (Table 3.1).

Targeted MD was implemented with a modified version of GROMACS 2020.1, patched with PLUMED *v2.7,* an open-source community-developed library (Bonomi et al., 2009; Tribello et al., 2014). A biasing force constraint is gradually applied, using the MOVINGRESTRAINT directive, to the backbone atoms (N, C_α, C, O) of the input structure. KAPPA, the biasing force constraint was set to reach its maximum, $5x10^5$ kJ/mol·nm^2, at 10 ns. The biasing force constraint was kept constant for another 40 ns. The target RMSD was set to 0.0 Å. Each system was simulated in triplicate.

Table 3.1 Summary of the transition pathways simulated.
All three transition pathways are simulated in triplicate with each of two protonation configurations: pre-determined "native" and "target" protonation states.

Transition Pathways	Input structure	Protonation State 1 (Native)	Protonation State 2 (Target)	Target Structure
Activation	Resting state (5wku)	Resting state	Open state	Open State (4ntw)
Desensitization	Open state (4ntw)	Open state	Desensitized state	Desensitized state (4nyk)
Recovery	Desensitized state (4nyk)	Desensitized state	Resting state	Resting state (5wku)

Measure of twisting in the TMD

To measure twisting of the TMD relative to the ECD, a pseudo-dihedral angle between two points representing the center-of-mass (COM) of the TMD and ECD, respectively, of the full trimer, as well as two points representing the COM of the TMD and ECD, respectively, of a single subunit was measured. The twist angles, exemplified in Figure 3.3B, are presented as averages for all three subunits.

pK_a Prediction

The pK_a of all ASP, GLU and HIS residues was predicted with PROPKA3.1 (Olsson et al., 2011). The pK_a shifts from the starting structure to the final structure were measured as the difference between the average pK_a in the first half-ns (0-0.5 ns, 10 frames sampled) and the last half-ns (49.5 – 50 ns, 10 frames sampled) of the simulations

$$pK_{a,shift} = pK_{a,avg(49.5-50ns)} - pK_{a,avg(0-0.5ns)} .$$

Snapshots from the simulations were taken every 0.05 ns to calculate the average pK_a within these two intervals, averaged for all subunits in all three repeats. Predicted pK_a values were also

measured from a snapshot every 0.5 ns during the full simulations to be plotted as a function of time.

3.3. Targeted MD transition pathways and the global structural dynamics of cASIC1

First, the force biasing constraint, target RMSD and pulling speed were tested to find a set of parameters that would allow us to get final simulation structures close to our target structures. The parameters used in the following simulations are described in the Experimental Procedures (3.2). The selected parameters were applied to all the simulation systems shown in this section. Each simulation targets the backbone atoms of the target structure. All side chain atoms can sample conformational space freely in the context of a changing backbone.

To monitor how well the final structure of the simulations agreed with the target structures, we first measured the C_α RMSD between the input and target structures. The parameters used led to a better agreement in the RMSDs between the input structures at the end of the simulation and the target structures, relative to the starting structures (Figure 3.1, Appendix B Figure 4.1). In activation, the thumb helices and both transmembrane helices displayed lower RMSDs in the final structure (50 ns), where these domains display the biggest differences in RMSD in the starting structure (0 ns).

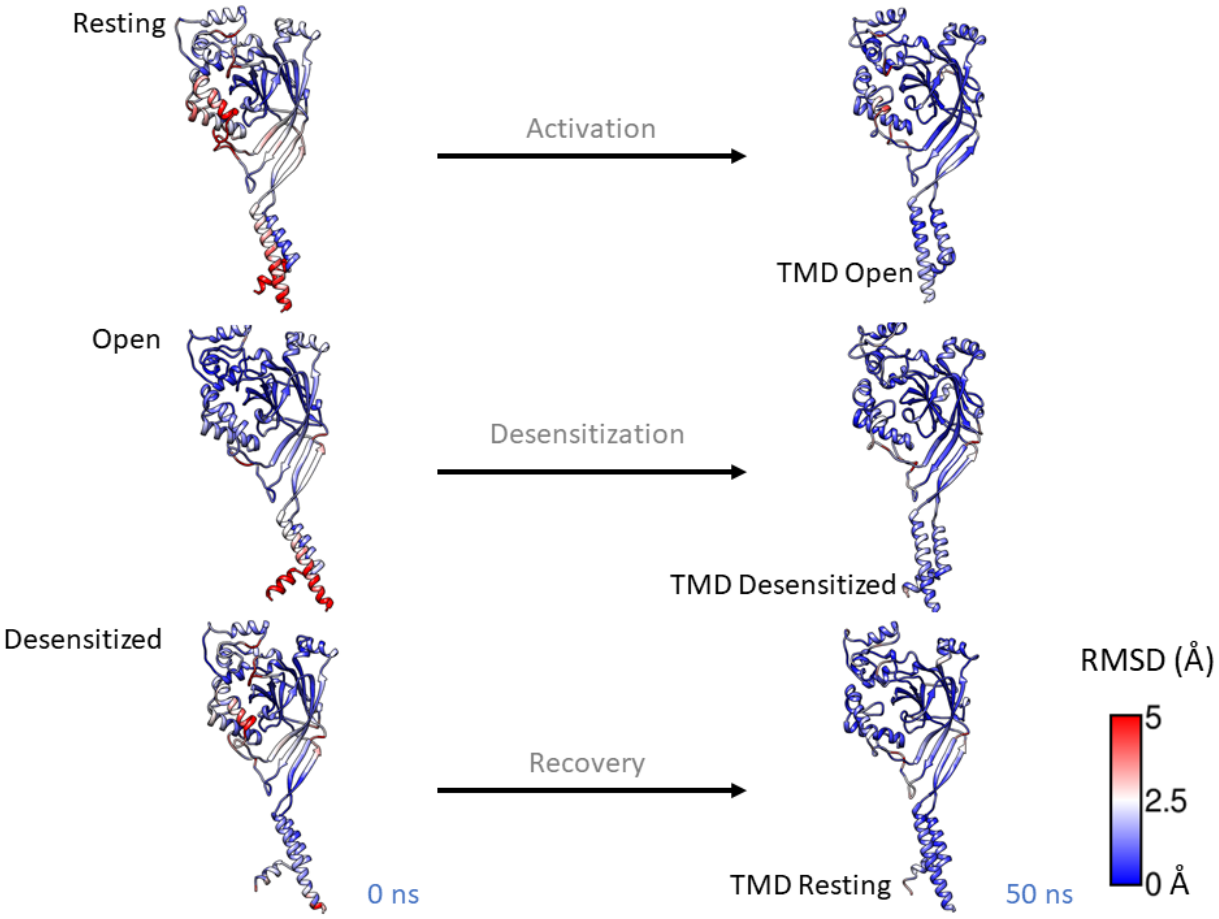

Figure 3.1 Global conformational changes.
Representative C_α RMSD values mapped onto single cASIC1 subunits. The RMSD measurements were taken for each transition pathway: activation, desensitization, and recovery, from top to bottom, respectively. The RMSD was taken between the starting structure of each simulation at 0 ns and again at 50 ns at the end of the simulation; both against that crystal structure of the target state. Top row: structures shown are the resting state system with the "native" protonation configuration at 0 and 50 ns with the open state crystal structure (4NTW) used as the target structure. Middle row: structures shown are the open state structure with the "native" (resting) protonation configuration at 0 and 50 ns with the desensitized state crystal structure (5WKU) used as the target structure. Bottom row: structures shown are the desensitized state structure with the "native" (open) protonation configuration at 0 and 50 ns with the resting state crystal structure (5WKU) used as the target structure.

Loops and unstructured regions in the acidic pocket tend to have higher final RMSDs compared to the structured regions, even at the end of all simulations. As these regions lack structural order, they are more flexible than structured regions that tend to show better agreement with their target structures. This flexibility could make it more difficult to agree with the crystal structure. This is not viewed as an issue per se, as loops are not expected to remain in a static configuration, as in the crystal structure, when embedded in a cellular membrane bilayer and solvated.

In all activation pathways, the TMD is slower than the ECD in reaching the target RMSD (Appendix B Figure 4.9). The $RMSD_{TMD}$ lags behind the other measured groups rapidly after the start of the simulation. As the biasing restraint continues to increase as a function of time, it is assumed that the system has a high enough force to overcome an energetic barrier in the conformational transition. The simulations suggest an initial resistance to conformational changes when in activation, the TMD is first seen to untwist. As the biasing force constraints increase as a function of time, the chains appear to be pulled apart. The timing of this motion is in line with the lagging $RMSD_{TMD}$ (Supplementary Movie 1 – 8 seconds in the movie, 12 ns in the simulation – the timing applies only to the activation systems with a resting protonation state). Interestingly, following initial untwisting, the pore already seems to be hydrated prior (Figure 3.2A) to it widening further (Appendix B Figure 4.10A).

In desensitization, the TMD is also the slowest group to reach its lowest RMSD but in a manner smoother than exhibited by the activation pathways (Appendix B Figure 4.9B). The recovery transition pathways with a native protonation configuration displayed a slight increasing RMSD in chain C for all repeats following an initial small decrease (Appendix B Figure 4.9C).

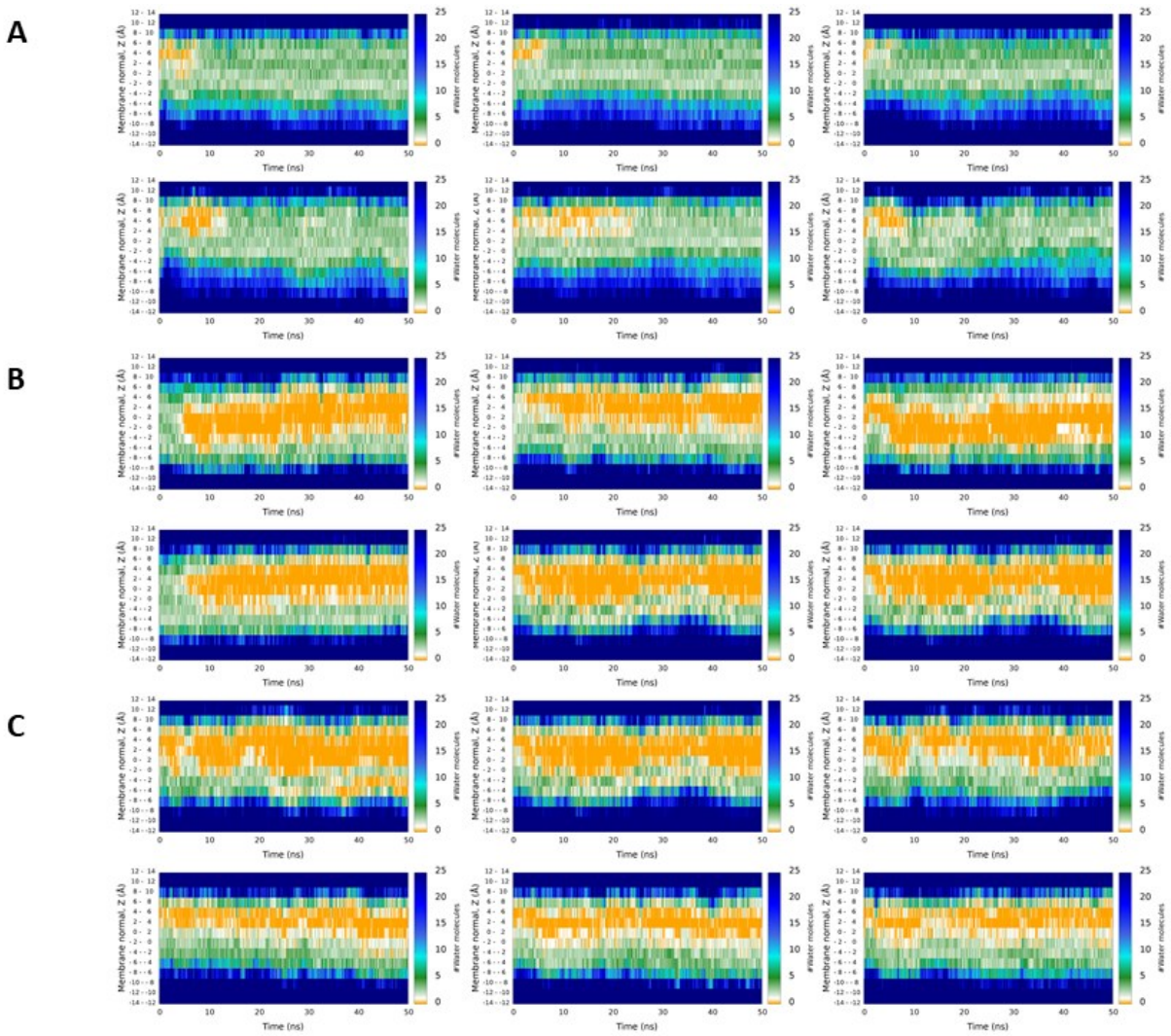

Figure 3.2 Pore hydration of all simulation systems.
Water molecules were counted along the pore axis (z) of each simulation as a function of time to monitor changes in the pore hydration for the A) activation pathways, B) the desensitization pathways and, C) the recovery pathways. The top rows and the bottom rows represent the "native" and the "target" protonation configurations for each panel, respectively.

Overall, the final RMSDs were lower than at the start, suggesting that our final conformation is close to the target.

To further ensure that our systems sample a transition to the target structures, we measured other indicators of a conformational change. One criterion measured was the hydration of the pore, as it is known that in activation the ion channel goes from being closed to open. As such, water is expected to fill the pore when it is opened. In desensitization, the ion channel through some unknown mechanism will close its gate, resulting in a dehydrated pore. Finally, in recovery, the gate stays closed, as such, it is expected for the pore to remain dehydrated throughout the transition pathway (Baconguis et al., 2014; Jasti et al., 2007; Yoder et al., 2018). Below, the pore hydration of each system is measured as a function of time (Figure 3.2). Interestingly, the activation systems with the "native" protonation configurations were quicker in terms of channel opening relative to the "target" protonation state, where two systems of the latter only open past the point where the maximum restraining force (10 ns) is reached (Figure 3.2A). In the desensitization systems, at the start of the simulations, the pore quickly dehydrates (Figure 3.2B). The protonation states may also influence the positioning and height of the gate.

With a resting protonation state applied to both the desensitization and recovery systems, meaning there are no protonated groups present in or around the TMD (D433 in the gate is either protonated or unprotonated in these systems), the gate appears to be smaller than when an open-like or desensitized-like protonation configuration is used on the two desensitized systems (Figure 3.2B, C). Perhaps the interactions that protonated D433 residues in the TMD introduces contribute to more gating along the pore. It may be that there are differences in the positions of the gate of the desensitized versus the resting state which is the case in other LGICs (Gielen & Corringer, 2018).

To monitor the progress of the transition further, a set of collective variables were chosen to represent a starting point and a final point in a reaction coordinate, describing the transition pathway. The selected reaction coordinates include descriptors for contraction and expansion of the acidic pocket in activation and recovery, respectively (Jasti et al., 2007; Yoder et al., 2018).

The C_α distances between D238 and D350 in the acidic pocket were measured to represent changes in the ACP (Figure 3.3A) (Baconguis et al., 2014; Jasti et al., 2007; Yoder et al., 2018). The second collective variable describes the twisting of the TMD relative to the ECD, a relevant motion during activation, where the TMD helices twist to open or close the channel in activation and in desensitization, respectively (Baconguis et al., 2014; Jasti et al., 2007; Yoder et al., 2018) (Figure 3.3B). The third collective variable represents the contraction and expansion of the central vestibule, suggested by the crystal structures to change during activation, desensitization, and recovery, respectively.

The resting state starts with an expanded central vestibule. During activation it contracts, and its volume shrinks even further into desensitization (Yoder et al., 2018). We measure this by calculating the average solvent-accessible surface area (SASA) of residues with side chains that face into the central vestibule (Figure 3.3C). First, considering the simulation of the activation pathways, with both protonation configurations, the measured SASA of the central vestibule appears to be noisy throughout the simulation. Meanwhile, the collapse of the ACP is seen to move along the reaction coordinate towards the distance of the open state crystal structure in both protonation configurations.

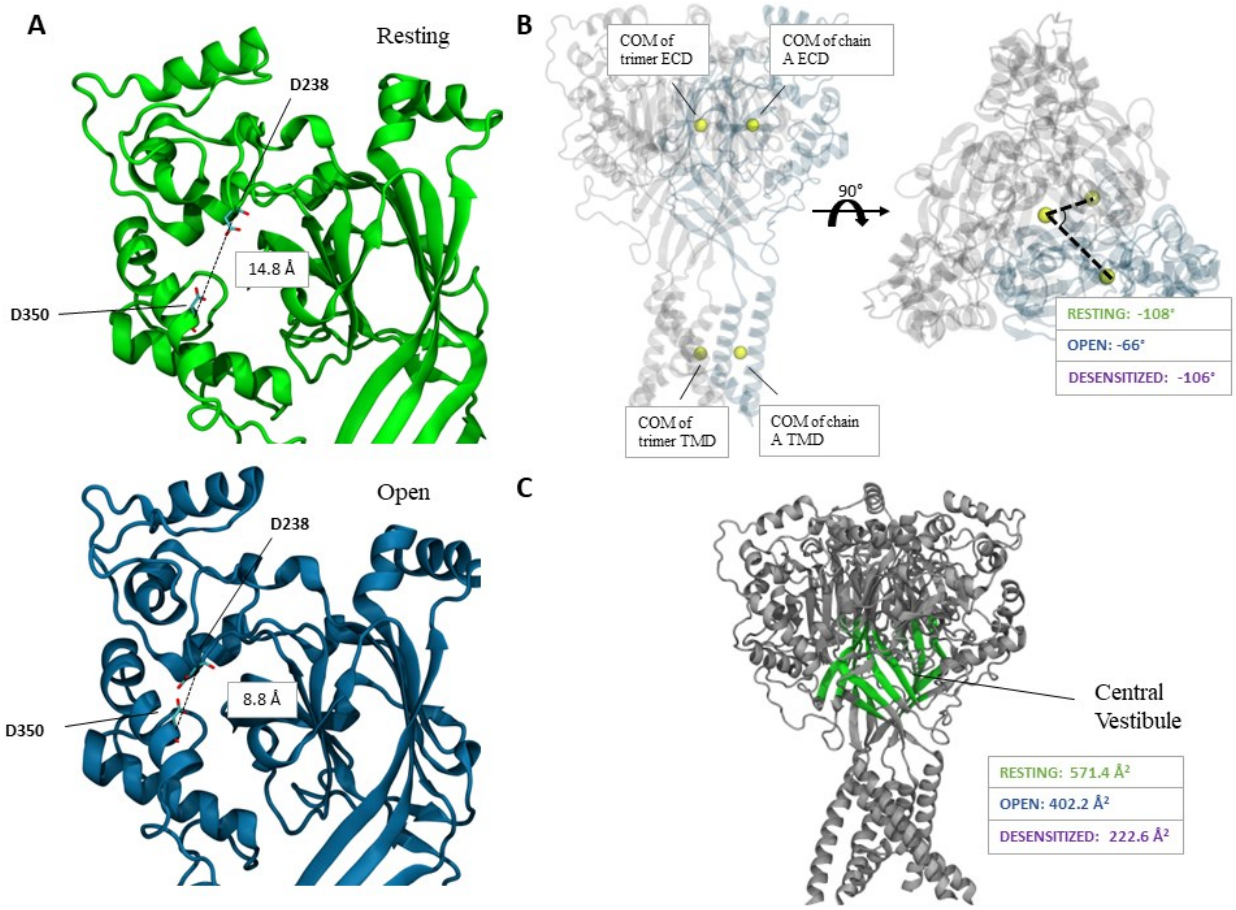

Figure 3.3 Collective variables used to describe the transition pathways.
A) The distance between the C_α atoms of D238 and D350 is used to represent the contraction and expansion of the acidic pocket in activation and recovery, respectively. The distances represent an average taken from all three subunits. The average D238-D350 C_α distance for the desensitized state (9.0 Å) is not shown. B) The twist angles represent the average pseudo-dihedral angles taken from the center of mass of the TMD and the ECD for both the trimer and for each subunit. The average angle for the crystal structure of each functional state is shown (Resting, 5WKU; open, 4NTW and desensitized; 4NYK). C) The regions of the palm domain with residues having their side chain pointing towards the central axis (central vestibule) are coloured in green. The contraction and expansion of the central vestibule are calculated as the sum of the SASA of all atoms with side chains facing the central vestibule for each chain.

Slightly counter-intuitive, however, the systems with the "native" resting protonation states approach the target distance consistently better than the "target" protonation states (Figure 3.4), with these systems also having overall lower final RMSDs (Appendix B Figure 4.9) and quicker channel opening times (Figure 3.2). A collapse of the ACP is apparent in the simulations (Figure 3.4A, Supplementary Movie 2) with not only acidic residues coming together, but a positively charged R191 also appears to participate in interactions in this region as the targeted open state is approached.

In the desensitization pathways, the TMD twists shut, and the acidic pocket remains collapsed as expected, in both protonation configurations (Figure 3.5). However, the SASA only appears to contract to the same level as the crystal structure in one repeat of the system with the "native" open state configuration.

The desensitized protonation is arguably worse at reaching a lower SASA with the measure even increasing briefly before reaching a lower SASA value (Figure 3.5C). In both activation and desensitization, there appear to be issues with reaching a lower SASA. Perhaps water molecules must be expelled from the central vestibule to ease the process of central vestibule collapse. Pulling residues by a biasing force constraint may not be strong enough to overcome the movement of water outside of the vestibule. Additionally, the crystal structure twist angles of the desensitized and resting states (-105.8° and -108.0°, respectively) are on average lower than those calculated from previous unbiased simulations of the desensitized and resting conformations (-94.1 ± 3.3° and -91.3 ± 3.2°, respectively) (Appendix B Figure 4.11). In the unbiased simulations, conformations can be sampled in a membrane and solvent environment.

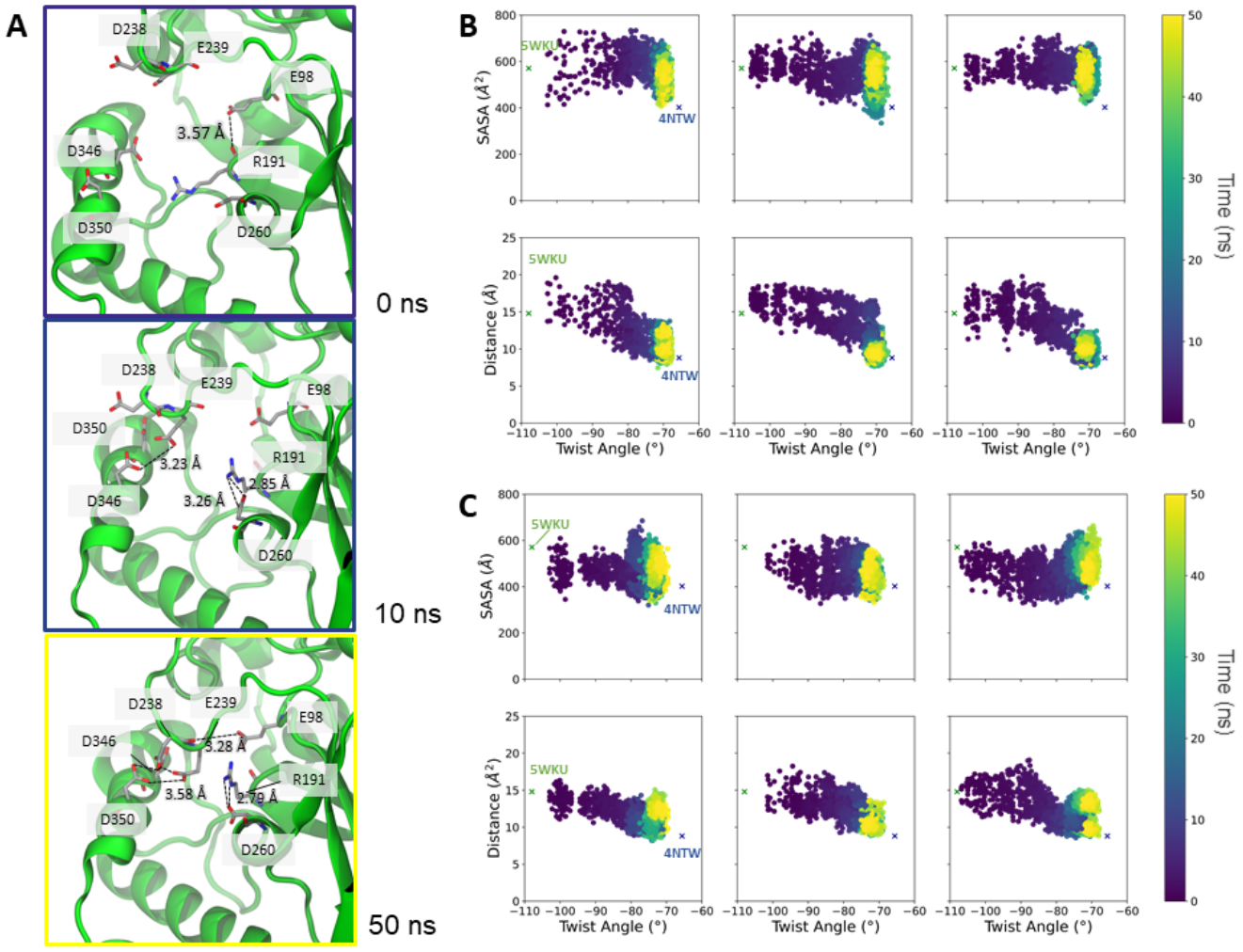

Figure 3.4 Activation transition pathways.
A) Snapshots of the acidic pocket of a representative activation transition pathway ("native" protonation configuration). B + C) The SASA and C_α D238-D350 distances were plotted as a function of the twist angle and coloured as a function of time for activation with the "native" and "target" protonation configurations, respectively. The crystal structure reference measurements for the resting state (green) and open state (blue) are drawn as X.

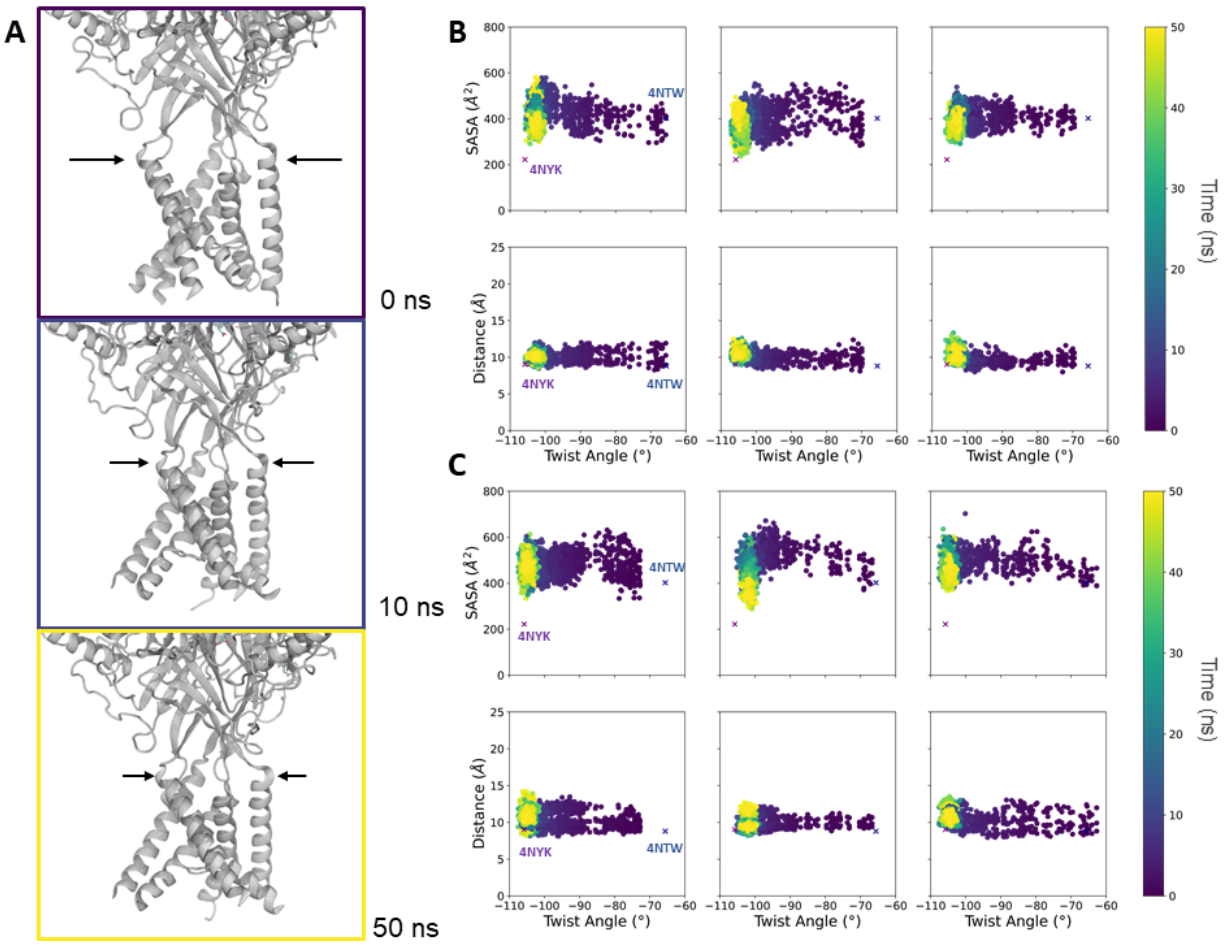

Figure 3.5 Desensitization transition pathways.
A) Snapshots of the TMD along the desensitization transition pathways at 0, 10 and 50 ns. B + C) The SASA and C_α D238-D350 distances are plotted as a function of the twist angle and coloured as a function of time for B) desensitization with the "native" and C) "target" protonation configurations. The crystal structure reference measurements for the open state (green) and desensitized state (blue) are drawn as X.

The targeted MD may be pulling the structure towards a conformation that is not relevant to a membrane-embedded cASIC1 in solvent, as is suggested by the tighter twist angles of the crystal structures.

Finally, in the recovery simulation systems, first, it appears that the crystal structure twist angles are not sampled well. This may again be due to the crystal structure conformations being irrelevant to a membrane embedded ASIC1 structure in solvent (Figure 3.6). The start of the simulation represents an equilibrated state of the crystal structure that went through several steps of relaxation during the minimization and equilibration steps.

In all systems emulating recovery from desensitization, the starting twist angle of the cASIC1 trimer is ~ -90°, i.e. the equilibration relaxes the twist angle from the initial -105.8 ° measured in the crystal structure of the desensitized state. Thus, as with our unbiased simulations, this suggests that a less twisted angle is more favoured between the ECD and the TMD in both the desensitized and the resting states. Additionally, the final twist angles in the recovery systems occupy the low -100°s, never reaching the target angle of the resting state crystal structure but surpassing that of the resting state unbiased twist angle (~ -94°), meaning that we may be targeting a non-physiological conformation by using the resting and desensitized state crystal structures as targets. As the TMD does not contain many acidic or histidine residues (only D433 in the gate), the residues that are usually considered to be proton-sensing candidates, we assume that the high twist angles of the resting and desensitized states will not greatly affect our observations related to proton-sensing in the ECD.

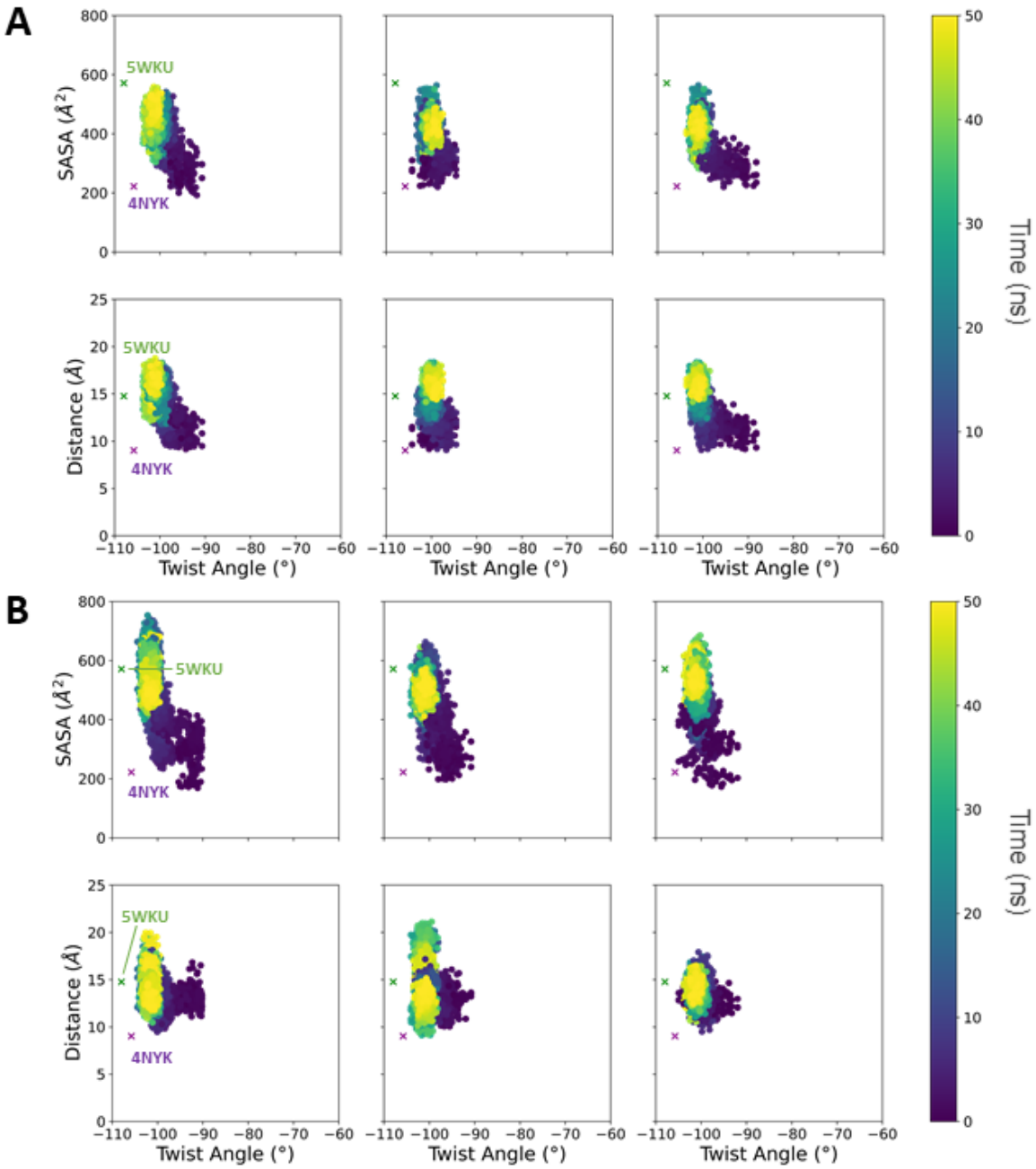

Figure 3.6 Recovery transition pathways.
Recovery with the A) the "native" and B) "target" protonation configurations. The crystal structure reference measurements for the desensitized state (green) and resting state (dark blue) are drawn as X.

Overall, the protonation states imposed affected how well the ion channel moves along the reaction coordinates and the extent of agreement with the target structure RMSDs with the final structures. Unexpectedly, in activation and desensitization, the systems with a "native" protonation state consistently had better agreement with their target structures than with their counterparts. We instead expected that when we impose a target protonation state on a system, the final structure would be in better agreement with the target structure as the protonation states may promote the formation of target-state interactions.

In recovery, the "target" or resting state protonation configuration displayed better agreement with the target SASA. The distances in the ACP were comparable between the two systems. The twist angles suggest the possibility of having simulated a transition pathway of the TMD that is unrealistic for a membrane-embedded trimer in solvent. Nonetheless, the SASA and ACP measurements, both residing in the ECD, appear to be in satisfactory agreement with the target structures. As such, we still expect to gain useful insights in the upcoming analyses. As the major conformational changes in the ECD, the region housing the putative proton-sensors, correspond with the target structures, we look closely at all acidic and histidine residues in these regions. We hope to characterize their potential function in the context of conformational transitions.

3.4. Conformational transitions and pK_a prediction of ASIC1

We follow our targeted MD simulations with an analysis of pK_a predictions for all ASP, GLU and HIS residues in the full trimer. We are interested in changes that may occur in the pK_a of these ionizable residues as a response to an imposed biasing force, or ultimately, conformational changes. As the pK_a is dependent on the local environment of an ionizable side chain, we do expect to see changes in the calculated pK_a value as a function of the reaction coordinates of the transition pathways. These differences may reflect changes in the protonation states that have the potential to be relevant in the ASIC1 gating mechanisms.

To this end, the average pK_a shifts ($pK_{a,shift}$) of the three amino acid residue types of interest were calculated for each system. The average shift in pK_a for all repeats and three subunits are shown in Appendix B Tables 4.2-4.7. Figure 3.7 displays the ionizable residues with a shift greater than a magnitude of one, to focus our analysis on residues that had the strongest response to the targeted MD. These amino acid residues are thought to change protonation states during the simulated transition pathways, and they can potentially be relevant to ASIC1 function. In activation, desensitization, and recovery, there are 17, 12 and 13 ionizable residues that fit the above criteria, respectively (Figure 3.7, Appendix B Figure 4.12). A few of these residues follow a shift of similar magnitude and in the same direction (an increase or decrease in the shifts) for a given transition pathway, disregarding the “native” or “target” protonation states imposed. This includes E98, E314, E412, E417 and D433. Meanwhile, other residues show a dependence on the imposed protonation states: E80, D238, D260, D346, D350, E374 and D408 (Figure 3.7).

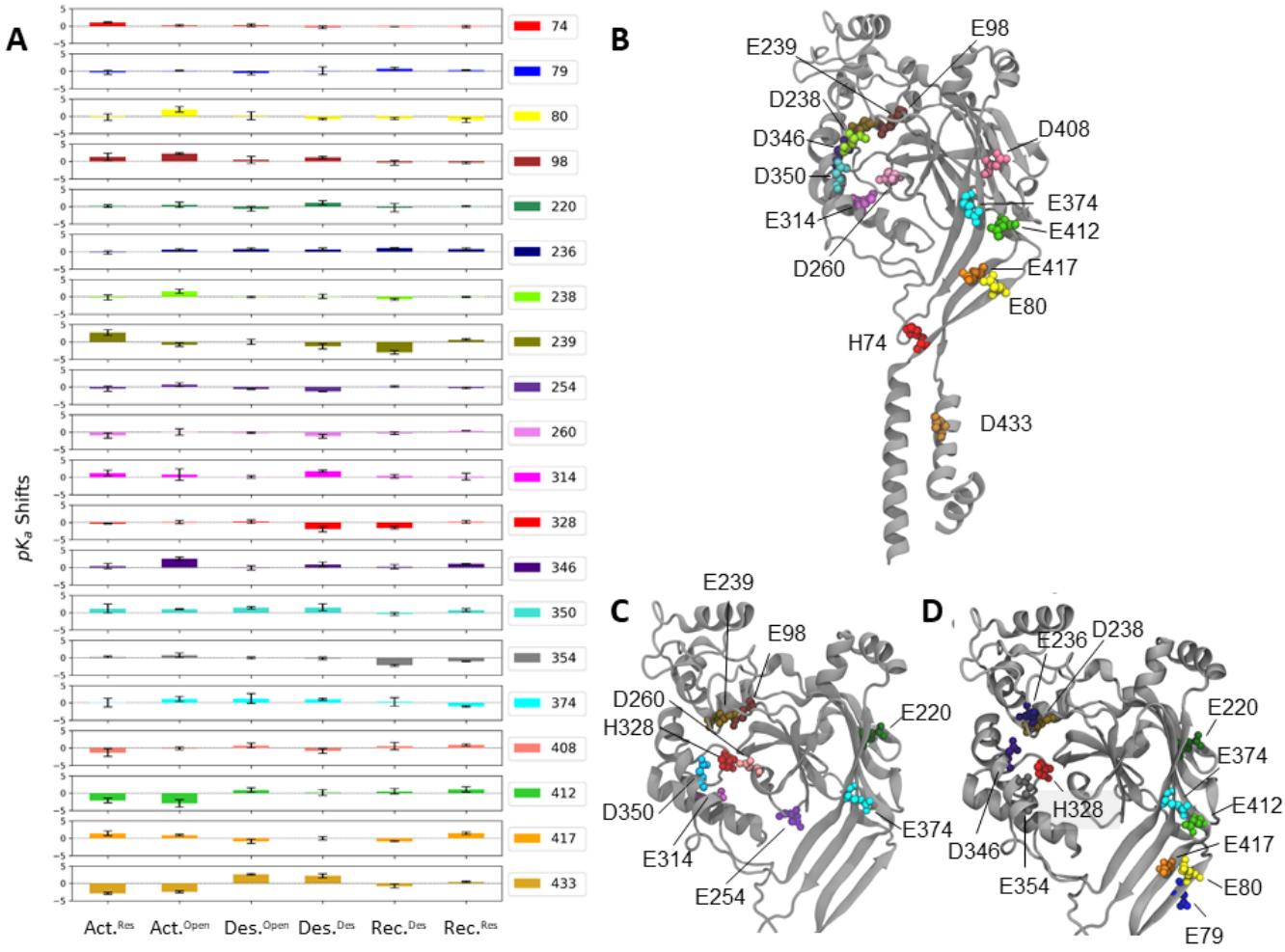

Figure 3.7 Average pK$_a$ shifts of ionizable residues.
A) The average pK$_a$ shifts of ionizable residues with a shift (pK$_{a,shift}$) greater than or equal to one, are shown. The average pK$_a$ shifts (pK$_{a,\ shift}$) were calculated for the triplicates of each of the six systems (Act.^{Res} – Activation with resting protonation, Act.^{Open} – activation with open protonation, Des.^{Open} – desensitization with open protonation, Des.^{Des} – desensitization with desensitized protonation, Rec.^{Des}, recovery with desensitized protonation and Rec.^{Res}, recovery with resting protonation). The standard deviations were calculated from the mean of the three repeats. B) Ionizable residues with a (pK$_{a,shift}$) ≥|1| in any of the activation, C) desensitization, or D) recovery simulations mapped onto the B) open, C) desensitized and, D) resting state crystal structures. The calculated pK$_a$ shifts for all ASP, GLU, and HIS residues in each simulation can be found in the Appendix (Appendix B Table 4.2-4.7).

We decided to look at the results of the systems that had a better agreement with the target structure, even if the protonation states may be "incorrect" (resting protonation for activation, open protonation for desensitization, and resting protonation for recovery). In the activation pathway with the "native" resting protonation configuration, of the five residues with the strongest effect on the pK_a as a response to the conformational changes, only E98, E314, and E417 displayed a clear increase over a threshold pK_a 5 (Figure 3.8). This threshold has been described in the previous chapters to represent an activating pH and thus a change in the pK_a from <5 to >5 suggests a potential protonation event for these residues. The second class of residues sometimes shows large changes in pK_a, but the results seem to depend on the protonation scheme. These residues include D350, H74 and E239, however, we only observe a change in the pK_a from <5 to >5 in the simulations with the "native" protonation configuration and not in that of the "target" protonation. This difference in pK_a shifts may be a result of having a different set of residues left unprotonated (singly protonated for the histidine) in the "native" configuration relative to the "target" protonation.

Thus, our results suggest that these three residues (H74, E239 and D350) are more sensitive to both their respective protonation states and the protonation of their surroundings, in contrast to the first group whose pK_a only appears to be strongly dependent on structural changes. In desensitization, again, residues meeting the above-mentioned criterion include D350, D433 and E374. For the second group: E254, D260, E98, E220, E239, E314, H328. Finally for recovery, residues meeting the first criteria include E354. The second group includes D79, E80, E220, E236, E239, E374, H328, E412 and E417.

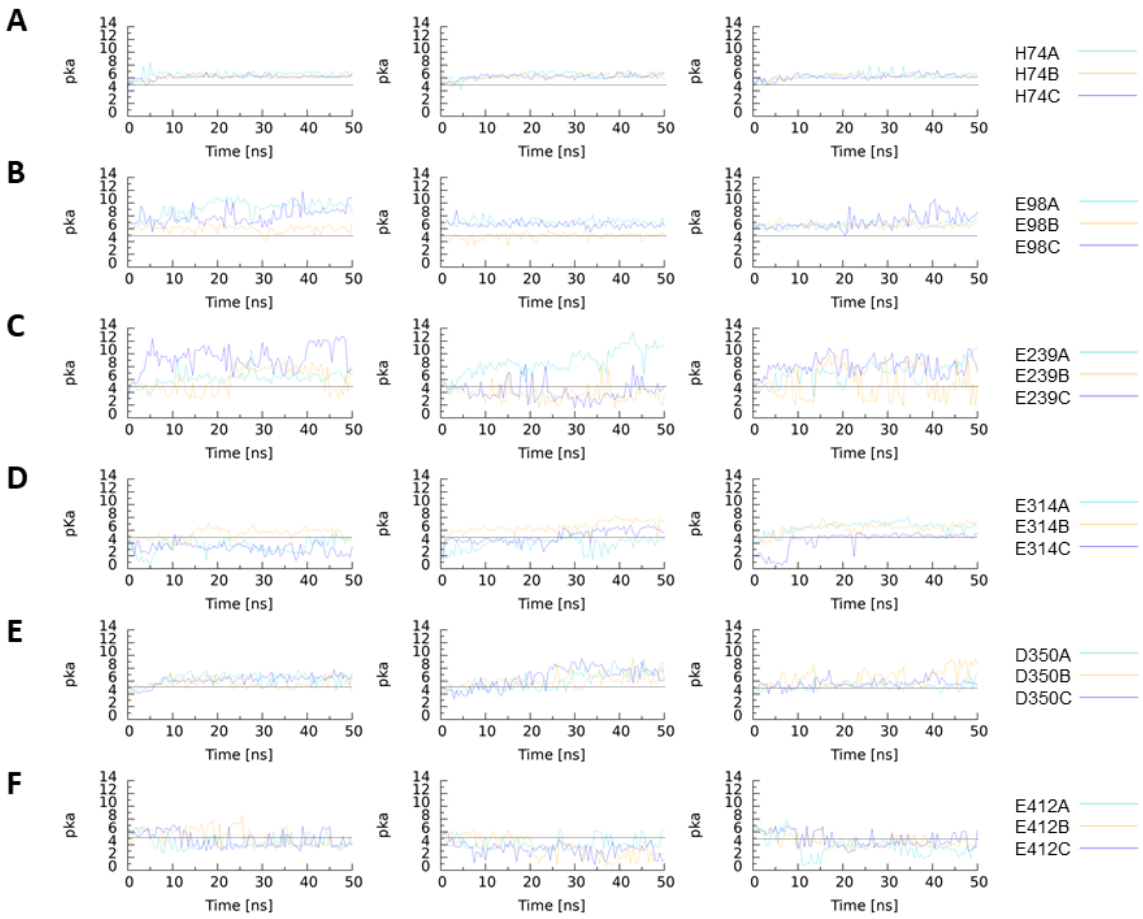

Figure 3.8 Ionizable side chains in activation with structurally dependent pK_a predictions. The ionizable residues including H74, E98, E239, E314, D350, and E412 display a strong response to changes in the conformation introduced by targeted MD. These residues are in the ACP (E98, E239, E314, D350), palm domain (E412) and the wrist domain (H74). A solid line at pK_a 5 marks a threshold pK_a for low pH or "activating" pH. pK_a values crossing this line are considered as potential protonation or deprotonation events (only residues with increasing pK_a trends are considered).

Next, we compared our observations of conformationally dependent pK_a shifts to existing mutagenesis studies that have perturbed these residues of interest. The strongest example is D433, where the pK_a shifts are in the same direction and magnitude for both protonation configurations in the activation and desensitization pathways. In desensitization, the pK_a values of D433 (< 5) at the start of the simulations would suggest that the side chains are unprotonated (Figure 3.9; bottom row). The simulation would suggest that the side chain is distanced from other residues and solvated resulting in a near table value pK_a. Progression along the reaction coordinate brings the aspartate (D433) closer to its negatively charged, adjacent counterparts on neighbouring subunits, likely raising its pK_a. When protonated, D433 can hydrogen bond with the carbonyl backbone of A428' of the adjacent subunit. This interaction contributes to a closed pore along with the formation of a salt bridge between R65-E426' (**Supplementary Movie 3**).

This observation is well supported by existing mutagenesis data where D433Q and D433N mutants, similar in charge to a protonated D433 and including a hydrogen bond donor, were reported to promote channel closure in lamprey ASIC1 (lASIC1) (T. Li et al., 2011), a constitutively open ion channel. This makes sense in the light of our simulations as this residue consistently shows a high pK_a in closed pore states, suggesting that it should be protonated. Thus, in D433Q and D433N where the side chain is constantly protonated, it will be easier to close the pore. A reduced proton-sensitivity was also reported in D434N mutants (D433 in cASIC1 numbering) in human ASIC1a (hASIC1a) (Yang & Palmer, 2014), suggesting that a lower pH is required to open the channel. This could be explained by the resting state being stabilized in the D434N mutant and hence requiring a stronger stimulus to open.

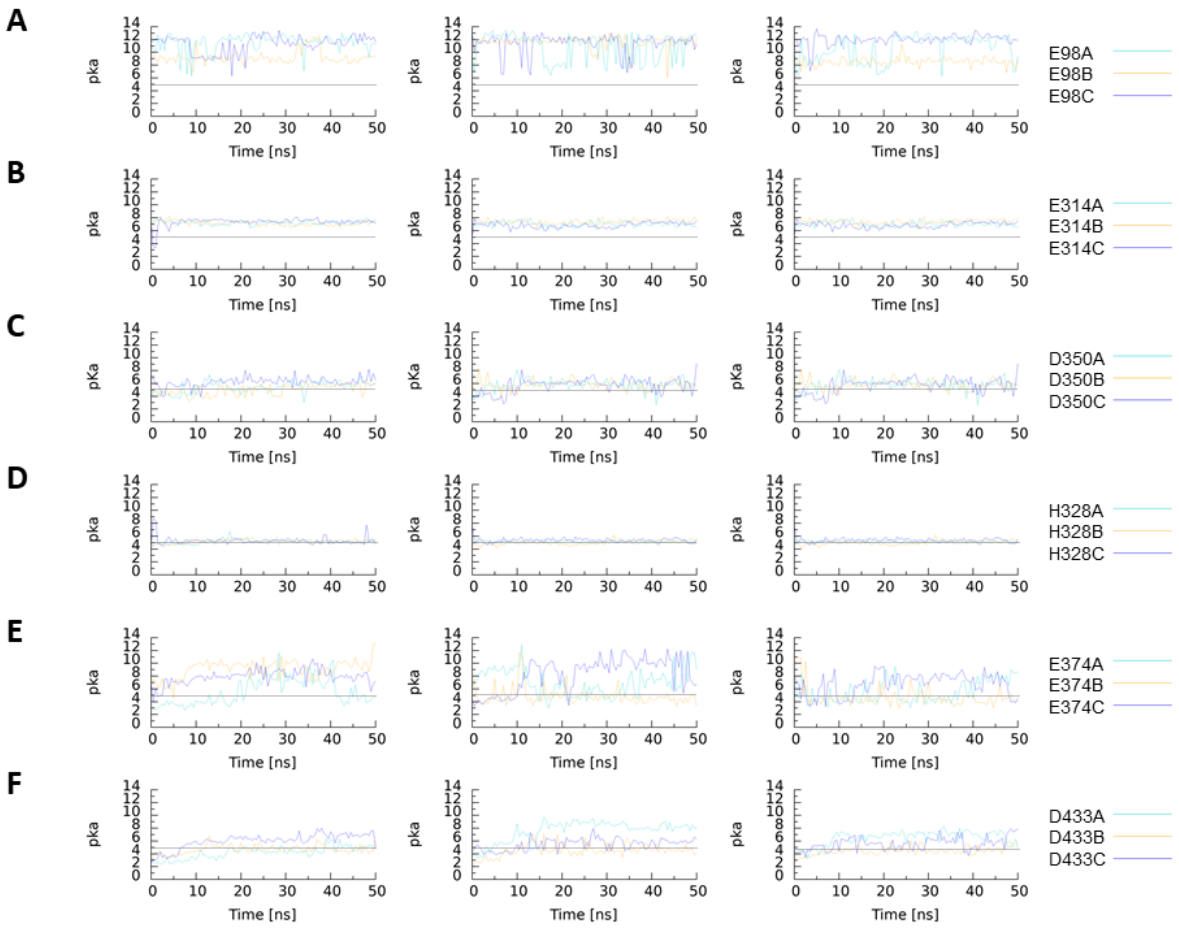

Figure 3.9 Ionizable side chains in desensitization with structurally dependent pK_a predictions.
The ionizable residues including E98, E314, D350, H328, E374 and D433 display a strong response to changes in the conformation introduced by biased MD. These residues are in the ACP (E98, E314, D350, H328), palm domain (E374) and the TMD (D433). A solid line at pK_a 5 marks a threshold pK_a for low pH or "activating" pH. pK_a values crossing this line are considered as potential protonation or deprotonation events (only residues with increasing pK_a trends are considered). Note: H328 is only exhibits a strong response to targeted MD in desensitization with the desensitized protonation configuration (not shown).

E98 is buried within the acidic pocket, which can contribute to its already higher than usual pK_a. From the structures, it is suggested that the ACP collapses upon activation and carboxyl-carboxylate interactions are formed (Jasti et al., 2007). In our simulations, the side chain of E98, when protonated, begins to interact with E239. This may aid the D238/E239 loop to approach the opposing thumb domain in the ACP, along with R191, and promote the collapse of the ACP. Further comparison of the simulation data with available functional data is covered in the discussion.

Finally, ASP, GLU and HIS residues behaved in one of three ways. 1) The residues listed above displayed a dependence on the application of the biasing force with no visible effect coming from the imposed protonation states of the systems. 2) Certain residues displayed differences between a pK_a with a dependence on the conformational transition if it was protonated versus if it was not. 3) Certain residues displayed no dependence on the conformational transition or changes in their protonation state. Essentially, the measured pK_a values of these residues did not change during the simulations. These residues are not thought to play any role in proton-sensing. The first two residue types are shown in Figure 3.10 below.

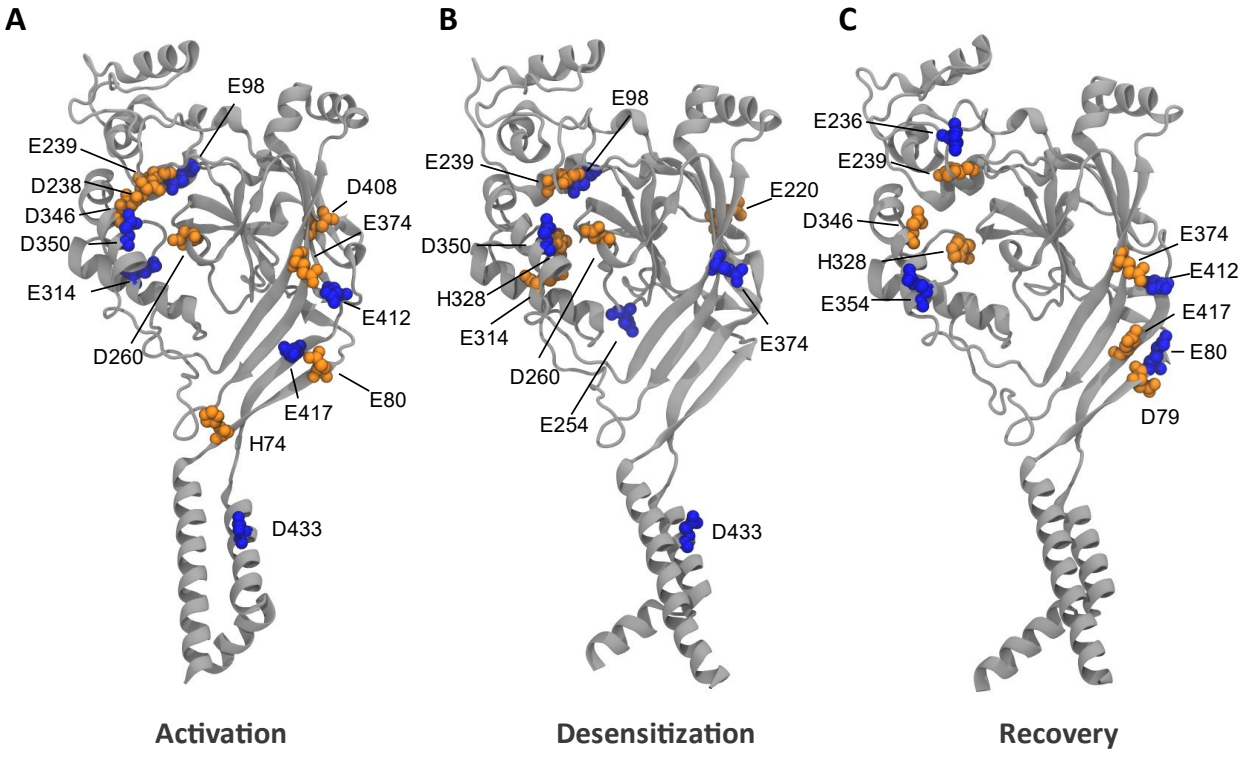

Figure 3.10 Potential proton-sensors of ASIC1.
The predicted proton-sensors are mapped onto a single ASIC1 subunit for activation, desensitization and recovery using a van der Waals representation. Residues in blue represent the type 1 behaviour. Residues in orange represent the type 2 behaviour.

3.5. Discussion

In this chapter, targeted MD was used to simulate the three major transition pathways of cASIC1. This was followed by a detailed analysis of the pK_a prediction of all ASP, GLU and HIS residues, the most probable candidates for proton-binding. Our analysis shed light on the different behaviours an ionizable residue can display. Here, the implications of the results and limitations of the methods implemented will be discussed.

As targeted MD uses the RMSD between an input structure and a target structure to pull the system to the desired configuration, our simulations reflect a direct motion of residues to their targeted positions. Small intermediate changes that can be described as more roundabout/indirect motions may be under-sampled. Even so, the results suggest that the end state is in satisfactory agreement with the target structures in terms of the ACP collapse or expansion in activation and recovery, respectively. The same is the case for the twisting of the TMD in the relevant pathways. Contraction of the central vestibule during activation and desensitization, however, did not reflect the target SASAs. This may be due to targeted MD not necessarily being a comprehensive method to simulate the twisting of the lower palm domain.

There is also the issue of water molecules that fill the central vestibule, and this may impact the ability to contract the central vestibule. This may affect the pK_a predictions of residues with side chains that face the central axis of this region (e.g. E80, E412, E417, E374). The predicted pK_a values can instead be expected to be higher than what was measured in the active states (open and desensitized) due to the increasing proximity of many negative charges from each subunit, with a lower count of water to stabilize the charges, due to a collapsed vestibule. The collapse of the vestibule would then favour the protonation and interaction

between the acidic residues in within it. Contrarily, a recovering ion channel readily exhibits an expansion of this cavity (Figure 3.6).

The crystal structures of the resting and desensitized states (Baconguis et al., 2014; Yoder et al., 2018) also have twist angles (-105.8° and -108°, respectively) that differ from those of our previous unbiased simulations (-94.1 ± 3.3° and -91.54 ± 3.2°, respectively) (Appendix B Figure 4.11). The crystal structures were solved by X-ray crystallography (Baconguis et al., 2014; Yoder et al., 2018) and the solvent in the simulation systems perhaps stabilize a less tense state as seen rapidly after the equilibration steps of our simulations. It is possible that an irrelevant TMD conformation was thus targeted in both recovery and desensitization.

Another interesting observation is that in the activation pathways, two steps in ion channel opening can be distinguished. First, the ion channel untwists where the channel becomes well hydrated, suggesting that the pore is open. Following this first opening (untwisting from the tighter twist angles of the resting state, the pore becomes hydrated), the ion channel can be seen to expand even further, yielding a more open pore. Curiously, multiple open state conformations were reported for constructs expressed at two different proton concentrations (**Supplementary movie 1**, Appendix B Figure 4.9A and 4.10).

The high-pH MitTx (Texas coral snake toxin) toxin-bound structure of an open state (pH 7.25) had a wider constriction at the level of D433 in the permeation pathway and it did not exhibit sodium selectivity, as opposed to the low-pH toxin-bound (pH 5.5) construct with a smaller pore radius (Baconguis & Gouaux, 2012). However, there have been no reports of a multi-step activation mechanism regarding the ion channel pore and the functional relevance of the very open pore is unknown.

pK_a prediction of the ionizable residues of interest led to the distinction of three different pK_a related behaviours, as mentioned above. Further investigation is required to propose a difference between the first two groups in terms of their function in the pH-dependent gating mechanisms of ASIC1. One could speculate that residues of the first category, with a pK_a dependent on conformational changes, are proton-sensors which stabilize the target state and are thus important for function. The second group shows high variability, and these residues display a conformation-dependent pK_a shift only when protonated. These are also considered to be potential proton-sensors that help to drive a conformational change. What makes them different from the first group may be related to their relative mobility or a better ability for their side chains to sample conformational space and thus form favourable interactions that were not possible without an extra proton (i.e. hydrogen bond interactions with other polar side chains). However, further inquiries would be required to propose any significant difference between the two groups in terms of their relevance in cASIC1 function.

Finally, six amino acid residues are suggested to be the most affected by targeted MD for both the activation (H74, E98, E239, E314, D350, E412) and the desensitization (E98, E314, H328, D350, E374 and D433) pathways (Figure 3.8 and 3.9). Our observations are highlighted in the context of existing mutagenesis studies beginning with activation. H74 sits on the outside of the lower palm domain. Our simulations suggest that H74 would become doubly protonated in activation, making it positively charged. This opens the opportunity for the side chain to form an extra hydrogen bond or form charged interactions with nearby residues. H74N in previous studies, evoked no pH-dependent responses in mutant rASIC1 and hASIC1a, constructs. It is however not known whether this phenotype is a consequence of a change in the structure (Lynagh et al., 2018; Paukert et al., 2008).

Acidic pocket residues, such as E239 and D350, when mutated to Q and N in rASIC1a and mASIC1a exhibited functional ion channels that were less proton-sensitive (Krauson et al., 2013; MacLean & Jayaraman, 2017; Paukert et al., 2008). This means that it takes a higher proton concentration to evoke a maximal response in the mutants that is similar to wild-type constructs. E417Q in the palm domain in rat ASIC1a and E418Q in human ASIC1a also lower the proton-sensitivity (Krauson et al., 2013; Liechti et al., 2010; MacLean & Jayaraman, 2017; Paukert et al., 2008). E417 must play a role in forming relevant interactions that are important in activation upon its protonation. These interactions may be relevant in the contraction of the palm domain. E417 mutants may limit the ability of the ion channel to open upon extracellular acidification.

There are limited studies on the function of E98 and E314. E98 is on a buried loop that links the finger domain to the β-ball domain. Our simulations suggest that E98 in activation, when protonated can participate in hydrogen bond interactions with E239 on the D238/E239 loop and along with the adjacent R191 and guide the loop closer to the interfacing acidic residues on the thumb domain (D346 and D350). E97 (E98 in cASIC1 numbering) is not conserved amongst other ASIC subunits, particularly the less pH-sensitive ASIC1b and ASIC2a subtypes. An E97A mutant in mASIC1a was reported to have a reduction in the peak maximal response relative to WT (Chu et al., 2004). One study reports reduced proton sensitivity in mutants of 8+ residues including E97 in hASIC1a constructs (E98 in cASIC1 numbering) meaning that the constructs retain a pH-dependent function without a protonatable E98 side chain, even when many other ACP residues have been mutated (Vullo et al., 2017). E98 may well play an allosteric role in pH-sensing but is not a main driving force for activation.

E314 is located in the center of the lower helix in the thumb domain and contributes to a chloride binding site along with R310 and K212' from the adjacent subunit in the open and desensitized state crystal structures (Baconguis et al., 2014; Gonzales et al., 2009; Jasti et al., 2007). Generally, our simulations exhibit an E314 with a side chain that does not appear to change its conformation between the resting, open and desensitized states. In the resting state, the acidic side chain is well-positioned to participate in electrostatic interactions with R191, which points downwards in the ACP.

R191 also interacts with H328 and D260 as mentioned in Chapter 2. During activation, the flexible side chain of R191 changes from pointing downwards to upwards in the ACP, breaking its interactions with E314 and D260 and instead, forming interactions with the D238/E239 loop and sometimes the incoming thumb helix on the opposite end of the ACP. Incidentally, R191 does not always have a drastic conformational change in activation. This motion was seen five times out of nine with the resting protonation state imposed on the resting state. However, with the open protonation state, this motion was instead observed eight of nine times. Coincidentally, whenever R191 breaks interactions with E314, the glutamate residue surpasses the threshold pK_a 5 in activation (Figure 3.8). This increase in the pK_a coincides with the loss of a favourable interaction, and so protonation of E314 at low pH would be favoured. Following this motion and the approaching of the thumb domain, R310 and K212' become better positioned to form the Cl^- binding site with E314. Three individual mutants of these three residues in mouse ASIC1a (mASIC1a numbering; K211A, R309A and E313A) resulted in faster rates of desensitization, but no changes in activation kinetics (Kusama et al., 2010).

Next, desensitization is investigated and continuing with E314, a change in the rates of desensitization would suggest that the Cl^- binding site eliminates chloride modulation while also

reducing the rate of tachyphylaxis (a gradual decrease in drug response following repetitive administration), (Kusama et al., 2010). D350 in the ACP again appears to be relevant in desensitization. H328A was reported to decrease the pH_{50} values of activation (H. Yang et al., 2009) but there is little knowledge about its potential implication in desensitization. It was suggested to mediate interactions between the finger and the thumb subdomains, which can facilitate collective motions between the two subdomains. These motions are suggested to be important for proton-dependent gating (H. Yang et al., 2009). There are no indications that H328 undergoes any drastic changes. In the resting state, as mentioned above, R191 is well-positioned to interact with H328 (Yoder et al., 2018). This interaction is usually broken during our simulations of activation. H328 does not appear to interact with any other nearby residue nor does the side chain change its positioning in the activation pathway with the resting protonation state.

Strangely, although not related to desensitization, in the simulations of activation with the open protonation state, the H328 residue can be seen to flip from inside of the ACP to outside of the region with its side chain becoming completely solvent-exposed. This may be a result of doubly protonating the histidine residue and we do not believe that this conformational rearrangement is relevant (**Supplementary Movie 4**). This flipped H328 conformation is not suggested in any of the existing crystal structures (Baconguis et al., 2014; Gonzales et al., 2009; Jasti et al., 2007; Yoder et al., 2018).

E374Q resulted in a shift in the pH_{50act} to more acidic values, and the proposition that this residue plays a role in proton-dependent gating (Yoder & Gouaux, 2018), but again, single functional data related to desensitization is lacking. As with E417 in activation, protonation of E374 may also contribute to the continuous contraction of the central vestibule going from the

open to the desensitized state during desensitization. D433 was previously described as an example in the Results (3.2).

Overall, our results suggest the need for future investigations into the roles of H328 and E374 in desensitization, as well as the roles of E314 in activation, and E98 in both transitions (activation and desensitization). Other residues than the ones discussed can certainly be involved in relevant proton-sensing, but we believe that residues displaying a stronger response to conformational changes likely have increased functional importance.

Chapter 4 : Discussion

ASICs are ligand-gated ion channels with a pH-dependent function (Waldmann et al., 1997). The identification and characterization of their ligand binding sites is the main objective of this thesis. We first used equilibrium MD to sample the local conformational spaces of each functional state to identify state-specific interactions and to investigate the effects of changing protonation states on ASIC1 structural dynamics. This was followed by the simulation of the transition pathways using targeted MD in combination with pK_a prediction, generating a set of ionizable residues that have the potential of being involved in the pH-dependent gating mechanisms of ASIC1.

Protein activity typically implies the notion of a ligand that must bind to the protein, promoting a change in its activity. A ligand-binding event would in turn lead to the formation of relevant interactions between the protein and the ligand, promoting the transition of the protein from a relaxed to a tense or active state (i.e. R -> T) (Monod et al., 1965). Oftentimes, it is the ligand-binding sites of these proteins that are targeted for rational drug design (Reddy & Parrill, 1999). In the case of ASIC1, drugs can be developed to target ASIC-related physiologies such as fear conditioning, learning and memory (Coryell et al., 2007; Wemmie et al., 2013) as well as pathologies, for instance, pain-associated tissue acidosis from injury and ischemia (Issberner et al., 1996; Pan et al., 1999). Identification of the orthosteric binding sites in proteins, more specifically in receptors, is an important step to improve our understanding on a structural level, of how a binding event is translated to a conformational change related to function. Having a

grasp on the molecular mechanisms underlying activation opens the avenue for these sites to be targeted in drug design studies or protein engineering.

Typically, an orthosteric or allosteric ligand binding site can be identified with conventional structural biology studies where ligands can be resolved in complex with a large protein using X-ray crystallography or cryo-EM (Berman et al., 2003). This is, however, challenging with ASICs that have protons as their ligand. Protons have very low electron density making their visualization difficult using the two previously mentioned structural biology techniques. We used MD simulations as protons can be explicitly modeled computationally, however, a drawback is that covalent bonds cannot be formed nor broken during a classical MD simulation. This presents a challenge as we are interested in changes related to proton binding and unbinding events. Thus, we sample different protonation states of ASIC1 ionizable residues, observing the effects of changing protonation states on global and local dynamics for local conformational sampling, as well as for the relevant conformational changes in the transition pathways.

In our experiments, we resorted to the use of PROPKA (Bas et al., 2008; Olsson et al., 2011) for fast pK_a prediction. As described in the Introduction, PROPKA has been optimized to produce results similar to the more exhaustive methods (Poisson-Boltzmann (Jo, Vargyas, et al., 2008; C. Li et al., 2019; Lu et al., 2009; Rocchia et al., 2001) and Generalized Born approaches (Feig et al., 2004; Feig & Brooks, 2004)) that exist, but we can appreciate a lack of accuracy from PROPKA results in comparison to these methods. If using the more exhaustive methods, more accurate predictions would be obtained but at a higher computational cost. With more accurate pK_a predictions, one can more confidently describe the protonation state of a given residue. The pK_a can also be potentially used to look at the energetics of ligand-binding as well. Given the

number of setups sampled in this thesis, it would, however, be unfeasible to perform these intensive predictions, wherefore we took advantage of the speed of PROPKA calculations.

Going back to ligand-binding energetics, the $pK_a = -\log(K_a)$, K_a being the association constant. The association constant can be directly related to free energy terms where $K_a = \frac{1}{K_D}$, where K_D is the dissociation constant. One can thus determine the K_D from accurate pK_a predictions and use the following equation:

$$\Delta G = -RT\ln(K_D)$$

to calculate the change in Gibb's free energy related to proton dissociation. This relation can be used to study the energetics of the pH-dependent gating mechanisms of ASIC1. One can potentially observe whether it is favourable for a certain potential proton-sensor to keep or lose a proton upon a conformational change. However, with an abundance of ionizable residues and still not knowing the specific agonist-bound configurations, these calculations would become highly complex.

A difficulty that has been shown repeatedly in the literature and throughout this thesis, is that there does not appear to be a single proton-sensor that regulates ASIC1 activation. Instead, many residues appear to have a pH-sensing function (Babini et al., 2002; Jasti et al., 2007; Krauson & Carattino, 2016; Liechti et al., 2010; Paukert et al., 2008; Rook, Musgaard, et al., 2021; Vullo et al., 2017). The ACP was initially hypothesized to house the proton-sensors relevant to ASIC1 function, where a protonation event(s) at this site would promote the formation of carboxyl-carboxylate interactions between interfacing ASP and GLU residues on the thumb and finger subdomains, stabilizing a collapsed ACP (Jasti et al., 2007). More recently,

mutagenesis studies of acidic residues outside of the ACP have also resulted in less pH-sensitive mutants. These include residues in the palm domain and wrist regions (Liechti et al., 2010; Lynagh et al., 2018; MacLean & Jayaraman, 2017; Paukert et al., 2008; Rook, Musgaard, et al., 2021). Even a mutant of 16 ionizable residues in the ACP still exhibited pH-dependent function, although it was significantly less proton-sensitive (Vullo et al., 2017).

First, to understand proton-sensing in the ACP, we sampled the protonation states of seven ionizable residues with the potential to form interactions at this site. The strength of the observed interactions in our simulations has been demonstrated to be highly dependent on the placement of the proton. Within an interacting pair, the protonation of one of the acidic residues of the pair favours an interaction between the two, more so than if the other were to be protonated, judged from our data. In real life, it is possible that some of the acidic pairs would share a proton, however, this cannot be accounted for in classical MD simulations as used here.

In analyzing the interactions, other than D238-D346 and E239-D350 (Jasti et al., 2007), non-obvious interactions not appearing in the crystal structures include R191-D238 and E98-E239 in the open state. Interestingly, the E98-E239 interaction is less frequent in the desensitized state, as seen in our simulations in Chapter 2. This observed change in frequency could be of structural relevance in desensitization. In the resting states, E98-E239 and R191-D346 interactions were seldom formed, suggesting perhaps that the formation of these interactions may indicate the start of activation.

E98 is on a buried loop that links the finger to the β-ball domain (Figure 1.2). E98A was reported to reduce the binding of the PcTx1 toxin that stabilizes the open state (Sherwood et al., 2012). If we assume that protonation events promote the formation or breaking of interactions,

these changes in interactions involving ionizable residues may well be implicated in promoting activation or desensitization along with ACP collapse. As mentioned in Chapter 2, an R191A mutant in hASIC1a resulted in a reduction in proton-sensitivity indicating the relevance of this residue in proton-sensing (H. Yang et al., 2009). R191 is highly mobile in our simulations, and we observed it to mediate interactions with multiple acidic residues (D346, D350, E239) simultaneously in the ACP, and this could also contribute to the activation pathway. In our targeted MD of activation from the resting to the open state, R191 begins in its crystal structure conformation low in the ACP, interacting with D260, E314 and H328. The side chain flips upwards in our simulations, picking up interactions with the acidic residues on the thumb and finger domains and, possibly, bringing these residues together and promoting a contracted ACP in activation. This motion occurred more frequently when an open protonation state was imposed on the system in comparison to the resting protonation state (8 of 9 versus 5 of 9 occurrences, respectively). Perhaps this facilitates the formation of interfacing carboxyl-carboxylate interactions as the residues would now be in closer proximity to each other.

Furthermore, with our targeted MD studies, we suggested in Chapter 3 a subset of amino acid residues to be involved in activation, desensitization, and recovery. Of these, H328 and E374 require further investigation in the context of desensitization, E314 in activation, and E98 in both the activation and desensitization pathways. Our pK_a predictions also exhibit different behaviours as discussed in Chapter 3. We split the residues up into three groups: 1) An ionizable residue with a pK_a value dependent on the conformational transition and not apparently affected by a change in protonation state. 2) An ionizable residue dependent on the protonation state to a greater extent than a conformational change. 3) An ionizable residue not dependent on the protonation state or a conformational change – not a proton-sensor. Further investigations would

be required to determine if there is a significant difference between the functions of the first two categories.

Hu et al. combined pK_a prediction with experimental studies to identify and suggest a proton-sensing residue important to the pH-dependent activation of GLIC, a pentameric ligand-gated ion channel (pLGIC). This residue was positioned on the so-called F loop, and this region was proposed to be the orthosteric site of the pH-dependent ion channel. Interestingly, this newly proposed allosteric site, the F loop, is however known to instead be an allosteric site in other pLGICs. Attenuated total reflectance (ATR)/Fourier transform infrared spectroscopy (FTIR) was used to provide experimental evidence for the importance of this site, in the context of existing electrophysiological findings (Hu et al., 2018). Like ASICs, GLICs also have an abundance of acidic residues that may be considered as potential proton-sensors. Although we cannot validate our suggested sites through our systems alone, future mutagenesis studies of these novel residues (E98, E314, H328 and E374) can shed light on their relevance in ASIC1 function.

The following addresses current working hypotheses and current knowledge in the field. The long-standing hypothesis, introduced along with the first cASIC1 structure, describes the ACP as the proton-binding site. This region is highly abundant in acidic residues and these residues were suggested to form carboxyl-carboxylate interactions upon extracellular acidification. The formation of these interactions would lead to a collapsed ACP and these conformational changes could then be transduced through the palm to the gate, leading to channel opening (Jasti et al., 2007). The described collapse of the ACP was experimentally supported by Förster resonance energy transfer (FRET) and voltage clamp fluorometry (VCF) measurements (Ramaswamy et al., 2013; Vullo et al., 2017). However, more recent studies

provide evidence of the ACP not being required for pH-dependent activation (Vullo et al., 2017) and that there are other important proton-binding sites such as the wrist region and the palm domains (Krauson et al., 2013; Liechti et al., 2010). Most mutagenesis studies of potential proton-sensing residues implement neutralization mutants (Jasti et al., 2007) that ultimately mimic a constantly protonated counterpart of the wild type residue (Rook, Musgaard, et al., 2021). This may leave open the possibility for similar hydrogen-bond interactions to form if these interactions are important in pH-sensing.

Our findings, if to be proven experimentally, also lead us to suggest that in addition to the palm domain, the ACP, and the wrist, the TMD also has a pH-dependent function directly related to the desensitization gate. Perhaps it is the opening of the channel that promotes channel gating, where an open channel can now be hydrated with water and H_3O^+ molecules, leading to protonation of the D433 residues in the permeation pathway, promoting channel closure along with the formation of other desensitized state-stabilizing interactions described in Chapter 3.

Fast conformational changes in the ACP and the wrist domains have been associated with activation, and slow conformational changes in the palm domain have been associated with desensitization by VCF, linking protonation sites with the role in ASIC1 gating function (Vullo et al., 2021). However, protonation states or specific residues have not been linked to these motions.

To entertain these motions considering our results, we speculate that first in the ACP, protons will bind to the negatively charged surface made up of many acidic residues. Acidic residues with the highest pK_a values in the resting state are, when changing to low pH, likely to become protonated first. E98 (~ 6-7 in the resting state, Miaro, 2020) deep in the ACP, as well as R191 (always protonated) appear to coordinate the approach of the negatively charged D238-

E239 loop to the thumb helix with D346 and D350. This approach between the two subdomains coincides with the collapse of the ACP. This conformational change is required to reach the active state. The collapse of the ACP is transduced to the palm and then the gate by the "motion" of E98 that couples the motions of the finger domains with the β-ball (Bonifacio et al., 2014; Gwiazda et al., 2015). Possibly at the same time, the β-turn, connected to the thumb domain, is coupled to the TM1. During activation, in ACP collapse, the thumb domain would pull upwards, dragging TM1 along with it, pulling open the TMD. Moving into desensitization from an open channel, motions from the palm domain may promote closure along with the flipping of the β11-12 linker and a concerted contraction of the central vestibule as suggested by the crystal structures of the desensitized state (Baconguis et al., 2014; Baconguis & Gouaux, 2012; Yoder et al., 2018). An influx of protons and their binding to the negatively charged residues in the central vestibule (E80, E374, E412 and E417) during activation could make the inner-facing palm domain less negative over time. This could potentially be beneficial to the contraction of the central vestibule as there may be less repulsive interactions between the charged residues of the three interfacing palm domains. The central vestibule starting from activation would continue to collapse even further as the ion channel progresses to the desensitized state, as suggested by the crystal structures (Baconguis et al., 2014; Dawson et al., 2012; Gonzales et al., 2009; Jasti et al., 2007; Yoder et al., 2018) and volumetric calculations of the central vestibule using CASTp (Bargeton et al., 2019). In desensitization, D433 also becomes protonated and promotes a closed channel (T. Li et al., 2011; L. Yang & Palmer, 2014). This proposed mechanism is illustrated in Figure 4.1.

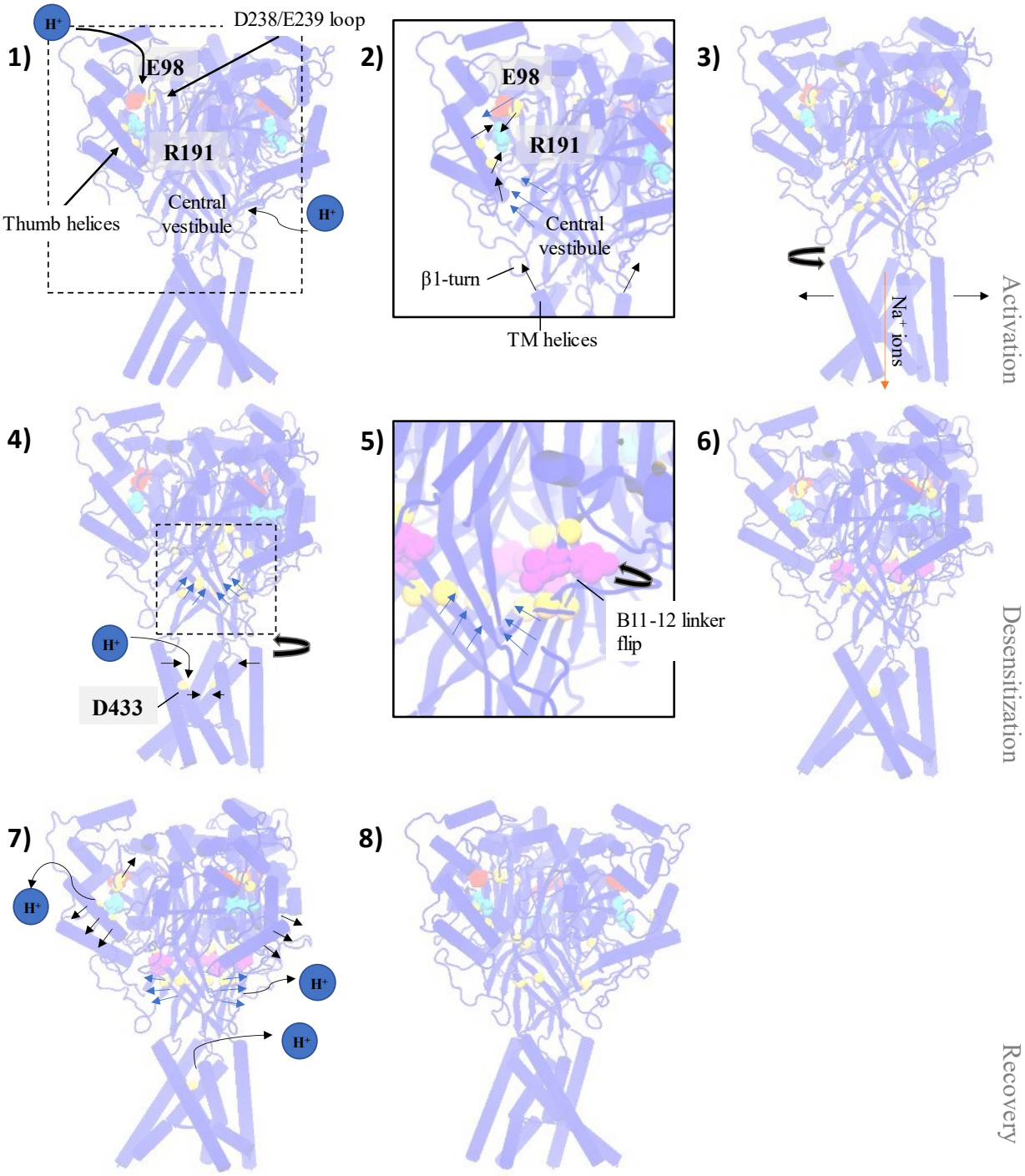

Figure 4.1 A proposed mechanism for the pH-dependent gating cycle of ASIC1.

1) Upon extracellular acidification, protons bind to acidic residues in the ACP and in the central vestibule, perhaps first to residues with the highest pK_a (e.g. E98).
2) A protonated E98 along with R191 act in concert to bring the negatively charged D238/E239 loop towards the thumb domain, promoting interfacing interactions with D346 and D350. R191 mediates contact with multiple negatively charged residues until carboxyl-carboxylate interactions form. As the ACP collapses, the β1-turn follows the motions of the thumb

domain and pulls the TM1 helices open as these two regions are coupled. At the same time, E98 couples the motions of the finger and β-ball domains which can bull on the β-strands in the palm domain leading to collapse of the central vestibule.

3) With the ion channel open, Na^+ can permeate through the channel.
4) As the central vestibule continues to contract, more interactions between acidic residues in this region are formed. With an open channel, protons can potentially bind to D433 in the gate and promote closure of the channel through the formation of hydrogen bond interactions with adjacent subunits. The TMD twists shut.
5) At some point during desensitization, the β11-12 linker flips and the hydrogen bond network between Q277, L414 and E80 forms, decoupling the ECD from the gate.
6) The ion channel is now in a desensitized state at low-pH.
7) Upon extracellular alkalinization, most acidic residues would become deprotonated, leading to repulsion between the subdomains in the ACP and central vestibule. This repulsion would result in the expansion of these cavities pushing the ion channel into a closed, resting state.

As with any method, there are inherent strengths and weaknesses of our research. As mentioned above, MD simulations are a valuable tool to use in the study of ASICs because we can model and observe the effects of explicit hydrogen atoms on protein dynamics. MD simulations are also ideal for the study of the dynamics of large transmembrane proteins that are difficult to isolate in experimental structural studies. Our theoretical observations can also be interpreted in the context of an abundance of existing mutagenesis studies that often lack a structural interpretation (Rook, Musgaard, et al., 2021).

The use of targeted MD also allowed us to simulate conformational changes, providing us with insights into what may occur in a transition pathway at a molecular level. The caveat of this method is the requirement to introduce a biasing force (Schlitter et al., 2006). It is possible that we are not simulating the proper pathway as we guide the position of atoms to a target configuration using RMSD. This implies that the transition pathway follows a direct motion to its target which may overlook more roundabout motions or otherwise intermediate states. Additionally, we assume that the structures we target are representative of the functional states in a membrane environment in solution. This may not be the case for the structures used in this study, potentially being the reason behind the "hyper-twisted" TMD in the desensitized and resting states. Perhaps a less strained structure from our previous unbiased simulations could have been used as a target state as a comparison. In addition, we were not able to observe the flipping of the β11-12 linker in desensitization that was described to decouple the conformational changes in the ACP to the TMD (Gonzales et al., 2009; Jasti et al., 2007; Rook et al., 2020). This could be because in our targeted MD simulations, the biasing force constraints are only applied to the backbone atoms of the ASIC1 structure and not to the atoms of the side chains which would usually go through the flipping motion. Additionally, linker flipping is a slow process.

Unbiased simulations of the L414A mutant (a mutant with characteristically faster desensitization and recovery time constants than WT) only exhibited a full flip of the linker in one instance of three repeats with simulation times of 400 ns (Rook et al., 2020). Our simulation times in our targeted MD following the application of the biasing force (40 ns) were not enough to sample the flip of the L414 and N415 side chains. The quality or relevance of the structures we use is not limited to only targeted MD. Structure quality also determines the quality of our models in general.

In both Chapter 2 and Chapter 3, we assume that by changing the protonation states of residues nearby a residue of interest, the dynamics and pK_a of the residue being measured will not be affected, which is false. However, with 64 ASP, GLU and HIS residues in each subunit of the existing structures (65 in 5WKU), this assumption is made for a more straightforward interpretation. Not knowing the correct protonation states, the issue we are studying is also a hindrance in terms of the assignment of static protonation states at the start of each simulation. We have shown in my previous work (Miaro, 2020) and through this thesis that protonation states do affect channel dynamics, making it difficult to determine the proper protonation states with MD simulations and pK_a prediction alone.

There remain many avenues for future research. In this thesis, we study the proton-binding sites at the molecular level with MD simulations for the conformational changes of the main three transition pathways in a global manner. Moving forward, more attention can be directed towards the determination of the function of crucial proton-binding sites in the pH-dependent processes of activation, desensitization, recovery from desensitization and steady-state desensitization (SSD).

Not previously described in this thesis, SSD involves the transition from a resting state to a desensitized state without entering an open state. SSD is induced by the introduction of a mildly acidic pH (non-activating pH i.e. ~7) or slow acidification (Babini et al., 2002; Immke & McCleskey, 2003; Todorović et al., 2005). This phenomenon is characterized through electrophysiology as a reduction in activity at activating pH following exposure to mildly stimulating conditions. Studies report evidence of the role of SSD of ASIC1a in the prevention of acidosis-mediated neuron death (Sherwood et al., 2009; Sherwood & Askwith, 2008). The process cannot be measured directly but if a channel were to undergo SSD and the pH of the sample was thereafter reduced to an activating pH, there would be a reduced or lack of response (Sherwood et al., 2012). This is because ASIC1 ion channels can only be activated from the resting state. Not only activation is pH-dependent. SSD is also invoked through pH-sensing. The SSD process has a higher proton affinity than activation as SSD occurs at lower proton concentrations (Babini et al., 2002). Multiple studies suggest that the same proton-sensitive binding sites are shared in activation and desensitization and thus, these processes are coupled (Bargeton & Kellenberger, 2010; Liechti et al., 2010; Sherwood & Askwith, 2008). Mutants of E235 and E254 in hASIC1a have been reported to affect the apparent proton-sensitivity of SSD while having a minimal effect on the pH_{50} of activation (Liechti et al., 2010). However, from a structural point of view, the molecular mechanisms behind the pH-dependence of steady-state desensitization remains elusive. Is the endpoint conformation of SSD similar to the desensitized state following activation?

We have also shown that a hydrogen-bond network in the palm domain retards recovery from desensitization in ASIC1, yet the process still retains pH-dependence with the Q277G/Q277N mutant constructs. Thus, this hydrogen-bond network cannot account for the

entire mechanism (Rook, Miaro, et al., 2021). Other proton sensors must be involved, and thus further investigation needs to be performed to determine the other elements affecting this function.

A logical approach for the study of a pH-dependent receptor from a computational perspective would be to perform simulations under physiological conditions. Constant-pH simulations allow one to simulate systems at a constant pH value of choice (J. Chen et al., 2008; Khandogin & Brooks, 2007; Mongan et al., 2004; Wallace & Shen, 2009). In these simulations, the protonation states of ionizable residues can be changed during the simulation by function of a criterion that determines the likelihood that a titratable residue is to be protonated or not. There are two general types of constant pH simulations, discrete pHMD (DpHMD) and continuous pHMD. DpHMD involves additional Monte Carlo (MC) steps to the usual classical MD steps to update the protonation states of ionizable residues and these methods typically use an implicit solvent model (Baptista et al., 2002). CpHMD is a more recent method that does not require extra MC sampling steps, cutting down on computational time (Khandogin & Brooks, 2005; Lee et al., 2004). Limitations exist for both methods regarding the solvent model used (implicit vs explicit), the time to convergence for ionizable residues, and an accurate representation of conformational dynamics. CpHMD methods are continuously being developed to be efficient in terms of computation time, sampling, and accuracy (W. Chen et al., 2014). Recently, a method has been implemented with GROMACS, the simulation engine used throughout this project. This new approach addresses the high computational costs associated with calculating long-range electrostatics of titratable residues which is high for large biomolecules. The authors argue that their method is more comparable to computation times of conventional MD simulations with

GROMACS, unlike other existing methods (Aho et al., 2022). This makes it an attractive option for future simulations of ASIC1.

CpHMD can be applied to ASICs to determine the occupancy of protons on sites of interest, drawing attention to residues with high proton occupancy at a given pH. Long-time scales should ideally be used to simulate unbiased transition pathways to sample a physiologically relevant transition pathway at a target pH (e.g. the simulation of the resting state structure at pH 5). This may reveal structurally how proton-binding transduces opening of the gate at a molecular level. The formation of important interactions or changes in electrostatics and dynamics can moreover be evaluated directly.

Another computational method we had begun to explore was the use of protein structure networks. This form of analysis renders the protein structure and dynamics as a mathematical representation where atoms and interactions are reduced to nodes and edges (Girvan & Newman, 2002), respectively, using graph theory (Strogatz, 2001). A downstream analysis, named path analysis, can be applied to networks to find nodes or residues that are important in the communication between distal communities (Freeman, 1977). The method has been used to pinpoint important regions involved in allosteric communication between two distanced sites (Greene, 2012). Applying this analysis to our data to study how distant regions such as the ACP and palm domains communicate with the gate and to observe the differences that appear between the functional states, essentially how changes in protonation affect the networks, would be interesting. This analysis is of course difficult when we do not know exactly what residues should be protonated. Given that protonation states already have a visible effect on protein dynamics, it would be unsurprising if dynamical networks also displayed changes as a result of differing protonation states on the same structure.

From an experimental perspective, our suggested residues, E98, E314, R191, and H328 should be further investigated. As discussed previously by Rook et al. (Rook, Musgaard, et al., 2021), most mutagenesis studies targeting potential proton sensors used neutralization mutants, swapping ASP/GLU for ASN/GLN residues. As such, the mutants have a constantly protonated counterpart to the WT side chain meaning that ASIC can still retain function. The authors suggested charge-swap mutations that had more drastic effects on pH-sensing resulting in bi-phasic curves (Rook, Musgaard, et al., 2021). We would suggest removing the side chain altogether to eliminate the possibility of forming any interactions with the residue of interest with ALA mutants. A methyl side chain in place of the WT ionizable residues removes the possibility for any electrostatic interactions and this is expected to impede proton-sensing in the ACP and palm domain to a greater extent than the neutralization mutants. A quadruple E98A/R191A/D238A/E239A mutant, consisting of residues we show to participate in frequent interactions in the low-pH states compared to the resting states (Chapter 2), may have drastic effects on the pH-sensing ability of the ACP as the main interactions between the finger and thumb domains (E239-D346, R191-D238, R191-D346, R191-D350) would not be able to form. This implies an impeded pinching motion that may be worse at translating a signal to the gate.

In conclusion, this research aimed to investigate the effects of protonation states on ASIC1 dynamics and ultimately characterize the ligand-binding sites of the ion channels relevant to the gating mechanisms. A combination of MD simulations and pK_a prediction was used to study this problem from a structurally focused angle. We have shown that changes in protonation states can have stark effects on ASIC1 dynamics, and our approach led us to identify ionizable residues potentially important in ASIC1 activity to be investigated in the future. Advancements in structural biology and constant-pH simulation methods will yield more physiological insights

on the proton-binding sites to be validated, opening the door for rational drug design and in providing a detailed molecular understanding of the proton-driven conformational changes of ASICs.

References

Abraham, M. J., Murtola, T., Schulz, R., Páll, S., Smith, J. C., Hess, B., & Lindah, E. (2015). Gromacs: High performance molecular simulations through multi-level parallelism from laptops to supercomputers. *SoftwareX*, *1–2*, 19–25. https://doi.org/10.1016/j.softx.2015.06.001

Afonine, P. V., Grosse-Kunstleve, R. W., Echols, N., Headd, J. J., Moriarty, N. W., Mustyakimov, M., Terwilliger, T. C., Urzhumtsev, A., Zwart, P. H., & Adams, P. D. (2012). Towards automated crystallographic structure refinement with phenix.refine. *Acta Crystallographica Section D: Biological Crystallography*, *68*(4), 352–367. https://doi.org/10.1107/S0907444912001308

Aho, N., Buslaev, P., Jansen, A., Bauer, P., Groenhof, G., & Hess, B. (2022). *Scalable Constant pH Molecular Dynamics in GROMACS*. https://doi.org/10.26434/CHEMRXIV-2022-N025T

Alexander, S. P. H., Peters, J. A., Kelly, E., Marrion, N. V., Faccenda, E., Harding, S. D., Pawson, A. J., Sharman, J. L., Southan, C., & Davies, J. A. (2017). THE CONCISE GUIDE TO PHARMACOLOGY 2017/18: Ligand-gated ion channels. *British Journal of Pharmacology*, *174*(Suppl Suppl 1), S130–S159. https://doi.org/10.1111/BPH.13879/FULL

Alvarez de la Rosa, D., Canessa, C. M., Fyfe, G. K., & Zhang, P. (2000). Structure and regulation of amiloride-sensitive sodium channels. *Annual Review of Physiology*, *62*, 573–594. https://doi.org/10.1146/ANNUREV.PHYSIOL.62.1.573

Andersen, J. F., Ding, X. D., Balfour, C., Shokhireva, T. K., Champagne, D. E., Walker, F. A., & Montfort, W. R. (2000). Kinetics and equilibria in ligand binding by nitrophorins 1-4: evidence for stabilization of a nitric oxide-ferriheme complex through a ligand-induced conformational trap. *Biochemistry*, *39*(33), 10118–10131. https://doi.org/10.1021/BI000766B

Babini, E., Paukert, M., Geisler, H. S., & Gründer, S. (2002). Alternative Splicing and Interaction with Di- and Polyvalent Cations Control the Dynamic Range of Acid-sensing Ion Channel 1 (ASIC1). *Journal of Biological Chemistry*, *277*(44), 41597–41603.

https://doi.org/10.1074/JBC.M205877200

Baconguis, I., Bohlen, C. J., Goehring, A., Julius, D., & Gouaux, E. (2014). X-Ray Structure of Acid-Sensing Ion Channel 1–Snake Toxin Complex Reveals Open State of a Na+-Selective Channel. *Cell*, *156*(4), 717–729. https://doi.org/10.1016/j.cell.2014.01.011

Baconguis, I., & Gouaux, E. (2012). Structural plasticity and dynamic selectivity of acid-sensing ion channelspider toxin complexes. *Nature*, *489*(7416), 400–405. https://doi.org/10.1038/nature11375

Baconguis, I., Hattori, M., & Gouaux, E. (2013). Unanticipated parallels in architecture and mechanism between ATP-gated P2X receptors and acid sensing ion channels. *Current Opinion in Structural Biology*, *23*(2), 277. https://doi.org/10.1016/J.SBI.2013.04.005

Baptista, A. M., Teixeira, V. H., Soares, C. M., Nio, A., Baptista, M., Udio, C., & Soares, M. (2002). Constant-pH molecular dynamics using stochastic titration. *The Journal of Chemical Physics*, *117*(9), 4184. https://doi.org/10.1063/1.1497164

Bargeton, B., Iwaszkiewicz, J., Bonifacio, G., Roy, S., Zoete, V., & Kellenberger, S. (2019). Mutations in the palm domain disrupt modulation of acid-sensing ion channel 1a currents by neuropeptides. *Scientific Reports 2019 9:1*, *9*(1), 1–14. https://doi.org/10.1038/s41598-018-37426-5

Bargeton, B., & Kellenberger, S. (2010). The Contact Region between Three Domains of the Extracellular Loop of ASIC1a Is Critical for Channel Function. *The Journal of Biological Chemistry*, *285*(18), 13816. https://doi.org/10.1074/JBC.M109.086843

Barker, B. S., Young, G. T., Soubrane, C. H., Stephens, G. J., Stevens, E. B., & Patel, M. K. (2017). Ion Channels. *Conn's Translational Neuroscience*, 11–43. https://doi.org/10.1016/B978-0-12-802381-5.00002-6

Bas, D. C., Rogers, D. M., & Jensen, J. H. (2008). Very fast prediction and rationalization of pKa values for protein–ligand complexes. *Proteins: Structure, Function, and Bioinformatics*, *73*(3), 765–783. https://doi.org/10.1002/PROT.22102

Bässler, E. L., Ngo-Anh, T. J., Geisler, H. S., Ruppersberg, J. P., & Gründer, S. (2001). Molecular and Functional Characterization of Acid-sensing Ion Channel (ASIC) 1b.

Journal of Biological Chemistry, *276*(36), 33782–33787. https://doi.org/10.1074/JBC.M104030200

Benson, C. J., Xie, J., Wemmie, J. A., Price, M. P., Henss, J. M., Welsh, M. J., & Snyder, P. M. (2002). Heteromultimers of DEG/ENaC subunits form H+-gated channels in mouse sensory neurons. *Proceedings of the National Academy of Sciences of the United States of America*, *99*(4), 2338–2343. https://doi.org/10.1073/pnas.032678399

Berendsen, H. J. C., Postma, J. P. M., Van Gunsteren, W. F., Dinola, A., & Haak, J. R. (1984). Molecular dynamics with coupling to an external bath. *The Journal of Chemical Physics*, *81*(8), 3684–3690. https://doi.org/10.1063/1.448118

Berman, H., Henrick, K., & Nakamura, H. (2003). Announcing the worldwide Protein Data Bank. *Nature Structural Biology*, *10*(12), 980. https://doi.org/10.1038/NSB1203-980

Bernèche, S., & Roux, B. (2001). Energetics of ion conduction through the K+ channel. *Nature*, *414*(6859), 73–77. https://doi.org/10.1038/35102067

Bocquet, N., Prado De Carvalho, L., Cartaud, J., Neyton, J., Le Poupon, C., Taly, A., Grutter, T., Changeux, J. P., & Corringer, P. J. (2006). A prokaryotic proton-gated ion channel from the nicotinic acetylcholine receptor family. *Nature 2006 445:7123*, *445*(7123), 116–119. https://doi.org/10.1038/nature05371

Bohlen, C. J., Chesler, A. T., Sharif-Naeini, R., Medzihradszky, K. F., Zhou, S., King, D., Sánchez, E. E., Burlingame, A. L., Basbaum, A. I., & Julius, D. (2011). A heteromeric Texas coral snake toxin targets acid-sensing ion channels to produce pain. *Nature*, *479*(7373), 410–414. https://doi.org/10.1038/NATURE10607

Bonifacio, G., Lelli, C. I. S., & Kellenberger, S. (2014). Protonation controls ASIC1a activity via coordinated movements in multiple domains. *The Journal of General Physiology*, *143*(1), 105–118. https://doi.org/10.1085/JGP.201311053

Bonomi, M., Branduardi, D., Bussi, G., Camilloni, C., Provasi, D., Raiteri, P., Donadio, D., Marinelli, F., Pietrucci, F., Broglia, R. A., & Parrinello, M. (2009). PLUMED: A portable plugin for free-energy calculations with molecular dynamics. *Computer Physics Communications*, *180*(10), 1961–1972. https://doi.org/10.1016/J.CPC.2009.05.011

Brunger, A. T., & Adams, P. D. (2002). Molecular dynamics applied to X-ray structure refinement. *Accounts of Chemical Research*, *35*(6), 404–412. https://doi.org/10.1021/AR010034R

Bürgi, R., Kollman, P. A., & Van Gunsteren, W. F. (2002). Simulating proteins at constant pH: An approach combining molecular dynamics and Monte Carlo simulation. *Proteins: Structure, Function, and Bioinformatics*, *47*(4), 469–480. https://doi.org/10.1002/PROT.10046

Capurro, V., Gianotti, A., Caci, E., Ravazzolo, R., Galietta, L. J. V., & Zegarra-Moran, O. (2015). Functional analysis of acid-activated Cl^- channels: properties and mechanisms of regulation. *Biochimica et Biophysica Acta*, *1848*(1 Pt A), 105–114. https://doi.org/10.1016/J.BBAMEM.2014.10.008

Chen, J., Brooks, C. L., & Khandogin, J. (2008). Recent advances in implicit solvent based methods for biomolecular simulations. *Current Opinion in Structural Biology*, *18*(2), 140. https://doi.org/10.1016/J.SBI.2008.01.003

Chen, W., Morrow, B. H., Shi, C., & Shen, J. K. (2014). Recent development and application of constant pH molecular dynamics. *Https://Doi.Org/10.1080/08927022.2014.907492*, *40*(10–11), 830–838. https://doi.org/10.1080/08927022.2014.907492

Chen, X., Kalbacher, H., & Gründer, S. (2005). The Tarantula Toxin Psalmotoxin 1 Inhibits Acid-sensing Ion Channel (ASIC) 1a by Increasing Its Apparent H+ Affinity. *The Journal of General Physiology*, *126*(1), 71. https://doi.org/10.1085/JGP.200509303

Chu, X. P., Wemmie, J. A., Wang, W. Z., Zhu, X. M., Saugstad, J. A., Price, M. P., Simon, R. P., & Xiong, Z. G. (2004). Subunit-Dependent High-Affinity Zinc Inhibition of Acid-Sensing Ion Channels. *The Journal of Neuroscience*, *24*(40), 8678. https://doi.org/10.1523/JNEUROSCI.2844-04.2004

Clark, A. J., Tiwary, P., Borrelli, K., Feng, S., Miller, E. B., Abel, R., Friesner, R. A., & Berne, B. J. (2016). Prediction of Protein-Ligand Binding Poses via a Combination of Induced Fit Docking and Metadynamics Simulations. *Journal of Chemical Theory and Computation*, *12*(6), 2990–2998.

https://doi.org/10.1021/ACS.JCTC.6B00201/SUPPL_FILE/CT6B00201_SI_001.PDF

Cordero-Morales, J. F., Jogini, V., Lewis, A., Vásquez, V., Cortes, D. M., Roux, B., & Perozo, E. (2007). Molecular driving forces determining potassium channel slow inactivation. *Nature Structural & Molecular Biology 2007 14:11*, *14*(11), 1062–1069. https://doi.org/10.1038/nsmb1309

Coryell, M. W., Ziemann, A. E., Westmoreland, P. J., Haenfler, J. M., Kurjakovic, Z., Zha, X., Price, M. P., Schnizler, M. K., & Wemmie, J. A. (2007). Targeting ASIC1a reduces innate fear and alters neuronal activity in the fear circuit. *Biological Psychiatry*, *62*(10), 1140–1148. https://doi.org/10.1016/J.BIOPSYCH.2007.05.008

Cvitkovic, J. P., Pauplis, C. D., & Kaminski, G. A. (2019). PKA17—A Coarse-Grain Grid-Based Methodology and Web-Based Software for Predicting Protein p K_a Shifts. *Journal of Computational Chemistry*, *40*(18), 1718–1726. https://doi.org/10.1002/jcc.25826

Darden, T., York, D., & Pedersen, L. (1993). Particle mesh Ewald: An N·log(N) method for Ewald sums in large systems. *The Journal of Chemical Physics*, *98*(12), 10089–10092. https://doi.org/10.1063/1.464397

Davies, M. N., Toseland, C. P., Moss, D. S., & Flower, D. R. (2006). Benchmarking pKa prediction. *BMC Biochemistry*, *7*, 18. https://doi.org/10.1186/1471-2091-7-18

Dawson, R. J. P., Benz, J., Stohler, P., Tetaz, T., Joseph, C., Huber, S., Schmid, G., Hügin, D., Pflimlin, P., Trube, G., Rudolph, M. G., Hennig, M., & Ruf, A. (2012). Structure of the Acid-sensing ion channel 1 in complex with the gating modifier Psalmotoxin 1. *Nature Communications 2012 3:1*, *3*(1), 1–8. https://doi.org/10.1038/ncomms1917

del Toro, D., Carrasquero-Ordaz, M. A., Chu, A., Ruff, T., Shahin, M., Jackson, V. A., Chavent, M., Berbeira-Santana, M., Seyit-Bremer, G., Brignani, S., Kaufmann, R., Lowe, E., Klein, R., & Seiradake, E. (2020). Structural Basis of Teneurin-Latrophilin Interaction in Repulsive Guidance of Migrating Neurons. *Cell*, *180*(2), 323. https://doi.org/10.1016/J.CELL.2019.12.014

Delemotte, L., Tarek, M., Klein, M. L., Amaral, C., & Treptow, W. (2011). Intermediate states of the Kv1.2 voltage sensor from atomistic molecular dynamics simulations. *Proceedings of*

the National Academy of Sciences of the United States of America, *108*(15), 6109–6114. https://doi.org/10.1073/PNAS.1102724108/-/DCSUPPLEMENTAL

Diochot, S., Baron, A., Salinas, M., Douguet, D., Scarzello, S., Dabert-Gay, A. S., Debayle, D., Friend, V., Alloui, A., Lazdunski, M., & Lingueglia, E. (2012). Black mamba venom peptides target acid-sensing ion channels to abolish pain. *Nature*, *490*(7421), 552–555. https://doi.org/10.1038/NATURE11494

Dror, R. O., Green, H. F., Valant, C., Borhani, D. W., Valcourt, J. R., Pan, A. C., Arlow, D. H., Canals, M., Lane, J. R., Rahmani, R., Baell, J. B., Sexton, P. M., Christopoulos, A., & Shaw, D. E. (2013). Structural basis for modulation of a G-protein-coupled receptor by allosteric drugs. *Nature 2013 503:7475*, *503*(7475), 295–299. https://doi.org/10.1038/nature12595

Du, J., Reznikov, L. R., Price, M. P., Zha, X., Lu, Y., Moninger, T. O., Wemmie, J. A., & Welsh, M. J. (2014). Protons are a neurotransmitter that regulates synaptic plasticity in the lateral amygdala. *Proceedings of the National Academy of Sciences*, *111*(24), 8961–8966. https://doi.org/10.1073/PNAS.1407018111

Escoubas, P., De Weille, J. R., Lecoq, A., Diochot, S., Waldmann, R., Champigny, G., Moinier, D., Menez, A., & Lazdunski, M. (2000). Isolation of a tarantula toxin specific for a class of proton-gated Na+ channels. *The Journal of Biological Chemistry*, *275*(33), 25116–25121. https://doi.org/10.1074/JBC.M003643200

Essmann, U., Perera, L., Berkowitz, M. L., Darden, T., Lee, H., & Pedersen, L. G. (1995). A smooth particle mesh Ewald method. *The Journal of Chemical Physics*, *103*(19), 8577–8593. https://doi.org/10.1063/1.470117

Feig, M., & Brooks, C. L. (2004). Recent advances in the development and application of implicit solvent models in biomolecule simulations. *Current Opinion in Structural Biology*, *14*(2), 217–224. https://doi.org/10.1016/J.SBI.2004.03.009

Feig, M., Onufriev, A., Lee, M. S., Im, W., Case, D. A., & Brooks, C. L. (2004). Performance comparison of generalized born and Poisson methods in the calculation of electrostatic solvation energies for protein structures. *Journal of Computational Chemistry*, *25*(2), 265–

284. https://doi.org/10.1002/JCC.10378

Freeman, L. C. (1977). A Set of Measures of Centrality Based on Betweenness. *Sociometry*, *40*(1), 35. https://doi.org/10.2307/3033543

Georgescu, R. E., Alexov, E. G., & Gunner, M. R. (2002). Combining conformational flexibility and continuum electrostatics for calculating pK(a)s in proteins. *Biophysical Journal*, *83*(4), 1731–1748. https://doi.org/10.1016/S0006-3495(02)73940-4

Gielen, M., & Corringer, P. J. (2018). The dual-gate model for pentameric ligand-gated ion channels activation and desensitization. *The Journal of Physiology*, *596*(10), 1873. https://doi.org/10.1113/JP275100

Girvan, M., & Newman, M. E. J. (2002). Community structure in social and biological networks. *Proceedings of the National Academy of Sciences of the United States of America*, *99*(12), 7821–7826. https://doi.org/10.1073/PNAS.122653799/ASSET/B8593464-1EFB-4723-9B55-0AAF2E3D4494/ASSETS/GRAPHIC/PQ1226537007.JPEG

Gonzales, E. B., Kawate, T., & Gouaux, E. (2009). Pore architecture and ion sites in acid-sensing ion channels and P2X receptors. *Nature*, *460*(7255), 599–604. https://doi.org/10.1038/nature08218

Gowers, R., Linke, M., Barnoud, J., Reddy, T., Melo, M., Seyler, S., Domański, J., Dotson, D., Buchoux, S., Kenney, I., & Beckstein, O. (2016). MDAnalysis: A Python Package for the Rapid Analysis of Molecular Dynamics Simulations. *Proceedings of the 15th Python in Science Conference*, 98–105. https://doi.org/10.25080/majora-629e541a-00e

Greene, L. H. (2012). Protein structure networks. *Briefings in Functional Genomics*, *11*(6), 469–478. https://doi.org/10.1093/BFGP/ELS039

Grubmüller, H., Heymann, B., & Tavan, P. (1996). Ligand Binding: Molecular Mechanics Calculation of the Streptavidin-Biotin Rupture Force. *Science*, *271*(5251), 997–999. https://doi.org/10.1126/SCIENCE.271.5251.997

Gründer, S., & Pusch, M. (2015). Biophysical properties of acid-sensing ion channels (ASICs). In *Neuropharmacology* (Vol. 94, pp. 9–18). Elsevier Ltd. https://doi.org/10.1016/j.neuropharm.2014.12.016

Gwiazda, K., Bonifacio, G., Vullo, S., & Kellenberger, S. (2015). Extracellular Subunit Interactions Control Transitions between Functional States of Acid-sensing Ion Channel 1a. *The Journal of Biological Chemistry*, *290*(29), 17956–17966. https://doi.org/10.1074/JBC.M115.641688

Hamelberg, D., Mongan, J., & McCammon, J. A. (2004). Accelerated molecular dynamics: A promising and efficient simulation method for biomolecules. *The Journal of Chemical Physics*, *120*(24), 11919. https://doi.org/10.1063/1.1755656

Harder, E., Damm, W., Maple, J., Wu, C., Reboul, M., Xiang, J. Y., Wang, L., Lupyan, D., Dahlgren, M. K., Knight, J. L., Kaus, J. W., Cerutti, D. S., Krilov, G., Jorgensen, W. L., Abel, R., & Friesner, R. A. (2016). OPLS3: A Force Field Providing Broad Coverage of Drug-like Small Molecules and Proteins. *Journal of Chemical Theory and Computation*, *12*(1), 281–296. https://doi.org/10.1021/ACS.JCTC.5B00864

Hess, B., Bekker, H., C Berendsen, H. J., & E M Fraaije, J. G. (1997). *3 LINCS: a linear constraint solver for molecular simulations* (Vol. 18).

Hesselager, M., Timmermann, D. B., & Ahring, P. K. (2004). pH Dependency and Desensitization Kinetics of Heterologously Expressed Combinations of Acid-sensing Ion Channel Subunits *. *Journal of Biological Chemistry*, *279*(12), 11006–11015. https://doi.org/10.1074/JBC.M313507200

Hollingsworth, S. A., & Dror, R. O. (2018). Molecular dynamics simulation for all. *Neuron*, *99*(6), 1129. https://doi.org/10.1016/J.NEURON.2018.08.011

Hoover, W. G. (1985). Canonical dynamics: Equilibrium phase-space distributions. *Physical Review A*, *31*(3), 1695–1697. https://doi.org/10.1103/PhysRevA.31.1695

Hu, H., Ataka, K., Menny, A., Fourati, Z., Sauguet, L., Corringer, P. J., Koehl, P., Heberle, J., & Delarue, M. (2018). Electrostatics, proton sensor, and networks governing the gating transition in GLIC, a proton-gated pentameric ion channel. *Proceedings of the National Academy of Sciences of the United States of America*, *115*(52), E12172–E12181. https://doi.org/10.1073/PNAS.1813378116/SUPPL_FILE/PNAS.1813378116.SAPP.PDF

Huang, J., Rauscher, S., Nawrocki, G., Ran, T., Feig, M., De Groot, B. L., Grubmüller, H., &

MacKerell, A. D. (2016). CHARMM36m: An improved force field for folded and intrinsically disordered proteins. *Nature Methods*, *14*(1), 71–73. https://doi.org/10.1038/nmeth.4067

Humphrey, W., Dalke, A., & Schulten, K. (1996). VMD: Visual molecular dynamics. *Journal of Molecular Graphics*, *14*(1), 33–38. https://doi.org/10.1016/0263-7855(96)00018-5

Immke, D. C., & McCleskey, E. W. (2003). Protons open acid-sensing ion channels by catalyzing relief of Ca2+ blockade. *Neuron*, *37*(1), 75–84. https://doi.org/10.1016/S0896-6273(02)01130-3

Issberner, U., Reeh, P. W., & Steen, K. H. (1996). Pain due to tissue acidosis: a mechanism for inflammatory and ischemic myalgia? *Neuroscience Letters*, *208*(3), 191–194. https://doi.org/10.1016/0304-3940(96)12576-3

Jasti, J., Furukawa, H., Gonzales, E. B., & Gouaux, E. (2007). Structure of acid-sensing ion channel 1 at 1.9 Å resolution and low pH. *Nature*, *449*(7160), 316–323. https://doi.org/10.1038/nature06163

Jo, S., Kim, T., Iyer, V. G., & Im, W. (2008). CHARMM-GUI: A web-based graphical user interface for CHARMM. *Journal of Computational Chemistry*, *29*(11), 1859–1865. https://doi.org/10.1002/jcc.20945

Jo, S., Vargyas, M., Vasko-Szedlar, J., Roux, B., & Im, W. (2008). PBEQ-Solver for online visualization of electrostatic potential of biomolecules. *Nucleic Acids Research*, *36*(Web Server issue). https://doi.org/10.1093/NAR/GKN314

Kandt, C., Ash, W. L., & Peter Tieleman, D. (2007). Setting up and running molecular dynamics simulations of membrane proteins. *Methods*, *41*(4), 475–488. https://doi.org/10.1016/j.ymeth.2006.08.006

Kellenberger, S., & Schild, L. (2002). Epithelial sodium channel/degenerin family of ion channels: a variety of functions for a shared structure. *Physiological Reviews*, *82*(3), 735–767. https://doi.org/10.1152/PHYSREV.00007.2002

Khakh, B. S., & North, R. A. (2012). Neuromodulation by extracellular ATP and P2X receptors in the CNS. *Neuron*, *76*(1), 51. https://doi.org/10.1016/J.NEURON.2012.09.024

Khandogin, J., & Brooks, C. L. (2005). Constant pH Molecular Dynamics with Proton Tautomerism. *Biophysical Journal*, *89*(1), 141. https://doi.org/10.1529/BIOPHYSJ.105.061341

Khandogin, J., & Brooks, C. L. (2007). *Molecular Simulations of pH-Mediated Biological Processes*. https://doi.org/10.1016/S1574-1400(07)03001-0

Klauda, J. B., Venable, R. M., Freites, J. A., O'Connor, J. W., Tobias, D. J., Mondragon-Ramirez, C., Vorobyov, I., MacKerell, A. D., & Pastor, R. W. (2010). Update of the CHARMM All-Atom Additive Force Field for Lipids: Validation on Six Lipid Types. *Journal of Physical Chemistry B*, *114*(23), 7830–7843. https://doi.org/10.1021/JP101759Q/SUPPL_FILE/JP101759Q_SI_001.PDF

Krauson, A. J., & Carattino, M. D. (2016). The Thumb Domain Mediates Acid-sensing Ion Channel Desensitization. *Journal of Biological Chemistry*, *291*(21), 11407–11419. https://doi.org/10.1074/JBC.M115.702316

Krauson, A. J., Rued, A. C., & Carattino, M. D. (2013). Independent contribution of extracellular proton binding sites to ASIC1a activation. *The Journal of Biological Chemistry*, *288*(48), 34375–34383. https://doi.org/10.1074/JBC.M113.504324

Kusama, N., Harding, A. M. S., & Benson, C. J. (2010). Extracellular chloride modulates the desensitization kinetics of Acid-sensing Ion Channel 1a (ASIC1a). *Journal of Biological Chemistry*, *285*(23), 17425–17431. https://doi.org/10.1074/jbc.M109.091561

Laio, A., & Parrinello, M. (2002). Escaping free-energy minima. *Proceedings of the National Academy of Sciences of the United States of America*, *99*(20), 12562–12566. https://doi.org/10.1073/PNAS.202427399

Lee, M. S., Salsbury, F. R., & Brooks, C. L. (2004). Constant-pH molecular dynamics using continuous titration coordinates. *Proteins*, *56*(4), 738–752. https://doi.org/10.1002/PROT.20128

Li, C., Jia, Z., Chakravorty, A., Pahari, S., Peng, Y., Basu, S., Koirala, M., Panday, S. K., Petukh, M., Li, L., & Alexov, E. (2019). DelPhi Suite: New Developments and Review of Functionalities. *Journal of Computational Chemistry*, *40*(28), 2502.

https://doi.org/10.1002/JCC.26006

Li, H., Robertson, A. D., & Jensen, J. H. (2005). Very fast empirical prediction and rationalization of protein pKa values. *Proteins*, *61*(4), 704–721. https://doi.org/10.1002/PROT.20660

Li, T., Yang, Y., & Canessa, C. M. (2011). Asp433 in the closing gate of ASIC1 determines stability of the open state without changing properties of the selectivity filter or Ca 2+ block. *Journal of General Physiology*, *137*(3), 289–297. https://doi.org/10.1085/jgp.201010576

Liechti, L. A., Bernèche, S., Bargeton, B., Iwaszkiewicz, J., Roy, S., Michielin, O., & Kellenberger, S. (2010). A Combined Computational and Functional Approach Identifies New Residues Involved in pH-dependent Gating of ASIC1a *. *Journal of Biological Chemistry*, *285*(21), 16315–16329. https://doi.org/10.1074/JBC.M109.092015

Lindorff-Larsen, K., Maragakis, P., Piana, S., Eastwood, M. P., Dror, R. O., & Shaw, D. E. (2012). Systematic Validation of Protein Force Fields against Experimental Data. *PLoS ONE*, *7*(2), 32131. https://doi.org/10.1371/JOURNAL.PONE.0032131

Liu, Y., Ke, M., & Gong, H. (2015). Protonation of Glu135 Facilitates the Outward-to-Inward Structural Transition of Fucose Transporter. *Biophysical Journal*, *109*(3), 542–551. https://doi.org/10.1016/J.BPJ.2015.06.037

Lomize, M. A., Pogozheva, I. D., Joo, H., Mosberg, H. I., & Lomize, A. L. (2012). OPM database and PPM web server: resources for positioning of proteins in membranes. *Nucleic Acids Research*, *40*(Database issue). https://doi.org/10.1093/NAR/GKR703

Lu, B., Cheng, X., Huang, J., & McCammon, J. A. (2009). An Adaptive Fast Multipole Boundary Element Method for Poisson-Boltzmann Electrostatics. *Journal of Chemical Theory and Computation*, *5*(6), 1692–1699. https://doi.org/10.1021/CT900083K

Lynagh, T., Mikhaleva, Y., Colding, J. M., Glover, J. C., & Pless, S. A. (2018). Acid-sensing ion channels emerged over 600 Mya and are conserved throughout the deuterostomes. *Proceedings of the National Academy of Sciences*, *115*(33), 8430–8435. https://doi.org/10.1073/PNAS.1806614115

MacLean, D. M., & Jayaraman, V. (2017). Deactivation kinetics of acid-sensing ion channel 1a are strongly pH-sensitive. *Proceedings of the National Academy of Sciences of the United States of America*, *114*(12), E2504–E2513. https://www.pnas.org/content/114/12/E2504

Mark, P., & Nilsson, L. (2001). Structure and dynamics of the TIP3P, SPC, and SPC/E water models at 298 K. *Journal of Physical Chemistry A*, *105*(43), 9954–9960. https://doi.org/10.1021/jp003020w

Miaro, M. (2020). *Predicition of the protonation states of acid-sensing ion channel 1a [Unpublished honours thesis]*.

Michaud-Agrawal, N., Denning, E. J., Woolf, T. B., & Beckstein, O. (2011). MDAnalysis: A toolkit for the analysis of molecular dynamics simulations. *Journal of Computational Chemistry*, *32*(10), 2319–2327. https://doi.org/10.1002/jcc.21787

Milletti, F., Storchi, L., & Cruciani, G. (2009). Predicting protein pK(a) by environment similarity. *Proteins*, *76*(2), 484–495. https://doi.org/10.1002/PROT.22363

Mongan, J., & Case, D. A. (2005). Biomolecular simulations at constant pH. *Current Opinion in Structural Biology*, *15*(2), 157–163. https://doi.org/10.1016/J.SBI.2005.02.002

Mongan, J., Case, D. A., & Mccammon, J. A. (2004). *Constant pH Molecular Dynamics in Generalized Born Implicit Solvent*. https://doi.org/10.1002/jcc.20139

Monod, J., Wyman, J., & Changeux, J. P. (1965). On the nature of allosteric transitions: A plausible model. *Journal of Molecular Biology*, *12*(1), 88–118. https://doi.org/10.1016/S0022-2836(65)80285-6

Noreng, S., Bharadwaj, A., Posert, R., Yoshioka, C., & Baconguis, I. (2018). Structure of the human epithelial sodium channel by cryo-electron microscopy. *ELife*, *7*. https://doi.org/10.7554/ELIFE.39340

Nosé, S. (1984). A molecular dynamics method for simulations in the canonical ensemble. *Molecular Physics*, *52*(2), 255–268. https://doi.org/10.1080/00268978400101201

Olsson, M. H. M., Søndergaard, C. R., Rostkowski, M., & Jensen, J. H. (2011). PROPKA3: Consistent Treatment of Internal and Surface Residues in Empirical p K_a Predictions.

Journal of Chemical Theory and Computation, *7*(2), 525–537. https://doi.org/10.1021/ct100578z

Pan, H.-L., Longhurst, J. C., Eisenach, J. C., & Chen, S.-R. (1999). Role of protons in activation of cardiac sympathetic C-fibre afferents during ischaemia in cats. *The Journal of Physiology*, *518*(Pt 3), 857. https://doi.org/10.1111/J.1469-7793.1999.0857P.X

Parrinello, M., & Rahman, A. (1981). Polymorphic transitions in single crystals: A new molecular dynamics method. *Journal of Applied Physics*, *52*(12), 7182–7190. https://doi.org/10.1063/1.328693

Paukert, M., Chen, X., Polleichtner, G., Schindelin, H., & Gründer, S. (2008). Candidate amino acids involved in H+ gating of acid-sensing ion channel 1a. *Journal of Biological Chemistry*, *283*(1), 572–581. https://doi.org/10.1074/jbc.M706811200

Qin, B. Y., Bewley, M. C., Creamer, L. K., Baker, H. M., Baker, E. N., & Jameson, G. B. (1998). Structural basis of the tanford transition of bovine β-lactoglobulin. *Biochemistry*, *37*(40), 14014–14023. https://doi.org/10.1021/BI981016T/SUPPL_FILE/BI981016T_S.PDF

Radak, B. K., Chipot, C., Suh, D., Jo, S., Jiang, W., Phillips, J. C., Schulten, K., & Roux, B. (2017). Constant-pH Molecular Dynamics Simulations for Large Biomolecular Systems. *Journal of Chemical Theory and Computation*, *13*(12), 5933–5944. https://doi.org/10.1021/ACS.JCTC.7B00875/SUPPL_FILE/CT7B00875_SI_001.PDF

Ramaswamy, S. S., Maclean, D. M., Gorfe, A. A., Jayaraman, V., & St, F. (2013). *Proton mediated conformational changes in an Acid Sensing Ion Channel The LRET experiments on the triple mutant D238A/E239A/ D260A shows no changes in the*. https://doi.org/10.1074/jbc.M113.478982

Rang, H. P., Bevan, S., & Dray, A. (1991). Chemical activation of nociceptive peripheral neurones. *British Medical Bulletin*, *47*(3), 534–548. https://doi.org/10.1093/OXFORDJOURNALS.BMB.A072491

Reddy, M. R., & Parrill, A. L. (1999). *Overview of Rational Drug Design*. https://pubs.acs.org/sharingguidelines

Robustelli, P., Piana, S., & Shaw, D. E. (2018). Developing a molecular dynamics force field for both folded and disordered protein states. *Proceedings of the National Academy of Sciences of the United States of America*, *115*(21), E4758–E4766. https://doi.org/10.1073/PNAS.1800690115/-/DCSUPPLEMENTAL

Rocchia, W., Alexov, E., & Honig, B. (2001). Extending the Applicability of the Nonlinear Poisson−Boltzmann Equation: Multiple Dielectric Constants and Multivalent Ions†. *Journal of Physical Chemistry B*, *105*(28), 6507–6514. https://doi.org/10.1021/JP010454Y

Rook, M. L., Miaro, M., Couch, T., Kneisley, D. L., Musgaard, M., & MacLean, D. M. (2021). Mutation of a conserved glutamine residue does not abolish desensitization of acid-sensing ion channel 1. *Journal of General Physiology*, *153*(8). https://doi.org/10.1085/jgp.202012855

Rook, M. L., Musgaard, M., & MacLean, D. M. (2021). Coupling structure with function in acid-sensing ion channels: challenges in pursuit of proton sensors. *The Journal of Physiology*, *599*(2), 417–430. https://doi.org/10.1113/JP278707

Rook, M. L., Williamson, A., Lueck, J. D., Musgaard, M., & Maclean, D. M. (2020). β11-12 linker isomerization governs acid-sensing ion channel desensitization and recovery. *ELife*, *9*. https://doi.org/10.7554/eLife.51111

Ruan, Z., Osei-Owusu, J., Du, J., Qiu, Z., & Lü, W. (2020). Structures and pH-sensing mechanism of the proton-activated chloride channel. *Nature 2020 588:7837*, *588*(7837), 350–354. https://doi.org/10.1038/s41586-020-2875-7

Sato-Numata, K., Numata, T., & Okada, Y. (2014). Temperature sensitivity of acid-sensitive outwardly rectifying (ASOR) anion channels in cortical neurons is involved in hypothermic neuroprotection against acidotoxic necrosis. *Channels (Austin, Tex.)*, *8*(3), 278–283. https://doi.org/10.4161/CHAN.27748

Schlick, T., & Portillo-Ledesma, S. (2021). Biomolecular modeling thrives in the age of technology. *Nature Computational Science 2021 1:5*, *1*(5), 321–331. https://doi.org/10.1038/s43588-021-00060-9

Schlitter, J., Engels, M., KrüGer, P., Jacoby, E., & Wollmer, A. (2006). Targeted Molecular

Dynamics Simulation of Conformational Change-Application to the T ↔ R Transition in Insulin. *Http://Dx.Doi.Org/10.1080/08927029308022170*, *10*(2–6), 291–308. https://doi.org/10.1080/08927029308022170

Shaikh, S. A., & Tajkhorshid, E. (2008). Potential cation and H+ binding sites in acid sensing ion channel-1. *Biophysical Journal*, *95*(11), 5153–5164. https://doi.org/10.1529/biophysj.108.141606

Sherwood, T., & Askwith, C. C. (2008). Endogenous arginine-phenylalanine-amide-related peptides alter steady-state desensitization of ASIC1a. *The Journal of Biological Chemistry*, *283*(4), 1818–1830. https://doi.org/10.1074/JBC.M705118200

Sherwood, T., Franke, R., Conneely, S., Joyner, J., Arumugan, P., & Askwith, C. (2009). Identification of Protein Domains That Control Proton and Calcium Sensitivity of ASIC1a. *The Journal of Biological Chemistry*, *284*(41), 27899. https://doi.org/10.1074/JBC.M109.029009

Sherwood, T., Frey, E. N., & Askwith, C. C. (2012). Structure and activity of the acid-sensing ion channels. In *American Journal of Physiology - Cell Physiology* (Vol. 303, Issue 7, p. C699). American Physiological Society. https://doi.org/10.1152/ajpcell.00188.2012

Sherwood, T., Lee, K. G., Gormley, M. G., & Askwith, C. C. (2011). Heteromeric acid-sensing ion channels (ASICs) composed of ASIC2b and ASIC1a display novel channel properties and contribute to acidosis-induced neuronal death. *Journal of Neuroscience*, *31*(26), 9723–9734. https://doi.org/10.1523/JNEUROSCI.1665-11.2011

Smith, P., Ziolek, R. M., Gazzarrini, E., Owen, D. M., & Lorenz, C. D. (2019). On the interaction of hyaluronic acid with synovial fluid lipid membranes. *Physical Chemistry Chemical Physics*, *21*(19), 9845–9857. https://doi.org/10.1039/c9cp01532a

Stanton, C. L., & Houk, K. N. (2008). Benchmarking pKa Prediction Methods for Residues in Proteins. *Journal of Chemical Theory and Computation*, *4*(6), 951–966. https://doi.org/10.1021/CT8000014

Strogatz, S. H. (2001). Exploring complex networks. *Nature 2001 410:6825*, *410*(6825), 268–276. https://doi.org/10.1038/35065725

Sugita, Y., & Okamoto, Y. (1999). Replica-exchange molecular dynamics method for protein folding. *Chemical Physics Letters*, *314*(1–2), 141–151. https://doi.org/10.1016/S0009-2614(99)01123-9

Sun, D., Liu, S., Li, S., Zhang, M., Yang, F., Wen, M., Shi, P., Wang, T., Pan, M., Chang, S., Zhang, X., Zhang, L., Tian, C., & Liu, L. (2020). Structural insights into human acid-sensing ion channel 1a inhibition by snake toxin mambalgin1. *ELife*, *9*, 1–49. https://doi.org/10.7554/ELIFE.57096

Sutherland, S. P., Benson, C. J., Adelman, J. P., & McCleskey, E. W. (2001). Acid-sensing ion channel 3 matches the acid-gated current in cardiac ischemia-sensing neurons. *Proceedings of the National Academy of Sciences of the United States of America*, *98*(2), 711–716. https://doi.org/10.1073/PNAS.98.2.711/ASSET/96C7B932-FF49-4111-BDF0-FC08D45E8921/ASSETS/GRAPHIC/PQ0114044005.JPEG

Tan, K. P., Nguyen, T. B., Patel, S., Varadarajan, R., & Madhusudhan, M. S. (2013). Depth: a web server to compute depth, cavity sizes, detect potential small-molecule ligand-binding cavities and predict the pKa of ionizable residues in proteins. *Nucleic Acids Research*, *41*(Web Server issue). https://doi.org/10.1093/NAR/GKT503

Tanford, C., & Taggart, V. G. (1961). Ionization-linked Changes in Protein Conformation. II. The N → R Transition in β-Lactoglobulin. *Journal of the American Chemical Society*, *83*(7), 1634–1638. https://doi.org/10.1021/JA01468A022/ASSET/JA01468A022.FP.PNG_V03

Tianbo, L., Youshan, Y., & Canessa, C. M. (2009). Interaction of the Aromatics Tyr-72/Trp-288 in the Interface of the Extracellular and Transmembrane Domains Is Essential for Proton Gating of Acid-sensing Ion Channels. *Journal of Biological Chemistry*, *284*(7), 4689–4694. https://doi.org/10.1074/JBC.M805302200

Todorović, N., Ćorić, T., Zhang, P., & Canessa, C. (2005). Effects of extracellular calcium on fASIC1 currents. *Annals of the New York Academy of Sciences*, *1048*, 331–336. https://doi.org/10.1196/ANNALS.1342.030

Torrie, G. M., & Valleau, J. P. (1977). Nonphysical sampling distributions in Monte Carlo free-

energy estimation: Umbrella sampling. *Journal of Computational Physics*, *23*(2), 187–199. https://doi.org/10.1016/0021-9991(77)90121-8

Tribello, G. A., Bonomi, M., Branduardi, D., Camilloni, C., & Bussi, G. (2014). PLUMED 2: New feathers for an old bird. *Computer Physics Communications*, *185*(2), 604–613. https://doi.org/10.1016/J.CPC.2013.09.018

Ullrich, F., Blin, S., Lazarow, K., Daubitz, T., von Kries, J. P., & Jentsch, T. J. (2019). Identification of TMEM206 proteins as pore of PAORAC/ASOR acid-sensitive chloride channels. *ELife*, *8*. https://doi.org/10.7554/ELIFE.49187

Vanommeslaeghe, K., & MacKerell, A. D. (2012). Automation of the CHARMM general force field (CGenFF) I: Bond perception and atom typing. *Journal of Chemical Information and Modeling*, *52*(12), 3144–3154. https://doi.org/10.1021/CI300363C/SUPPL_FILE/CI300363C_SI_001.ZIP

Vullo, S., Ambrosio, N., Kucera, J. P., Bignucolo, O., & Kellenberger, S. (2021). Kinetic analysis of asic1a delineates conformational signaling from proton-sensing domains to the channel gate. *ELife*, *10*. https://doi.org/10.7554/ELIFE.66488

Vullo, S., Bonifacio, G., Roy, S., Johner, N., Bernèche, S., & Kellenberger, S. (2017). Conformational dynamics and role of the acidic pocket in ASIC pH-dependent gating. *Proceedings of the National Academy of Sciences*, *114*(14), 3768–3773. https://doi.org/10.1073/PNAS.1620560114

Wacker, D., Wang, S., McCorvy, J. D., Betz, R. M., Venkatakrishnan, A. J., Levit, A., Lansu, K., Schools, Z. L., Che, T., Nichols, D. E., Shoichet, B. K., Dror, R. O., & Roth, B. L. (2017). Crystal Structure of an LSD-Bound Human Serotonin Receptor. *Cell*, *168*(3), 377-389.e12. https://doi.org/10.1016/J.CELL.2016.12.033

Waldmann, R., Champigny, G., Bassilana, F., Heurteaux, C., & Lazdunski, M. (1997). A proton-gated cation channel involved in acid-sensing. *Nature*, *386*(6621), 173–177. https://doi.org/10.1038/386173a0

Wallace, J. A., & Shen, J. K. (2009). Predicting pKa Values with Continuous Constant pH Molecular Dynamics. *Methods in Enzymology*, *466*, 455–475.

https://doi.org/10.1016/S0076-6879(09)66019-5

Wang, H. Y., Shimizu, T., Numata, T., & Okada, Y. (2007). Role of acid-sensitive outwardly rectifying anion channels in acidosis-induced cell death in human epithelial cells. *Pflugers Archiv : European Journal of Physiology*, *454*(2), 223–233. https://doi.org/10.1007/S00424-006-0193-Z

Wang, L., Li, L., & Alexov, E. (2015). pKa predictions for proteins, RNAs, and DNAs with the Gaussian dielectric function using DelPhi pKa. *Proteins*, *83*(12), 2186–2197. https://doi.org/10.1002/PROT.24935

Wang, Y., Guo, Y., Li, G., Liu, C., Wang, L., Zhang, A., Yan, Z., & Song, C. (2021). The push-to-open mechanism of the tethered mechanosensitive ion channel nompc. *ELife*, *10*. https://doi.org/10.7554/ELIFE.58388

Webb, B., & Sali, A. (2016). Comparative protein structure modeling using MODELLER. *Current Protocols in Bioinformatics*, *2016*, 5.6.1-5.6.37. https://doi.org/10.1002/cpbi.3

Weichsel, A., Andersen, J. F., Roberts, S. A., & Montfort, W. R. (2000). Nitric oxide binding to nitrophorin 4 induces complete distal pocket burial. *Nature Structural Biology*, *7*(7), 551–554. https://doi.org/10.1038/76769

Wemmie, J. A., Chen, J., Askwith, C. C., Hruska-Hageman, A. M., Price, M. P., Nolan, B. C., Yoder, P. G., Lamani, E., Hoshi, T., Freeman, J. H., & Welsh, M. J. (2002). The acid-activated ion channel ASIC contributes to synaptic plasticity, learning, and memory. *Neuron*, *34*(3), 463–477. https://doi.org/10.1016/S0896-6273(02)00661-X

Wemmie, J. A., Taugher, R. J., & Kreple, C. J. (2013). Acid-sensing ion channels in pain and disease. *Nature Reviews. Neuroscience*, *14*(7), 461–471. https://doi.org/10.1038/NRN3529

Wu, Y., Chen, Z., & Canessa, C. M. (2019). A valve-like mechanism controls desensitization of functional mammalian isoforms of acid-sensing ion channels. *ELife*, *8*. https://doi.org/10.7554/eLife.45851

Wu, Y., Chen, Z., Sigworth, F. J., & Canessa, C. M. (2021). Structure and analysis of nanobody binding to the human asic1a ion channel. *ELife*, *10*. https://doi.org/10.7554/ELIFE.67115

Yang, H., Yu, Y., Li, W. G., Yu, F., Cao, H., Xu, T. Le, & Jiang, H. (2009). Inherent dynamics of the acid-sensing ion channel 1 correlates with the gating mechanism. *PLoS Biology*, *7*(7), 30700145. https://doi.org/10.1371/journal.pbio.1000151

Yang, J., Chen, J., Del Carmen Vitery, M., Osei-Owusu, J., Chu, J., Yu, H., Sun, S., & Qiu, Z. (2019). PAC, an evolutionarily conserved membrane protein, is a proton-activated chloride channel. *Science (New York, N.Y.)*, *364*(6438), 395–399. https://doi.org/10.1126/SCIENCE.AAV9739

Yang, L., & Palmer, L. G. (2014). Ion conduction and selectivity in acid-sensing ion channel 1. *The Journal of General Physiology*, *144*(3), 245. https://doi.org/10.1085/JGP.201411220

Yoder, N., & Gouaux, E. (2018). Divalent cation and chloride ion sites of chicken acid sensing ion channel 1a elucidated by x-ray crystallography. *PLOS ONE*, *13*(8), e0202134. https://doi.org/10.1371/JOURNAL.PONE.0202134

Yoder, N., & Gouaux, E. (2020). The his-gly motif of acid-sensing ion channels resides in a reentrant 'loop' implicated in gating and ion selectivity. *ELife*, *9*, 1–18. https://doi.org/10.7554/eLife.56527

Yoder, N., Yoshioka, C., & Gouaux, E. (2018). Gating mechanisms of acid-sensing ion channels. *Nature*, *555*(7696), 397–401. https://doi.org/10.1038/nature25782

Appendix A

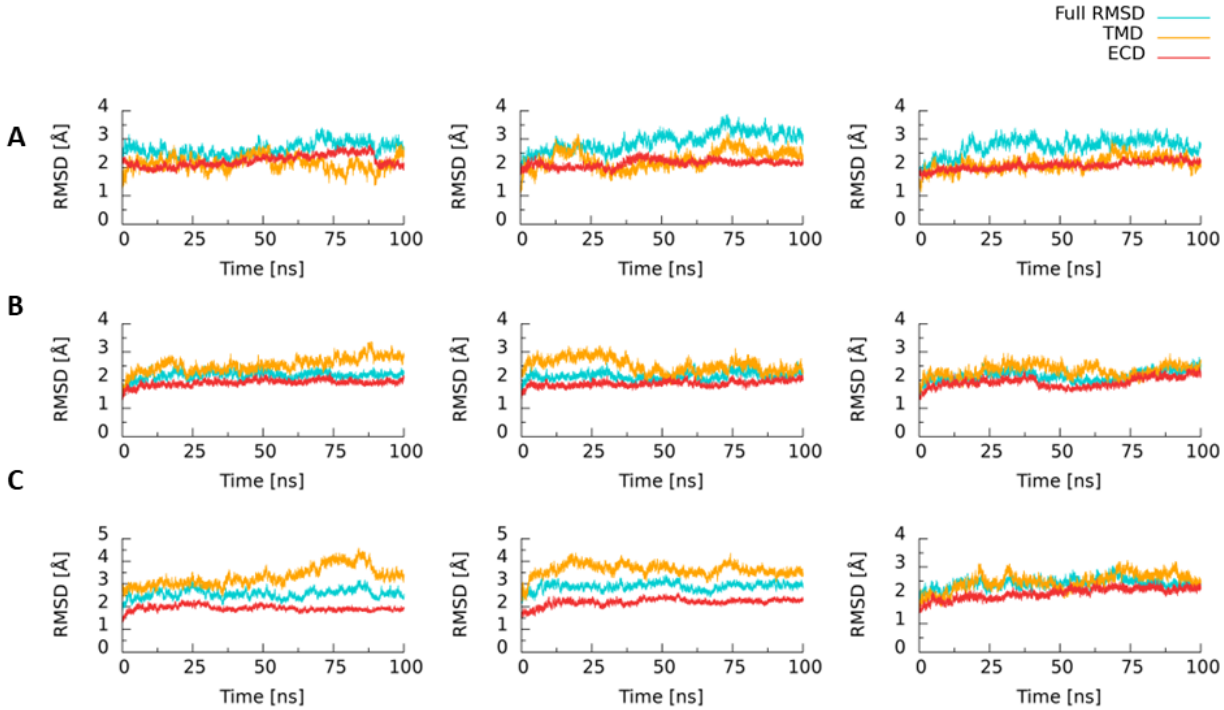

Appendix A Figure 4.1 Control RMSD measurements.
The C_α RMSD between the starting structure and each frame is measured for systems of A) the resting state with resting protonation, B) the open state with open protonation, and C) the desensitized state with desensitized protonation. The RMSDs of the entire channel, the TMD (residues 42 to 72 and 426 to 459 for the resting state; 45 to 72 and 426 to 456 for the open state; 45 to 72 and 426 to 455 for the desensitized state) and the ECD (residues 73 to 426) are shown.

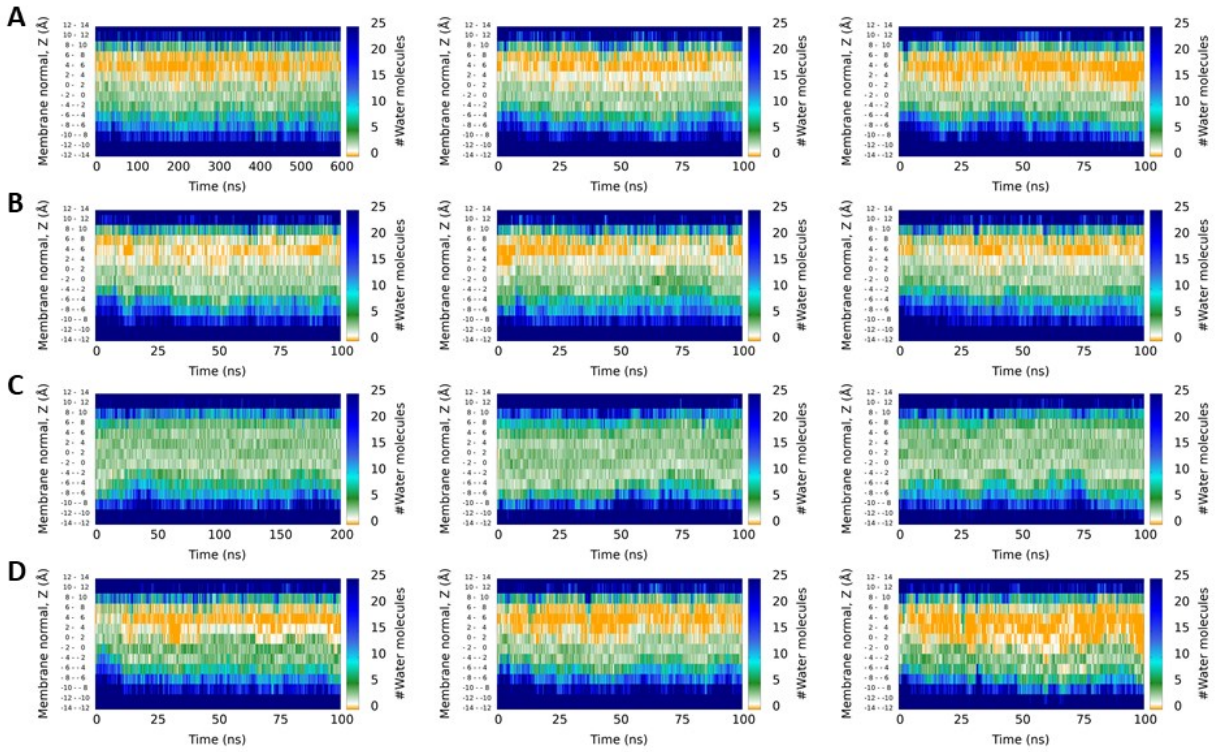

Appendix A Figure 4.2 Pore hydration along the permeation pathway.
Plots representing the number of water molecules along subsections of the membrane normal along the pore permeation pathway. The y-axis represents the length of the TMD from the top of the membrane to below as shown in Figure 2.1. A) Resting state with open protonation, (B) resting state with E98 and D408 protonated, (C) open state with desensitized protonation and (D) desensitized state with resting protonation, respectively. Note the different time scales of the x-axis.

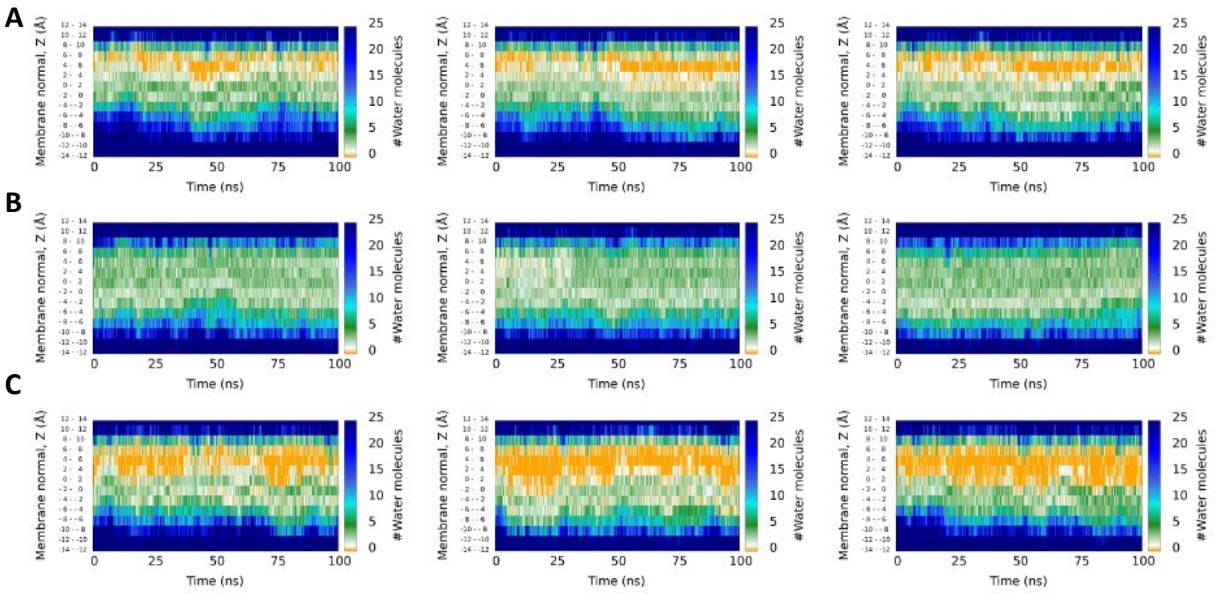

Appendix A Figure 4.3 Control pore hydration along the permeation pathway.
Same as in Appendix A 4.1 above. A) Resting state with open protonation, (B) open state with open protonation and (C) desensitized state with desensitized protonation, respectively.

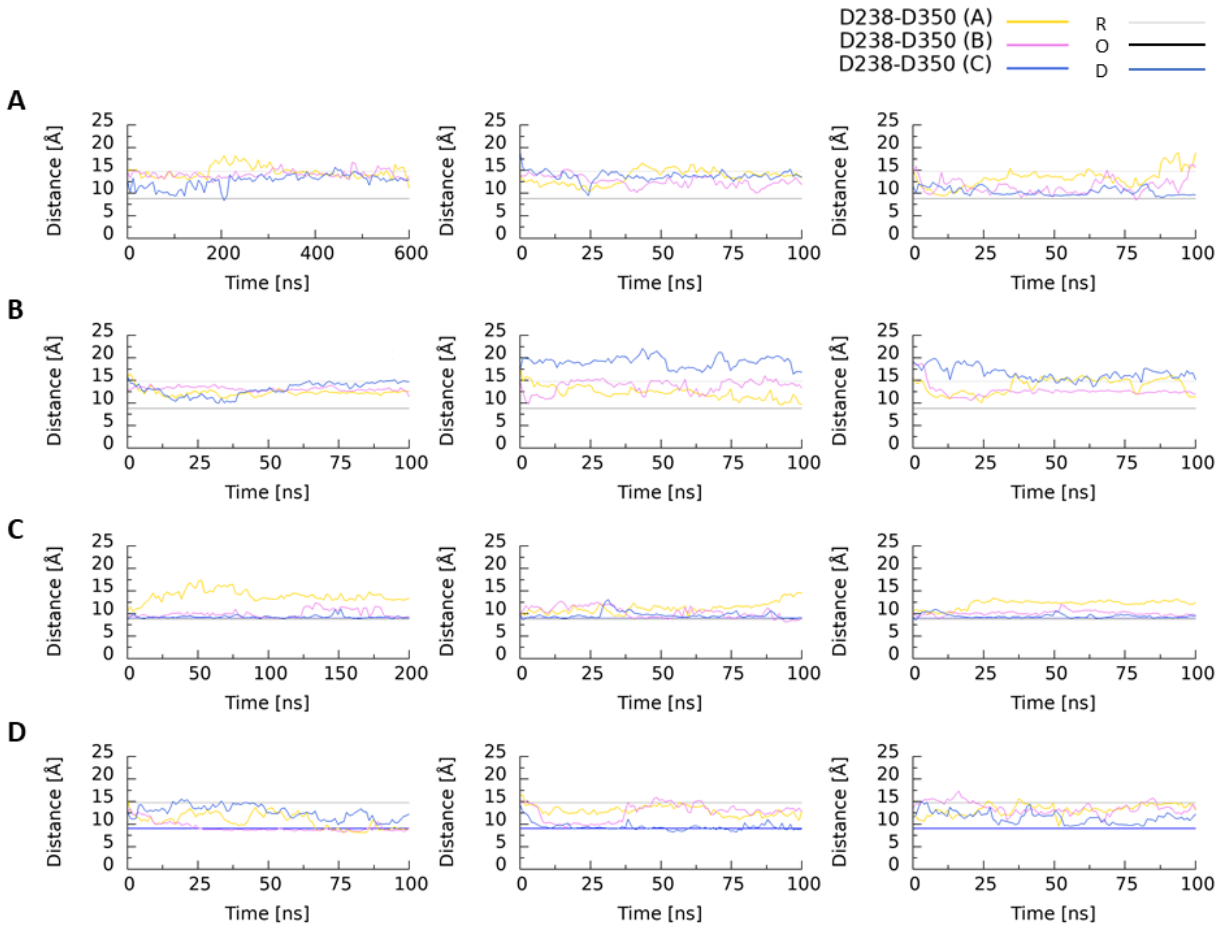

Appendix A Figure 4.4 C_α distances in the acidic pocket between D238 and D350.
(A) Resting state with open protonation, (B) resting state with E98 and D408 protonated, (C) open state with desensitized protonation, and (D) desensitized state with resting protonation. R (gray), O (black) and D (blue) represent the average distance between the Cα atoms of D238 and D350 for all three chains in the resting state (14.78 Å), open state (8.81 Å), and desensitized state (9.02 Å) crystal structures. R, O, D standards are drawn twice on each plot to represent the start and end of a conformational transition (i.e., the plots for "activation" (B) have the average distances for the resting and open state crystal structures only).

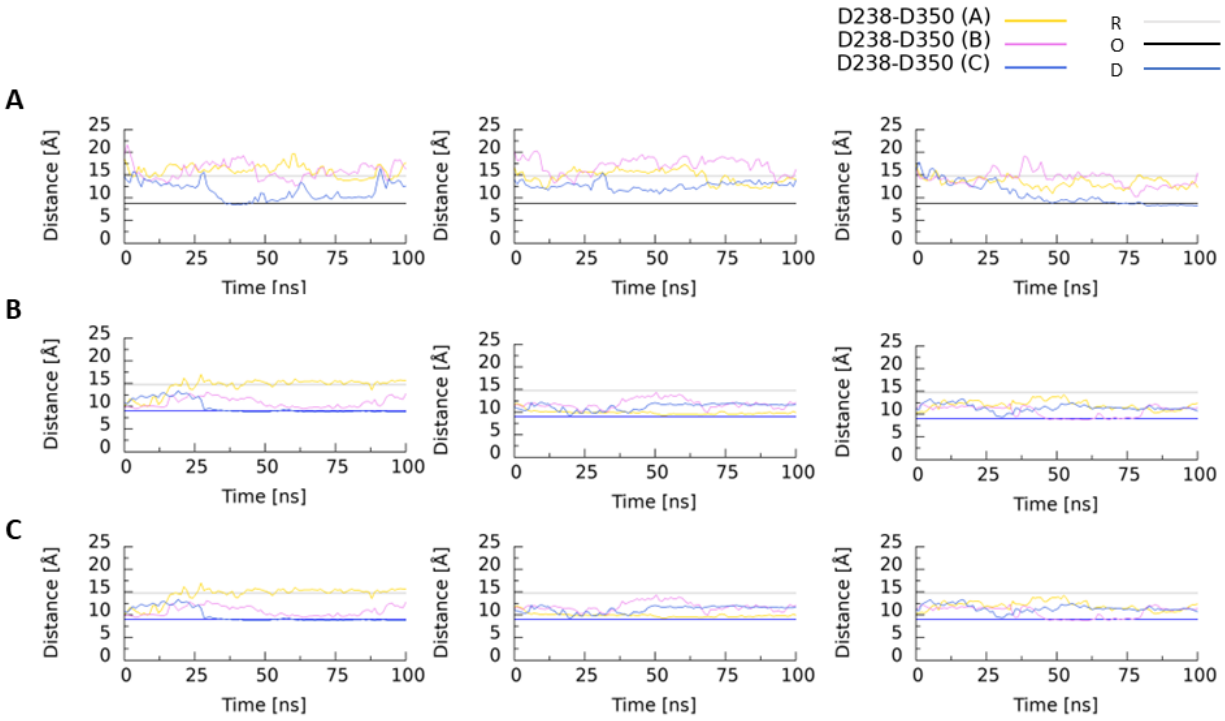

Appendix A Figure 4.5 Control C_α distances in the acidic pocket between D238 and D350. Same as in Appendix A Figure 4.4. (A) Resting state with resting protonation, (B) open with open protonation and (C) resting with resting protonation. R (gray), O (black) and D (blue) represent the average distance between the Cα atoms of D238 and D350 for all three chains in the resting state (14.78 Å), open state (8.81 Å), and desensitized state (9.02 Å) crystal structures. R, O, D standards are drawn twice on each plot to represent the start and end of a conformational transition (i.e., the plots for "activation" (B) have the average distances for the resting and open state crystal structures only).

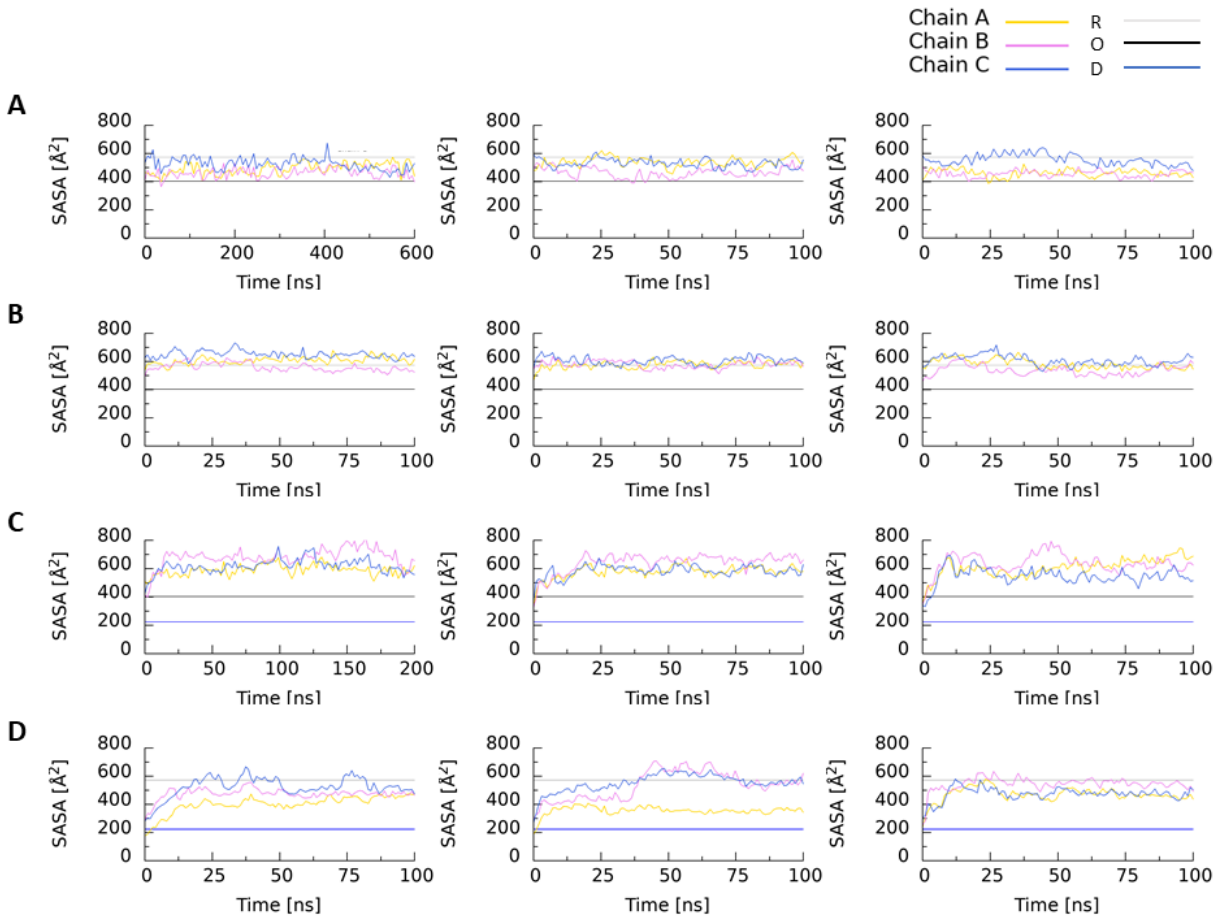

Appendix A Figure 4.6 Solvent-accessible surface area (SASA) of the palm domain. SASA measurements of the palm domain for each chain in the (A) resting state with open protonation, (B) resting state with E98 and D408 protonated, (C) open state with desensitized protonation and, desensitized with resting protonation state systems, respectively. R (gray), O (black) and D (blue) represent the SASA of the crystal structures for the resting (537.4 Å^2), open (402.3 Å^2) and desensitized (222.5 Å^2) states, respectively. Strangely, desensitization displayed SASA similar to the resting state crystal structure – see subsequent chapters.

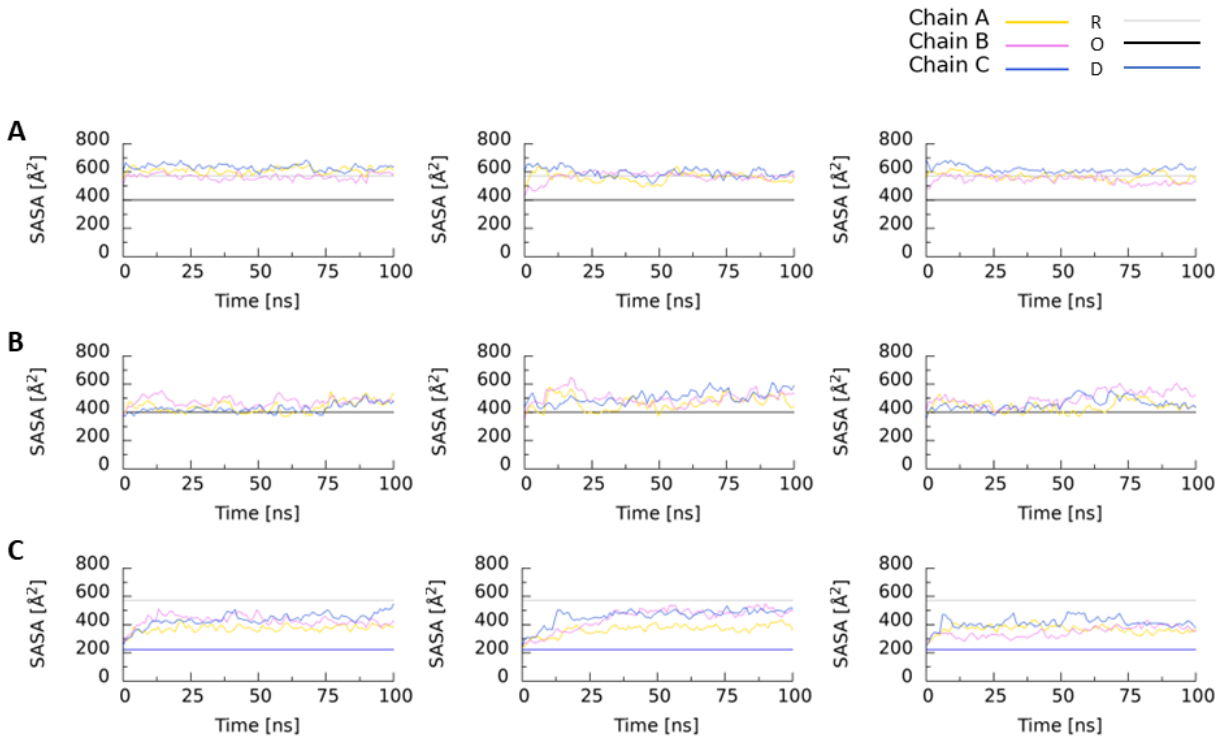

Appendix A Figure 4.7 Control solvent-accessible surface areas (SASA) of the palm domain.

SASA measurements of the palm domain for each chain in a A) resting state with resting protonation, B) open state with open protonation and C) desensitized with desensitized protonation state systems, respectively. R (gray), O (black) and D (blue) represent the SASA of the crystal structures for the resting (537.4 Å^2), open (402.3 Å^2) and desensitized (222.5 Å^2) states, respectively.

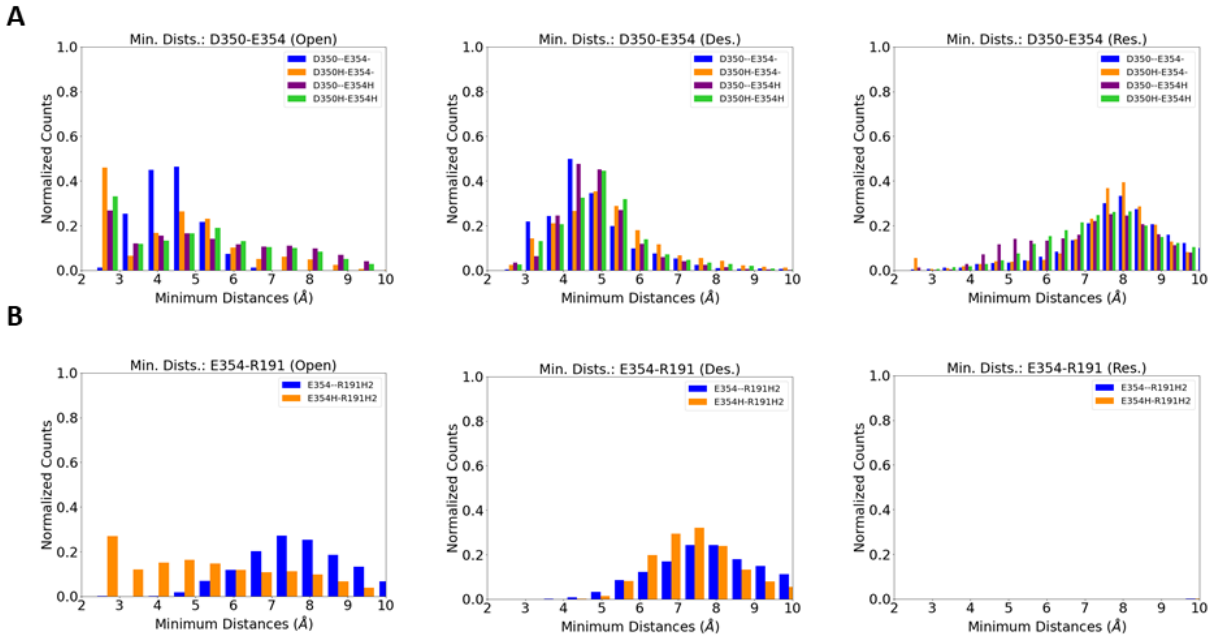

Appendix A Figure 4.8 Approximation of the probability density functions of distances between acidic pocket interactions.
A) D350-E354, B) E354-R191 donor-acceptor atom distances for the open, desensitized, and resting states, from left to right. The data is normalized for the area under the curve for each system to equate to 1. Legends indicate the changes in protonation states of the residues of interest, relative to the background protonation states from Table 2.1. Counts over 10 Å exist but are not included in these plots.

Appendix A Table 4.1 Predicted protonation states of each functional state of cASIC1. The following protonation state configurations were applied to the simulations shown in Figure 2.6 for the resting, open and desensitized states (Figure 2.6 A, B, C, respectively). H denotes a protonated residue (neutralizing ASP/GLU; making HIS positive). H/- when highlighted in grey are residues that were not originally protonated (or unprotonated) in the original predicted protonation state (Table 2.1).

Ionizable Residue	*Resting State*	*Open State*	*Desensitized State*
H74	-	H	-
E80	-	H	-
E98	H	H	H
H111	-	H	H
E220	-	-	-
E239	H	-	-
H328	-	H	H
D346	-	-	-
E354	-	H	H
E374	-	H	H
D408	H	H	H
E412	-	H	H
E417	-	-	H
D433	-	-	H

Appendix B

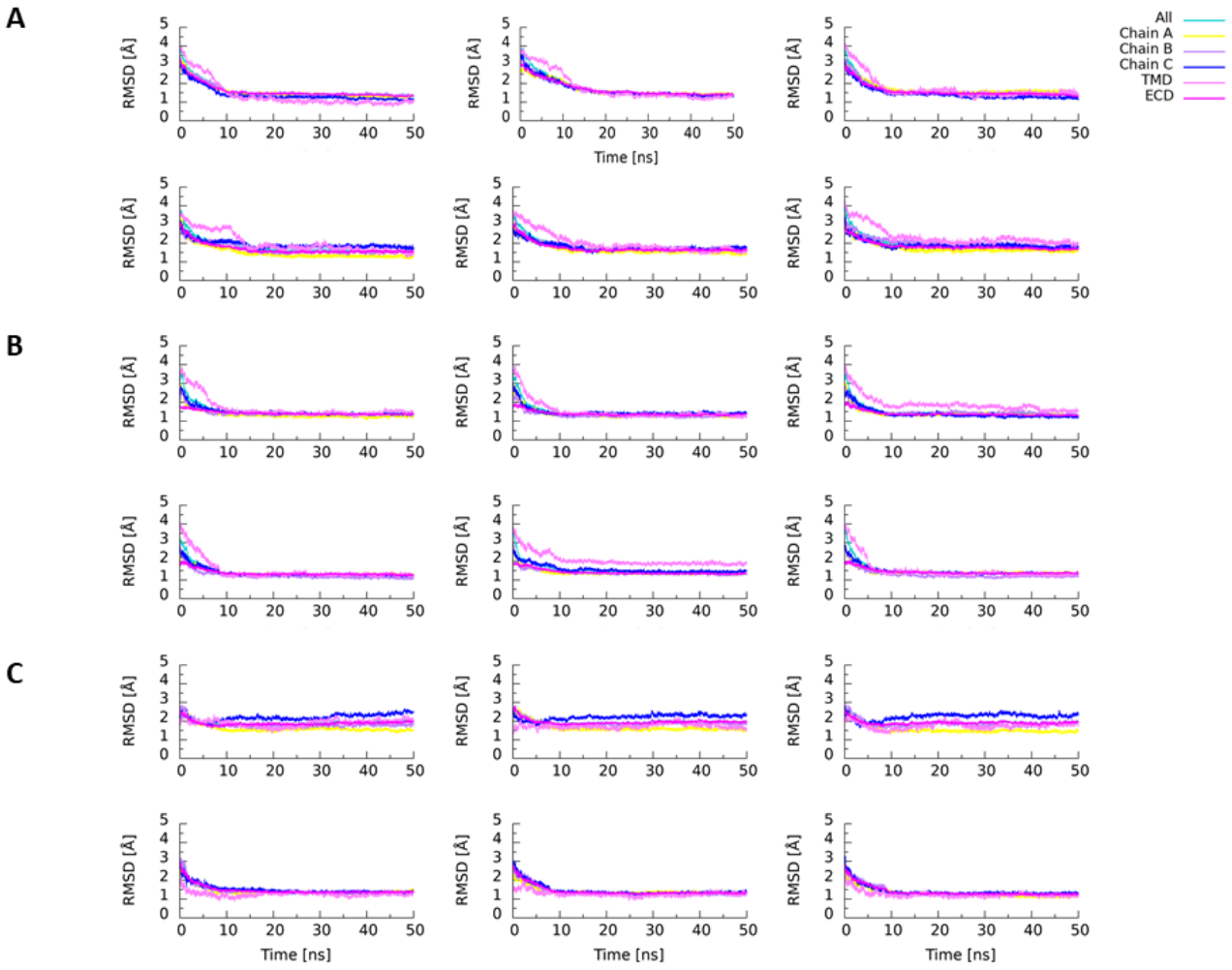

Appendix B Figure 4.9 RMSD of all targeted MD simulations.
The C_α RMSD of all starting structures is plotted in reference to the target structure as a function of time for A) the activation pathways, B) the desensitization pathways and, C) the recovery pathways. The top rows and the bottom rows represent the "native" and the "target" protonation configurations for each panel, respectively.

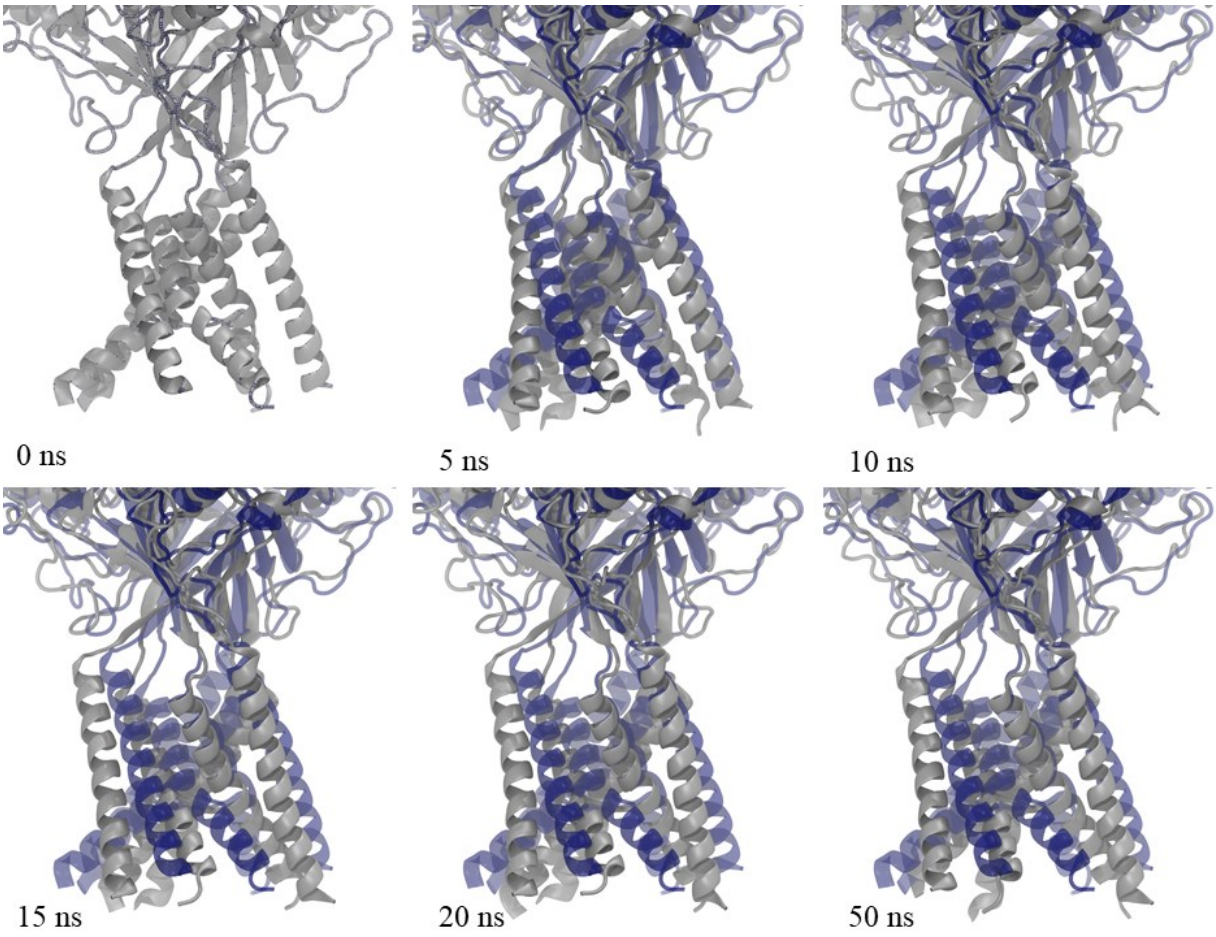

Appendix B Figure 4.10 Representative snapshots of the TMD in the activation pathway. The representation in blue is of the starting structure. The representation in grey is of the structure at the time points specified. Widening of the TMD subunits can be seen to occur after the initial untwisting of the three subunits from 5 to 10 ns where the top of the transmembrane helices of the 10 ns structure overlaps less with that of the starting structure (Supplementary Movie 1).

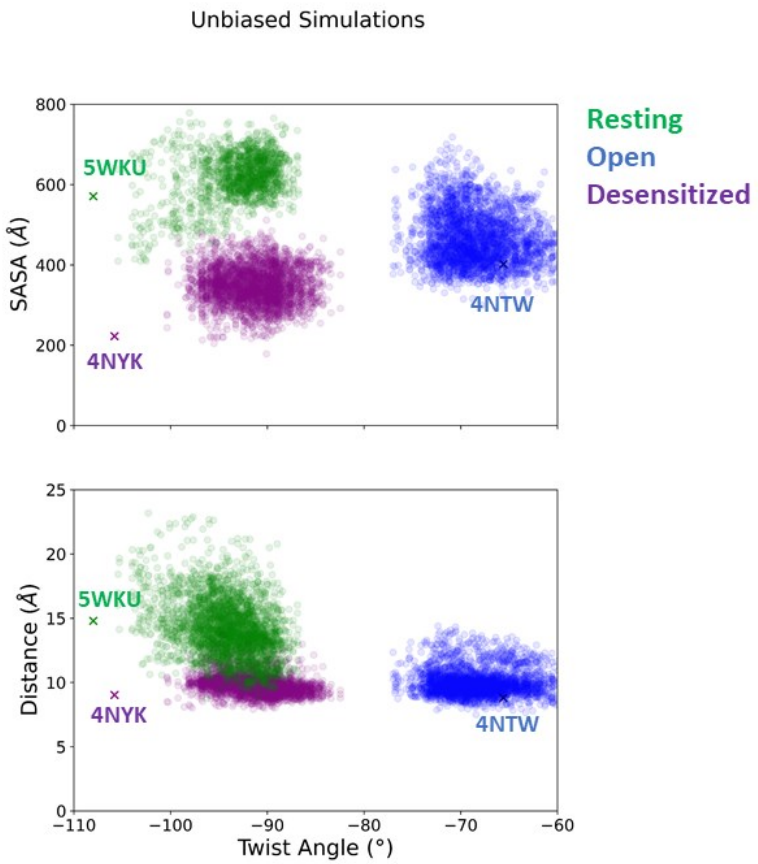

Appendix B Figure 4.11 Unbiased simulations.
The SASA and D238-D350 distances plotted as a function of the twist angle for the resting, open and desensitized states. The data in these simulations comes from systems with protonation configurations that match the functional state (i.e. resting state with resting state protonation, open state with open state protonation and desensitized state with desensitized protonation state (Table 2.1). Two simulations of 25 ns each are plotted for each functional state. The crystal structure reference measurements for the resting state (green), open state (blue) and desensitized state (purple) are drawn as X.

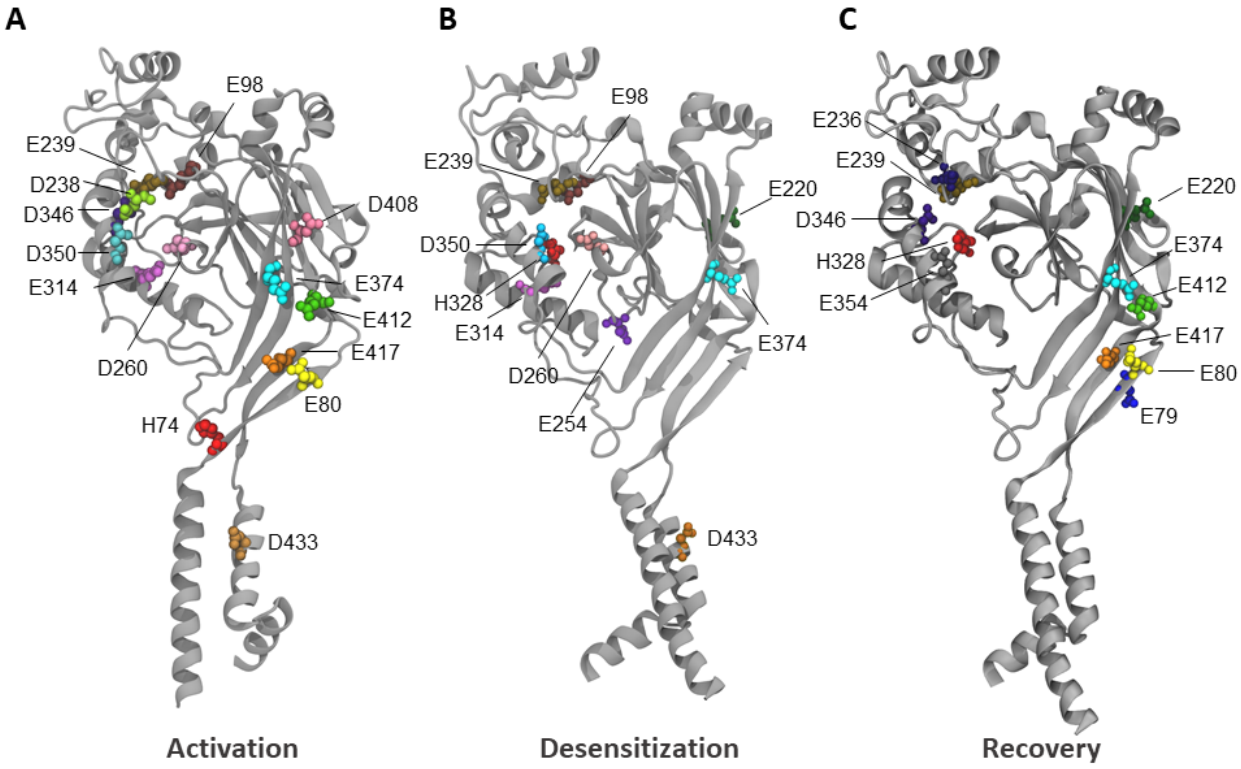

Appendix B Figure 4.12 Acidic and histidine residues with a pK_a shift > |1|.
A single subunit with ASP, GLU and HIS residues with an average $pK_{a,shift}$ greater than the magnitude of 1 for A) the activation simulations, B) the desensitization simulations, and C) the recovery simulations. Residues are shown in a 'Van der Waals' representation.

Appendix B Table 4.2 Activation with Resting Protonation State.
Average pK_a shifts of all ASP, GLU and HIS amino acid residues of the activation pathway with the "native" protonation configuration for each of three repeats. Rows are coloured by value of the mean $pK_{a,shift}$. Blank = $|pK_{a,shift}| < 0.5$, Orange = $|pK_{a,shift}| > 0.5$, Red $|pK_{a,shift}| > 1$.

Residue #	$pK_{a,shift}$ 1	$pK_{a,shift}$ 2	$pK_{a,shift}$ 3	Mean	Standard Deviation
79	0.186060606	-1.257252747	0.074848485	-0.332114552	0.655745146
108	0.320909091	-0.893106893	-0.01030303	-0.194166944	0.512388626
127	0.266060606	-0.772294372	-0.588787879	-0.365007215	0.452477332
132	0.134242424	-1.043153513	-0.11969697	-0.342869353	0.505911542
141	0.244242424	-1.085274725	0.044242424	-0.265596626	0.585322783
160	-0.053333333	-1.037795538	0.001818182	-0.363103563	0.477610279
165	-0.437575758	-1.699177489	-0.403636364	-0.846796537	0.602883591
184	-0.114545455	-0.571182151	-0.558484848	-0.414737485	0.212331104
203	-0.094545455	-1.291701632	0.024848485	-0.453799534	0.594487831
224	0.26969697	-1.467569098	0.311515152	-0.295452325	0.828987529
228	-0.053939394	-1.040709291	0.31969697	-0.258317238	0.573878051
238	0.716666667	-1.00011322	-0.256666667	-0.18003774	0.702963863
254	0.582727273	-1.331611722	-0.587575758	-0.445486735	0.78795745
260	-0.041515152	-1.786143856	-1.194848485	-1.007502498	0.724456678
290	-0.318484848	-1.446373626	-0.200909091	-0.655255855	0.561460305
297	-0.425454545	-1.612044622	-0.05969697	-0.699065379	0.662617524
302	-0.097575758	-1.200762571	-0.266666667	-0.521668332	0.485128624
312	-0.483939394	-1.352903763	0.437878788	-0.466321456	0.731190048
332	-0.022727273	-1.29952048	-0.034242424	-0.452163392	0.599190384
346	0.913939394	-0.699247419	0.96969697	0.394796315	0.773940564
350	1.182727273	-0.334289044	2.787878788	1.212105672	1.274788953
356	0.908181818	-0.789407259	0.01969697	0.046157176	0.693290356
408	-0.287878788	-2.874115884	-0.81969697	-1.327230547	1.115152704
433	-3.099090909	-3.023406593	-2.469090909	-2.863862804	0.280850691
454	-0.156969697	-0.98032634	-0.345151515	-0.494149184	0.352258683
80	-1.155454545	1.095151515	-0.61969697	-0.226666667	0.959917192
98	2.708181818	0.071818182	1.083939394	1.287979798	1.085918251
114	-0.424848485	0.855454545	0.503636364	0.311414141	0.540065428
124	-0.351818182	-0.763636364	0.305151515	-0.27010101	0.440140246
133	-0.330909091	0.096363636	0.682424242	0.149292929	0.415381145
137	-0.593030303	-0.561212121	-0.647878788	-0.600707071	0.035795506
157	0.311515152	0.065757576	0.211212121	0.196161616	0.100892962
168	0.113939394	0.25030303	-0.244848485	0.03979798	0.208832417
178	-0.261818182	-0.711818182	-0.059090909	-0.344242424	0.27277407

183	0.356969697	0.097272727	0.116363636	0.19020202	0.118179832
220	0.176666667	-0.282121212	0.586363636	0.16030303	0.354746209
229	-0.929090909	-0.50969697	-0.671818182	-0.703535354	0.172679478
236	0.03969697	-0.871515152	0.210606061	-0.207070707	0.47498582
239	3.06	1.547878788	3.500606061	2.702828283	0.836247442
243	-0.083333333	1.113939394	0.695757576	0.575454545	0.496131777
255	0.03030303	0.18	0.794242424	0.334848485	0.330539346
278	0.364848485	0.355454545	0.207575758	0.309292929	0.072027073
299	0.310606061	0.000909091	-0.26969697	0.013939394	0.237086824
314	0.094545455	1.349090909	2.116666667	1.186767677	0.833468725
320	0.543333333	0.303030303	-0.229090909	0.205757576	0.322755109
339	-0.328181818	0.410606061	0.277575758	0.12	0.32153224
343	0.04030303	-0.426666667	0.204848485	-0.060505051	0.267487755
354	-0.073636364	0.333030303	0.518787879	0.259393939	0.247397597
358	-0.407272727	0.343333333	-1.253333333	-0.439090909	0.652224608
363	0.723939394	0.219393939	0.366363636	0.436565657	0.211876964
374	1.19	-1.596969697	0.708181818	0.10040404	1.216236105
397	0.014242424	-0.444545455	-0.322727273	-0.251010101	0.194043112
402	0.005454545	0.157878788	-0.733939394	-0.19020202	0.389483449
412	-1.473636364	-1.840909091	-3.018484848	-2.111010101	0.658966427
417	2.37	0.644545455	1.268787879	1.427777778	0.71332867
420	0.394848485	0.631818182	0.950606061	0.659090909	0.227705178
426	0.671818182	-0.133636364	0.704242424	0.414141414	0.387563503
451	0.146666667	0.101818182	0.123333333	0.123939394	0.018314332
458	-0.276969697	-0.403636364	0.076666667	-0.201313131	0.203249743
74	1.161818182	1.153030303	0.906666667	1.073838384	0.118262685
111	0.192424242	0.129090909	0.007878788	0.10979798	0.076565523
164	-0.281818182	0.183030303	-0.376060606	-0.158282828	0.244392306
251	0.018787879	-0.025151515	-0.291515152	-0.099292929	0.137100218
328	-0.110909091	-0.497272727	-0.31030303	-0.306161616	0.157759476

Appendix B Table 4.3 Activation with Open Protonation State.
Average pK_a shifts of all ASP, GLU and HIS amino acid residues of the activation pathway with the "target" protonation configuration for each of three repeats. Rows are coloured by value of the mean $pK_{a,shift}$. Blank = $|pK_{a,shift}| < 0.5$, Orange = $|pK_{a,shift}| > 0.5$, Red $|pK_{a,shift}| > 1$.

Residue #	$pK_{a,shift}$ 1	$pK_{a,shift}$ 2	$pK_{a,shift}$ 3	Mean	Standard Deviation
79	-0.010909091	0.083030303	0.297272727	0.123131313	0.128970479
108	0.328484848	-0.412727273	0.054848485	-0.00979798	0.306031835
127	0.32969697	-0.322727273	-0.772727273	-0.255252525	0.45258475
132	-0.342121212	-0.007878788	0.056363636	-0.097878788	0.174685515
141	0.192121212	0.089393939	0.446969697	0.242828283	0.150318575
160	-0.142727273	0.031212121	0.194848485	0.027777778	0.13783612
165	-0.47030303	-1.302121212	0.568181818	-0.401414141	0.765100262
184	0.825757576	0.053636364	0.251818182	0.377070707	0.32742321
203	0.33	-0.965757576	-0.269090909	-0.301616162	0.529490537
224	0.523939394	0.853333333	1.133333333	0.836868687	0.249056295
228	-0.045151515	0.49030303	-0.094242424	0.116969697	0.264746184
238	0.741515152	2.293636364	1.780606061	1.605252525	0.645668496
254	-0.139090909	1.000909091	1.183333333	0.681717172	0.585157574
260	-0.323333333	-0.833636364	1.29	0.044343434	0.905114175
290	-0.425151515	-0.163333333	-0.169090909	-0.252525253	0.12208783
297	0.171515152	0.320909091	-0.509090909	-0.005555556	0.361239096
302	0.152121212	0.279393939	-0.149393939	0.094040404	0.179805073
312	-0.720606061	-0.109393939	-0.007878788	-0.279292929	0.31479548
332	0.05969697	-0.147878788	-0.03	-0.039393939	0.085002386
346	2.304545455	2.026363636	3.156666667	2.495858586	0.480865034
350	1.063636364	0.816060606	1.107878788	0.995858586	0.128412962
356	-0.346969697	0.047878788	-0.363333333	-0.220808081	0.190107719
408	0.388484848	-0.655757576	-0.126060606	-0.131111111	0.426325143
433	-2.238787879	-2.147878788	-2.827878788	-2.404848485	0.301421182
454	-0.016666667	-0.072121212	-0.030606061	-0.03979798	0.023553771
80	3.132424242	1.247878788	1.601818182	1.994040404	0.817825
98	2.146969697	2.085151515	2.629393939	2.287171717	0.243300101
114	0.093939394	-0.143030303	-0.557272727	-0.202121212	0.269119686
124	-0.277575758	-0.200606061	-0.252727273	-0.243636364	0.03207353
133	0.968181818	0.116969697	0.151212121	0.412121212	0.393442655
137	-0.366969697	-0.339393939	-0.846363636	-0.517575758	0.232760546
157	-0.033636364	0.286060606	0.335151515	0.195858586	0.163510302
168	0.387878788	0.398484848	-0.18030303	0.202020202	0.270378023
178	0.106666667	-0.267575758	-0.08030303	-0.08040404	0.152783847

183	0.322424242	0.107878788	0.416363636	0.282222222	0.129106874
220	-0.528484848	1.382727273	0.600909091	0.485050505	0.78453823
229	-0.146363636	0.058787879	-0.566363636	-0.217979798	0.26019257
236	0.75030303	0.720606061	0.085454545	0.518787879	0.306652693
239	-0.062121212	-1.332727273	-0.955757576	-0.783535354	0.532825995
243	0.828787879	1.037272727	0.98030303	0.948787879	0.087982523
255	1.012727273	0.645151515	0.914242424	0.857373737	0.155356622
278	0.136363636	0.364545455	0.129393939	0.21010101	0.109245775
299	0.163939394	-0.312121212	-0.13030303	-0.092828283	0.196149081
314	1.308484848	2.552424242	-1.522424242	0.779494949	1.705084608
320	0.13	0.300909091	-0.269393939	0.053838384	0.238972565
339	0.37030303	-0.05	-0.145151515	0.058383838	0.223954816
343	-0.112424242	-0.447878788	-0.639090909	-0.39979798	0.217682135
354	0.495454545	1.586666667	0.115757576	0.732626263	0.623474782
358	0.143636364	-0.226363636	-0.339090909	-0.140606061	0.206191135
363	-0.142121212	0.44969697	-0.092121212	0.071818182	0.267979208
374	1.592121212	1.740606061	0.055757576	1.129494949	0.761663048
397	-0.32969697	-0.365151515	-0.028181818	-0.241010101	0.151186782
402	-0.120606061	-0.387272727	0.823333333	0.105151515	0.519369246
412	-4.462121212	-2.384545455	-1.993333333	-2.946666667	1.083424691
417	1.209090909	0.836363636	0.607272727	0.884242424	0.248012855
420	0.187272727	0.633333333	0.843636364	0.554747475	0.273660506
426	-0.374242424	0.086363636	0.55	0.087373737	0.377321066
451	-0.049090909	-0.337878788	-0.146666667	-0.177878788	0.119945146
458	-0.061212121	-0.007272727	0.431515152	0.121010101	0.220661739
74	0.411515152	0.196060606	-0.145151515	0.154141414	0.229183127
111	-0.091212121	-0.10969697	-0.169393939	-0.123434343	0.033363011
164	-0.553030303	-0.211212121	-0.815151515	-0.526464646	0.247271778
251	0.004848485	-0.103030303	0.133333333	0.011717172	0.096617204
328	0.100606061	-0.475757576	0.732424242	0.119090909	0.493411318

Appendix B Table 4.4 Desensitization with Open Protonation State.
Average pK_a shifts of all ASP, GLU and HIS amino acid residues of the desensitization pathway with the "native" protonation configuration for each of three repeats. Rows are coloured by value of the mean $pK_{a,shift}$. Blank = $|pK_{a,shift}|$ <0.5, Orange = $|pK_{a,shift}|$ >0.5, Red $|pK_{a,shift}|$ > 1.

Residue #	$pK_{a,shift}$ 1	$pK_{a,shift}$ 2	$pK_{a,shift}$ 3	Mean	Standard Deviation
79	-0.141515152	-0.244545455	-1.224848485	-0.536969697	0.488219029
108	0.013030303	0.084848485	0.058484848	0.052121212	0.029662937
127	-0.490909091	-1.47969697	-0.195757576	-0.722121212	0.549071565
132	-0.467272727	-0.085151515	0.31969697	-0.077575758	0.321323689
141	0.100606061	0.736666667	-0.046060606	0.263737374	0.339729662
160	0.077575758	-0.048484848	0.508181818	0.179090909	0.238325322
165	0.060606061	-0.253939394	-0.823333333	-0.338888889	0.365831952
184	0.467878788	0.322727273	0.504242424	0.431616162	0.078414162
203	0.352727273	-0.300606061	-0.332727273	-0.093535354	0.315827687
224	-0.267878788	-0.477272727	0.287272727	-0.152626263	0.322588279
228	0.553030303	-0.587878788	-0.345757576	-0.126868687	0.490817446
238	-0.283333333	0.200606061	-0.21	-0.097575758	0.212961252
254	-0.57969697	-0.42030303	-0.710909091	-0.57030303	0.118825236
260	-0.046969697	-0.027878788	-0.472727273	-0.182525253	0.205351772
290	0.228787879	-0.008787879	0.199393939	0.13979798	0.105749134
297	0.38030303	0.548787879	-0.868484848	0.02020202	0.632149797
302	-0.136060606	0.003939394	-0.034545455	-0.055555556	0.059054033
312	-0.942727273	-0.097878788	-0.461818182	-0.500808081	0.346008092
332	-0.083030303	-0.001515152	0.022727273	-0.020606061	0.045236514
346	0.5	-0.898484848	0.129393939	-0.08969697	0.591574502
350	1.488181818	1.775757576	1.003939394	1.422626263	0.318484929
356	-0.115454545	-0.024848485	0.247878788	0.035858586	0.154416729
408	0.005454545	1.616060606	0.552727273	0.724747475	0.668683375
433	2.70030303	2.796060606	2.368181818	2.621515152	0.183349778
454	0.309393939	-0.019090909	-0.025454545	0.088282828	0.156370749
80	-0.772727273	1.829393939	-0.555151515	0.167171717	1.178720165
98	0.365757576	1.783636364	-0.728787879	0.473535354	1.028520274
114	0.523333333	0.151818182	0.260606061	0.311919192	0.15595011
124	0.04030303	-0.144242424	-0.200606061	-0.101515152	0.102886709
133	-0.02969697	-0.031818182	-0.274545455	-0.112020202	0.114925971
137	-0.637575758	-0.106969697	-0.304848485	-0.34979798	0.218938409
157	0.080606061	0.046363636	0.071212121	0.066060606	0.01444621
168	0.296363636	0.030909091	0.604545455	0.310606061	0.234402509
178	-0.069090909	-0.447878788	-0.799090909	-0.438686869	0.298092121

183	0.044848485	0.681212121	0.37969697	0.368585859	0.259913142
220	0.221515152	-1.396969697	-0.700909091	-0.625454545	0.662894332
229	0.826060606	-0.255757576	0.161818182	0.244040404	0.445460821
236	0.729393939	0.275151515	1.20030303	0.734949495	0.377711953
239	-0.564848485	-0.386060606	1.041515152	0.03020202	0.718821704
243	0.499393939	0.698181818	0.726969697	0.641515152	0.101179757
255	0.171515152	0.566969697	0.466363636	0.401616162	0.167809914
278	-0.22969697	0.301515152	-0.03030303	0.013838384	0.219101084
299	0.136969697	0.132121212	0.236969697	0.168686869	0.048323807
314	0.361818182	0.336666667	-0.38969697	0.102929293	0.348490675
320	0.684848485	-0.247878788	0.135757576	0.190909091	0.382776095
339	-0.076666667	-0.243030303	0.394848485	0.025050505	0.270163067
343	-0.597878788	-0.063636364	-0.642727273	-0.434747475	0.26305315
354	0.162424242	-0.438484848	0.145454545	-0.043535354	0.279357382
358	0.04	-0.635454545	-0.348484848	-0.314646465	0.276789316
363	0.163636364	-0.038484848	1.083636364	0.402929293	0.488354266
374	2.619090909	1.834848485	-0.671515152	1.260808081	1.403368293
397	0.051212121	-0.032727273	0.026666667	0.015050505	0.035238775
402	-0.396363636	0.362424242	-0.415454545	-0.14979798	0.362279652
412	1.564545455	-0.001212121	1.138787879	0.900707071	0.661014901
417	0.014848485	-1.307878788	-1.316969697	-0.87	0.625693371
420	-0.279393939	0.565151515	-0.14969697	0.045353535	0.371346901
426	-0.666060606	0.221515152	-0.178787879	-0.207777778	0.362930656
451	0.081212121	-0.133636364	0.128181818	0.025252525	0.113976013
74	0.529393939	-0.311818182	0.406060606	0.207878788	0.37091462
111	-0.001212121	0.016969697	-0.000909091	0.004949495	0.008500467
164	0.097575758	0.142424242	0.211818182	0.150606061	0.046996734
251	0.461515152	-0.170909091	-0.206969697	0.027878788	0.306980416
328	0.383030303	-0.413939394	0.777878788	0.248989899	0.495703384

Appendix B Table 4.5 Desensitization with Desensitized Protonation State.
Average pK_a shifts of all ASP, GLU and HIS amino acid residues of the desensitization pathway with the "target" protonation configuration for each of three repeats. Rows are coloured by value of the mean $pK_{a,shift}$. Blank = $|pK_{a,shift}|$ <0.5, Orange = $|pK_{a,shift}|$ >0.5, Red $|pK_{a,shift}|$ > 1.

Residue #	$pK_{a,shift}$ 1	$pK_{a,shift}$ 2	$pK_{a,shift}$ 3	Mean	Standard Deviation
79	-1.239393939	0.241818182	1.420606061	0.141010101	1.088277447
108	1.241515152	0.151818182	-0.177575758	0.405252525	0.606424756
127	-1.072121212	-0.641818182	-1.154545455	-0.956161616	0.224807006
132	0.198787879	0.203636364	0.096363636	0.166262626	0.049465669
141	0.044242424	-0.026666667	0.388484848	0.135353535	0.181316705
160	0.02	-0.015151515	-0.009090909	-0.001414141	0.015342899
165	-0.392121212	0.333030303	-0.329393939	-0.129494949	0.328055772
184	0.432727273	-0.118484848	0.846363636	0.386868687	0.395230234
203	-0.206363636	-0.567575758	0.482424242	-0.097171717	0.435558765
224	-0.383636364	-1.139393939	-0.820909091	-0.781313131	0.309804517
228	-0.507878788	0.753939394	0.153636364	0.133232323	0.515337122
238	-0.745151515	0.578787879	0.524848485	0.119494949	0.611793808
254	-1.14	-1.285151515	-1.391515152	-1.272222222	0.103086833
260	-1.572424242	-1.572424242	-0.378787879	-1.174545455	0.562685578
290	0.130606061	0.491515152	0.358787879	0.326969697	0.149048405
297	0.222727273	-0.496666667	-0.166363636	-0.146767677	0.294018039
302	-0.068484848	-0.032121212	-0.254848485	-0.118484848	0.097559758
312	0.17969697	0.079393939	-0.028484848	0.076868687	0.085008627
332	-0.007575758	-0.634242424	-0.106969697	-0.24959596	0.274996322
346	0.149090909	1.823939394	0.666969697	0.88	0.700150362
350	2.813030303	0.335151515	1.452121212	1.533434343	1.01322248
356	0.480909091	0.47	0.815151515	0.588686869	0.160196607
408	-1.193939394	-1.482727273	0.116060606	-0.853535354	0.695670829
433	2.840909091	1.462121212	2.305454545	2.202828283	0.567546248
454	-0.254848485	-0.253333333	0.10030303	-0.135959596	0.16706405
80	-0.696969697	-0.567272727	-1.123636364	-0.795959596	0.237675373
98	1.494242424	0.653030303	1.266666667	1.137979798	0.355274252
114	0.286666667	-0.122727273	0.436060606	0.2	0.236212202
124	-0.289090909	-0.330909091	0.428787879	-0.063737374	0.348686137
133	-0.181818182	0.104242424	-0.058787879	-0.045454545	0.117163706
137	-0.255151515	-0.204545455	-0.123636364	-0.194444444	0.054163835
157	-0.520606061	-0.169090909	-0.197575758	-0.295757576	0.159416598
168	0.033333333	-0.182424242	0.708787879	0.186565657	0.379626896
178	-0.467878788	-0.066969697	-0.231212121	-0.255353535	0.164558259

183	0.368181818	-0.176363636	-0.09	0.033939394	0.238960482
220	1.36030303	1.673333333	0.24969697	1.094444444	0.610844069
229	-0.471818182	-0.040909091	1.123333333	0.203535354	0.67376648
236	0.728484848	0.008787879	1.053333333	0.596868687	0.436471391
239	-2.194242424	-0.352727273	-1.192424242	-1.246464646	0.752765916
243	-0.180606061	1.448181818	0.790909091	0.686161616	0.669062286
255	0.367272727	0.913333333	-0.120909091	0.386565657	0.422448033
278	-0.036666667	0.108484848	0.004848485	0.025555556	0.061040029
299	-0.321818182	-1.080909091	-0.450606061	-0.617777778	0.331677091
314	1.531818182	1.474545455	2.261515152	1.755959596	0.358245592
320	0.31	0.263030303	0.077272727	0.216767677	0.10048439
339	0.501818182	0.127272727	-0.223030303	0.135353535	0.295973316
343	-0.315757576	-0.338787879	-0.112121212	-0.255555556	0.101858257
354	-0.650909091	0.211818182	-0.09	-0.176363636	0.357461975
358	-0.00969697	-0.797575758	0.010909091	-0.265454545	0.376360546
363	-0.175757576	0.563939394	0.295454545	0.227878788	0.305737103
374	1.082424242	0.653939394	1.461515152	1.065959596	0.329896918
397	-0.14030303	-0.517575758	0.075757576	-0.194040404	0.245189573
402	-0.543030303	-0.917272727	-0.183030303	-0.547777778	0.299772011
412	-0.133333333	1.313333333	-0.682424242	0.165858586	0.841783396
417	0.691515152	-0.231818182	-0.504242424	-0.014848485	0.511706903
420	1.122424242	0.022424242	-0.219090909	0.308585859	0.583856191
426	-0.425151515	-0.055454545	-0.483939394	-0.321515152	0.189657917
451	0.161818182	0.282727273	0.147272727	0.197272727	0.060716566
74	0.076666667	-0.471818182	-0.655151515	-0.35010101	0.310913456
111	-0.021818182	-0.006666667	-0.076666667	-0.035050505	0.030070149
164	0.569393939	0.537575758	0.06969697	0.392222222	0.228429425
251	-0.05	-0.032424242	0.055151515	-0.009090909	0.045989445
328	-1.406363636	-1.368787879	-3.038484848	-1.937878788	0.778397182

Appendix B Table 4.6 Recovery with Desensitized Protonation State.
Average pK_a shifts of all ASP, GLU and HIS amino acid residues of the recovery pathway with the "native" protonation configuration for each of three repeats. Rows are coloured by value of the mean $pK_{a,shift}$. Blank = $|pK_{a,shift}| < 0.5$, Orange = $|pK_{a,shift}| > 0.5$, Red $|pK_{a,shift}| > 1$.

Residue #	$pK_{a,shift}$ 1	$pK_{a,shift}$ 2	$pK_{a,shift}$ 3	Mean	Standard Deviation
79	0.964545455	1.027272727	0.014545455	0.668787879	0.463327487
108	0.106363636	0.118787879	0.141515152	0.122222222	0.014554571
127	-0.02969697	0.063939394	0.423030303	0.152424242	0.195128457
132	0.36	-0.788484848	0.573333333	0.048282828	0.598059577
141	0.113636364	-0.243636364	0.138787879	0.002929293	0.17465035
160	0.081515152	0.013333333	0.001212121	0.032020202	0.03534632
165	-0.045454545	-1.044242424	-0.437575758	-0.509090909	0.410877207
184	0.519393939	0.173636364	0.951818182	0.548282828	0.318347464
203	0.234545455	0.817878788	0.64	0.564141414	0.244111093
224	0.38	-0.041818182	-0.450909091	-0.037575758	0.33923048
228	0.168787879	0.412121212	0.762121212	0.447676768	0.243528587
238	-0.575454545	-0.516969697	-1.116363636	-0.736262626	0.269830444
254	0.391212121	-0.135454545	0.240909091	0.165555556	0.221514576
260	-0.067272727	0.080909091	-0.887878788	-0.291414141	0.426080602
290	0.023030303	0.252727273	-0.773636364	-0.165959596	0.439805612
297	-0.35969697	0.154242424	0.358181818	0.050909091	0.30204395
302	0.417575758	0.04030303	0.101515152	0.186464646	0.165319872
312	-0.209393939	1.28	-0.045151515	0.341818182	0.666774693
332	-0.108181818	0.037272727	-0.116969697	-0.062626263	0.070730299
346	-0.635757576	0.891212121	0.377272727	0.210909091	0.63438514
350	-0.747272727	-0.581212121	0.22	-0.369494949	0.42231288
356	0.231212121	0.994848485	1.593939394	0.94	0.557681314
408	0.032727273	2.088484848	-0.416969697	0.568080808	1.090650624
433	0.056060606	-1.031818182	-1.276060606	-0.750606061	0.579049177
454	-0.127272727	-0.489393939	-0.182727273	-0.266464646	0.159252219
80	-0.909393939	-0.752424242	-0.187272727	-0.616363636	0.310106571
98	-1.313030303	0.423030303	-0.257272727	-0.382424242	0.714247288
114	-0.194242424	0.015454545	-0.036363636	-0.071717172	0.08918374
124	-0.474242424	-0.056666667	-0.175454545	-0.235454545	0.175674658
133	0.022424242	0.061212121	0.044242424	0.042626263	0.015876269
137	-0.501212121	-0.115454545	-0.19	-0.268888889	0.167072478
157	-0.158787879	-0.317272727	-0.182424242	-0.219494949	0.069809454
168	0.762121212	1.083636364	0.577272727	0.807676768	0.209216817
178	0.82969697	0.351212121	0.281515152	0.487474747	0.243654747

183	0.128787879	-0.199393939	0.018484848	-0.017373737	0.136357875
220	0.041212121	-1.928181818	0.916363636	-0.323535354	1.189577026
229	0.563636364	0.653636364	0.473636364	0.563636364	0.073484692
236	1.191818182	0.911212121	1.047878788	1.05030303	0.114569769
239	-2.332121212	-3.443333333	-3.293939394	-3.023131313	0.492409624
243	-0.064242424	-0.266060606	-0.156060606	-0.162121212	0.082503304
255	0.277878788	0.265757576	0.367272727	0.303636364	0.045268981
278	-0.989090909	-0.679393939	-0.476666667	-0.715050505	0.210710218
299	-0.066969697	-0.056060606	0.000909091	-0.040707071	0.029762177
314	0.796969697	0.512424242	-0.443636364	0.288585859	0.530630798
320	0.344545455	-0.473333333	-0.263030303	-0.130606061	0.346779049
339	-0.206969697	-0.214848485	-0.064848485	-0.162222222	0.068928719
343	-0.43	-0.020909091	-0.017878788	-0.156262626	0.193565507
354	-2.023636364	-2.020909091	-2.614848485	-2.21979798	0.27934511
358	0.014242424	-0.355757576	-0.314242424	-0.218585859	0.16550455
363	-0.011515152	0.59969697	0.042121212	0.21010101	0.276354813
374	-1.425454545	1.523636364	0.706060606	0.268080808	1.243155669
397	0.02969697	-0.206363636	-0.375151515	-0.183939394	0.166037564
402	-0.414242424	0.136363636	0.114545455	-0.054444444	0.254571467
412	1.516060606	0.377272727	-0.312121212	0.527070707	0.753831001
417	-0.941818182	-0.627878788	-0.992727273	-0.854141414	0.161336121
420	-0.473030303	-0.438484848	-0.258484848	-0.39	0.094058575
426	-0.196666667	0.265454545	0.076969697	0.048585859	0.189724775
451	-0.195757576	0.524545455	0.301515152	0.21010101	0.30108307
74	-0.173030303	-0.150606061	-0.07969697	-0.134444444	0.03978003
111	0.298787879	-0.304848485	-0.334545455	-0.113535354	0.291808514
164	-0.196363636	0.067878788	0.14969697	0.007070707	0.147676906
251	0.026060606	-0.086969697	-0.151515152	-0.070808081	0.073390216
328	-1.141515152	-1.925454545	-1.695454545	-1.587474747	0.329023779

Appendix B Table 4.7 Recovery with Resting Protonation State.
Average pK_a shifts of all ASP, GLU and HIS amino acid residues of the recovery pathway with the "target" protonation configuration for each of three repeats. Rows are coloured by value of the mean $pK_{a,shift}$. Blank = $|pK_{a,shift}| < 0.5$, Orange = $|pK_{a,shift}| > 0.5$, Red $|pK_{a,shift}| > 1$.

Residue #	$pK_{a,shift}$ 1	$pK_{a,shift}$ 2	$pK_{a,shift}$ 3	Mean	Standard Deviation
79	0.450909091	0.163333333	0.224242424	0.279494949	0.123732467
108	-0.199090909	0.199393939	0.136060606	0.045454545	0.174842095
127	-1.125757576	-0.464242424	1.442727273	-0.049090909	1.088895982
132	0.271212121	0.301212121	0.445757576	0.339393939	0.076201126
141	-0.050909091	-0.173939394	-0.114848485	-0.113232323	0.05023991
160	-0.041212121	0.061818182	0.025454545	0.015353535	0.042664065
165	-0.015454545	-0.337272727	0.125454545	-0.075757576	0.193660311
184	0.813939394	1.133333333	0.630606061	0.859292929	0.207728003
203	0.167575758	0.36	-0.166060606	0.120505051	0.217327217
224	-0.41030303	-0.575151515	-0.856363636	-0.613939394	0.184157343
228	0.371818182	1.01969697	0.820606061	0.737373737	0.27096426
238	-0.00030303	-0.296363636	0.13030303	-0.055454545	0.178498139
254	-0.27030303	0.014242424	-0.608484848	-0.288181818	0.254541486
260	0.402727273	0.491515152	0.400909091	0.431717172	0.042290072
290	0.576363636	-0.220606061	0.565454545	0.307070707	0.373150399
297	0.446969697	-0.376969697	0.084545455	0.051515152	0.337181733
302	0.046363636	-0.58030303	-0.05	-0.194646465	0.275523414
312	-0.476363636	-0.262727273	-0.181818182	-0.306969697	0.124250554
332	-0.075454545	-0.025757576	0.071818182	-0.00979798	0.061173772
346	0.87030303	1.162424242	1.034848485	1.022525253	0.119575909
350	0.357878788	0.588181818	1.246969697	0.731010101	0.376758632
356	0.485454545	0.877878788	1.337575758	0.90030303	0.348238209
408	1.090909091	0.447272727	1.181212121	0.906464646	0.326783897
433	0.743333333	0.247272727	0.383636364	0.458080808	0.20924549
454	0.570606061	0.03030303	-0.138181818	0.154242424	0.302341743
80	-0.89969697	-2.035151515	-0.577575758	-1.170808081	0.625170749
98	-0.536666667	0.044848485	-0.605454545	-0.365757576	0.29169727
114	0.107878788	-0.223939394	-0.175454545	-0.097171717	0.146337458
124	-0.62	-0.239090909	-0.155151515	-0.338080808	0.202270905
133	0.09030303	-0.036666667	-0.099393939	-0.015252525	0.078909903
137	-0.202424242	0.071818182	-0.444242424	-0.191616162	0.21081943
157	-0.006363636	0.069090909	-0.129393939	-0.022222222	0.081803341
168	0.072727273	-0.343636364	-0.104545455	-0.125151515	0.1706031
178	0.163939394	-0.243333333	0.09969697	0.006767677	0.178782286

183	-0.673333333	-0.361515152	-0.494848485	-0.50989899	0.127743318
220	0.313636364	0.042121212	-0.001818182	0.117979798	0.139508151
229	-0.216666667	-0.784545455	0.759090909	-0.080707071	0.637477877
236	1.11	0.210606061	0.797272727	0.705959596	0.372809988
239	0.339393939	0.780909091	0.920909091	0.68040404	0.247811645
243	0.236060606	0.190909091	0.046666667	0.157878788	0.080770319
255	0.455151515	1.213636364	0.982424242	0.883737374	0.317415752
278	-0.177575758	-0.550606061	-0.906363636	-0.544848485	0.297554259
299	0.278787879	-0.987272727	-1.165151515	-0.624545455	0.642867819
314	1.492727273	-0.738787879	-0.148787879	0.201717172	0.944124042
320	-0.140606061	-0.066666667	-0.321212121	-0.176161616	0.10691584
339	-0.383030303	0.035151515	-0.103939394	-0.150606061	0.17388184
343	0.198787879	0.352727273	-0.095757576	0.151919192	0.186068393
354	-0.895151515	-0.999090909	-1.12969697	-1.007979798	0.095958852
358	0.014242424	-0.252727273	0.393333333	0.051616162	0.265073793
363	0.124848485	0.124242424	-0.285454545	-0.012121212	0.193276012
374	-1.157272727	-0.845454545	-1.231212121	-1.077979798	0.167168086
397	-0.261818182	-0.072727273	-0.302121212	-0.212222222	0.100000714
402	-0.01969697	-0.604242424	-0.438181818	-0.354040404	0.245944683
412	0.384242424	0.692727273	2.184545455	1.087171717	0.786113887
417	1.336969697	1.918181818	1.104242424	1.453131313	0.342290788
420	-0.738484848	0.15	0.435454545	-0.051010101	0.499891469
426	-0.266060606	0.14	-0.176363636	-0.100808081	0.174170004
451	-0.57030303	0.919090909	-0.216666667	0.044040404	0.635373753
74	0.359090909	-0.225757576	-0.420606061	-0.095757576	0.331317412
111	0.341212121	0.536363636	0.283030303	0.386868687	0.108344623
164	0.125151515	0.142121212	0.220606061	0.162626263	0.041579124
251	-0.278484848	-0.231212121	0.092727273	-0.138989899	0.16498144
328	0.773939394	-0.168484848	-0.112424242	0.164343434	0.431656594

Supplementary Movies

Supplementary Movie 1. Movie illustrating the transmembrane domain upon activation during a molecular dynamics trajectory. The ECD and TMD junction of the trimer is shown. R65, E426 and D433 are shown in Licorice representation. Initial untwisting of the TM helices occurs within the first 2 seconds (~3 ns in the simulation) of the movie (first a smoothing function was used. R65 and E426' begin with electrostatic interactions that are broken at ~8 seconds (~12 ns in the simulation) coinciding with the widening of the pore. The simulation time is 50 ns. The movie is representative of the activation system with a resting protonation state.

Supplementary Movie 2. Movie illustrating the collapse of the ACP upon activation during a molecular dynamics trajectory. A close-up of the ACP with acidic residues E98, D238, E239, E314, D346, D350 and the basic R191 is shown in Licorice representation. The backbone of the active protein is shown in an Opaque green and the backbone of the protein as well as the side chain of R191 at the start of the simulation is shown in a translucent (Ghost) representation to depict the changes in conformation. Sodium ions are shown as yellow spheres. The simulation time represents the first 29 ns of the simulation. R191 undergoes a drastic conformational change from pointing downwards into the ECD to upwards to interact with the acidic residues of the thumb and D238/E239 loops. The upper thumb helix domain can also be seen to approach the right-hand side of the ACP. The system is an activation system with the open protonation state imposed. In this case, H74, E80, E98, H111, H328, D346, E354, E374, D408, and E412 are fully protonated (Table 2.1). Hydrogen atoms are not shown for simplicity. Sodium ions tend to interact with unprotonated acidic residues (D238 and D350). Unlike the activation simulations with a resting protonation state, there are fewer sodium ions present in the ACP.

Supplementary Movie 3. Movie illustrating the closure of the TMD gate in desensitization with a desensitized protonation state. Side view of the ECD and TMD junction as a trimer. R65, E426 and D433 (protonated) are shown in Licorice representation. First, D433 (cyan bonds) is well poised to interact with R65 in intra-subunit interactions. The TM helices twist to a tighter angle in a counter-clockwise manner within the first 4 s (~ 6 ns) of the movie. At around 5-6 s (~ 7-9 ns), inter-subunit electrostatic interactions between R65 and E426' form. The protonated D433 also interacts with the backbone carbonyl of A438' of the adjacent subunit in two instances. The movie represents the first 18 ns of the simulation.

Supplementary Movie 4. Movie illustrating the flip of the H328 side chain in activation with an open protonation configuration. Close up of the lower ACP. E314, D260, R191 H328 and E98 are shown in Licorice representation. The backbone of the active protein is shown in opaque green and the backbone and H328 of the starting structure at 0 ns are shown as translucent. R191 begins in proximity to the side chains of E314 (left) H238, (behind R191) and D260 (right). This distance between these residues with R191 quickly increases at one second. At 6 s (~9 ns), the side chain of H328 flips outside of the ACP, becoming more exposed to solvent, not appearing to form any interactions. A note that H328 is doubly protonated (HISP) in this system. The movie represents the first 17 ns of the simulation.